Bose Polarons and Tunable Spin Dynamics in an Ultracold Mixture of ^{87}Rb and ^{23}Na Atoms

超冷 ^{23}Na-^{87}Rb 混合物中的極化子和自旋氣體

LI, Lintao

李林濤

A Thesis Submitted in Partial Fulfilment
of the Requirements for the Degree of
Doctor of Philosophy
in
Physics

The Chinese University of Hong Kong
December 2020

Thesis Assessment Committee

Prof. LAW Chi Kwong (Chair)

Prof. WANG Dajun (Thesis Supervisor)

Prof. YANG Sen (Committee Member)

Prof. ZHANG Shizhong (External Examiner)

Abstract

An ultracold Bose-Bose mixture of ^{87}Rb and ^{23}Na provides an excellent platform for studying not only few-body but also many-body physics. A key feature of ultracold atoms mixture is the tunable interspecies interaction, which is facilitated by the Feshbach resonance. In this thesis, we study the behavior of ultracold Bose-Bose mixture under different interspecies interaction. The studies are divided into two different topic, each of them corresponds to a different regime of many-body physics.

The primary research is about the behavior of the impurities in Bose-Einstein condensate, which is also known as the polaron state. We use the radio frequency spectroscopy to probe the spectra of the ^{87}Rb impurities in a ^{23}Na Bose-Einstein condensate. For the trap-averaged spectra, near quantitative agreement between the theory and experimental data can be observed without any fitting parameters. Besides, we develop a fitting model which helps us find the energy and residue immune from the trap-averaging. The results shows the deviation of polaron energy and residue at strong interacting regime, which can not be explained by field-theoretic approach and two-body variational theory.

The second research investigates the manipulation of heteronuclear spinor dynamics by microwave and light field. Previously, we have observe the first heteronuclear spin coherent heteronuclear spin oscillation in a spin-1 mixture of ^{87}Rb and ^{23}Na atoms. Here, we observe the spin population oscillation start from a pure $|0,0\rangle$ mixture of ^{87}Rb and ^{23}Na. We then demonstrate controlling of the spin dynamics by either a detuned microwave field or a laser beam, which selectively dress the energy levels of ^{87}Rb atoms. The results introduce a new techniques for investigating spin dynamics with fast temporal and high spatial resolutions.

摘要

基於 ^{87}Rb 和 ^{23}Na 的超冷波色混合氣體給少體以及多體物理提供了極佳的實驗平台。而對於异核混合氣體，其最關鍵的特性即是可以通過 Feshbach 共振調控异核原子間的相互作用。在這篇論文中，我們研究了超冷波色混合氣體在各種异核相互作用下的一些特性，具體的研究包括了多體物理下兩個研究方向。

這篇論文的第一個方向是研究雜質原子在波色愛因斯坦凝聚中的特性即波色極化子問題。我們使用射頻波譜學探測 ^{87}Rb 雜質在 ^{23}Na 凝聚態中的能量譜。通過對阱中整體信號求平均的方式，在不需要任何擬合變量的前提下，我們所探測的能量譜與場論方法的理論計算幾乎一致。我們進一步利用擬合模型來去除整體平均所帶來的失真，得到了特定凝聚態密度下極化子的能量和殘余（residue）。我們發現這些結果與場論方法以及基於兩體理論的變分法下得到的數值在强相互作用區域發現了明顯的偏差。

這篇論文的第二個研究方向是使用微波和光場操控异核旋量混合氣的自旋交換動力學過程。在之前的研究中，我們在 F=1 的 ^{87}Rb-^{23}Na 混合氣體中觀察到了首個异核間的相干自旋動力學。基於之前的研究，我們進一步觀察了 $|0,0\rangle$ 初始態下不同自旋態原子數隨時間的變化。我們之後借助這個動力學過程演示了通過失諧微波以及光場下 ^{87}Rb 不同自旋態的能量平移對動力學的操控。這項研究給自旋動力學的快速和高分辨率操控提供了新的方式。

Acknowledgement

Before I came to CUHK, I was trained to be a mediocre engineer that only relies datasheets and application notes. I had several years' of experience on electronics but was still not familiar to experimental physics. I want to thank my advisor Prof. Dajun Wang for giving me the chance to work in his group and guiding me into the field of cold atoms experiment. His enthusiasm and conscientious attitude to science is the key for helping us grow. The most important thing I leaned from him is not any specific technology skill but how to slove a problem step by step in the scientific way when we don't have any experience.

I also want to thank the former group members of the lab, Fudong Wang, Bing Zhu, Bo Lu, Mingyang Guo and Xin Ye, who were patient to teach me how to run the experiment and maintain the cold atom machine. Following Xiaoke Li's work, my first scientifc project is the hetronuclear spin dynamics. Bo lu taught me basic laser optics and Bing Zhu shared a lot of his understanding in spinor physics. I benefit a lot from them during the past years. Shi Yu helped me taking the data when I was upgrating the magnetic field system. Later, Zhichao Guo and Junyu He joined our lab and Zhichao helped me a lot in the Bose polaron experiment. With the help of him, we built up the new dipole traps, new image systems, fast coils and made many other technical improvements. These improvements not only help me finish my polaron experiment but also provide many opportunities for future study. I would also like to thank Fan Jia and Junyu Lin who take the responsibilities for buying new items for lab. Both of them give me the impression that they have wide interests and new ideas in physics.

Finally, I want to thank the general lab and other supporting stuffs in physics department. With the help of them, we can efficiently working on the experiment with new instruments, electrical and mechanical components.

Contents

List of Figures

List of Tables

1

Introduction to this thesis

1.1 Introduction

Over a century ago, Niels Bohr proposed the Bohr model of atom, which together with the Plank's law, provided a first glimpse into the nature of quantum physics [1, 2]. Until today, the study of neutral atom is still the frontier of physics research. With the development of laser trapping, cooling and state manipulation, the unprecedented control of the parameters can be applied in the experiment. One of the most striking development is the study related to the new phase of matter [3] where the dilute samples of atom are cooled down to temperature well below one millions of a kelvin [4–6]. In a Bose-Einstein condensate (BEC), the temperature is so low that the thermal de Broglie wavelength $\sqrt{2\pi\hbar^2/(mk_BT)}$ of the atoms is at the same level as interparticle spacing and every particle shares the same quantum wavefunction. It is amazing that the behaviour of a macroscopic number of particles is dominated by quantum mechanical effects.

Quantum mechanics has shown great success in explaining an enormous amount of phenomena in our universe. The application of quantum mechanics ranges from the subatomic particles to the neutron stars. It builds a solid foundation for not only modern physics, but also chemistry, biology and electronics. It promotes the development of semiconductors which has totally changed our life. At this moment, quantum mechanics lead the development of a new generation of technology such as quantum computing, optical atomic clock, quantum cryptography and quantum simulations.

For the traditional calculation of a many-body system, with the increasing number of interacting particles, the increasing degrees of freedom quickly makes it impossible to calculate and describe the whole system. Even if

we could work on some less complicated cases, the deep insight into the physics of solutions is still not easy to come. To solve this kind of problems, we introduce quantum simulations which are the modern version of analog computations. The main idea is to build a flexible system to mimic another system which might be hard to study. Due to the low temperature, low density and large mass, compared with the condensed matter system, the cold atom system provides a much slower dynamics which is much easier to be studied by current technologies. And the low density also enables the local control and detection of the individual particles [7–9].

What is more, for cold atom system, the interaction between the particles and the energy of different spin states can be probed or even engineered [10–13], which provides a clean system for the quantum simulations. This feature is not limited to quantum gases of a single component; tunable interaction in a heteronuclear system exhibits rich physics which is inaccessible in single-species experiments. Highlight of these studies includes the exploration of Few-body physics [14–20], polaron physics [21–23], spinor physics [24, 25], quantum droplets [26], ultracold polar molecules [27–38], topological excitations [39] and phase separations [40–43].

In this thesis, I will talk about two studies related to the heteronuclear Bose-Bose mixture with interspecies interaction. Using this interaction, we measure and engineer some interesting quantum many-body physics in an ultracold mixture of ^{23}Na and ^{87}Rb.

The first topic of my research related to quantum many-body physics is the manipulation of heteronuclear spin dynamics with microwave and vector light shift. The spin degree of freedom in ultracold atomic gases has been recognized as a great assert for rich physics since 1998 [44, 45]. Although the atoms in BEC need not to be interacting with others, the thermal equilibrium mediated by elastic collisions is essential for keeping the condensate from fragmenting into small pieces [46]. The spinor physics study this kind of collisional coherence into the internal spin degree of freedom. In this so-called ultracold spinor gases, collative spin dynamics in the form of coherent spin population oscillations have been investigated with Bose condensate [45, 47–56], as well as thermal Bose gases [57, 58] and degenerate Fermi gases. The study of the spin dynamics promotes the spin

squeezing and multi-particle entanglement with potential applications in quantum metrology and quantum information [59–63]. And the study of the spin dynamics also promotes the deepening understanding of quantum phase transition in many-body systems such as Quantum Kibble-Zurek Mechanism [64, 65]. In this thesis, we explore in detail the various methods for the fast and local controlling of the heteronuclear spin dynamics.

The second topic of my research related to the many-body physics is the Bose polaron in ultracold Bose-Bose mixture. The polaron physics study the characteristics of mobile impurities in the quantum bath, which has wide relevance to the material physics. As first proposed by Landau and Pekar [66–68], the moving impurities can be described by the formation of quasiparticles which is generated by the dressing of the vibration modes in quantum bath. In 1946, anticipated by Landau's work on lattice defects, Pekar proposed the self-trapping state of the electron strong coupled to the induced polarization of atomic displacement in surrounding crystal lattice, which is called the polaron. The framework has now been developed for a wide range of systems. Recently, the Bose polaron - the impurity immersed in a BEC is observed in three individual experiments with Bose-Fermi mixture or spinor mixture of BEC [22, 23, 69] and it has been studied theoretically using a wide range of methods [70–81]. The phenomenon shows that the impurity can be dressed by the excitation of Bogliubov phonon in BEC, which is non-trivial and even exists in unitary regime. However, compared with Fermi polaron experiments [21, 82–84], the three and many-body interaction is not suppressed in BEC, which give rise to the broad spectrum and make both the experiment and theory be challenging but also more interesting for strong interactions [85–87]. In this thesis, we study the Bose polaron problem in a Bose-Bose mixture by immersing bosonic ^{87}Rb impurities in a BEC of ^{23}Na atoms.

1.2 Thesis outline

This thesis includes two main research topics that I was leading in ^{87}Rb-^{23}Na mixture setup. The first research topic is the heteronuclear spinor experiment with the manipulation of microwave and light dressing and the

second one is the Bose polaron experiment. The remainder of the thesis is organized as follows.

Chapter 2 gives a brief introduction to ultracold bosons. I will first talk about two-body interactions and how we tune the interparticle interactions. Then I will give the mean-field theory of weak interacting BEC, which is key for both spinor and polaron studies. Finally, I will give a brief introduction to the BEC properties that go beyond mean-field theory, which include the Lee-Huang-Yang (LHY) correlations and three-body interactions.

Chapter 3 introduces the improvements I made that enables the following experiments. The improvements includes the atom number, the atom number stability of the microwave evaporation, the gravitational sag free trap for ^{87}Rb-^{23}Na mixture, the low noise magnetic field servo system, the rf antenna for hyperfine state manipulation and the evaluation of the absorption image. These improvements give a better control and probe for our ten-year-old experiment setup.

Chapter 4 presents the study related to the manipulation of heteronuclear spinor dynamics. I include a general introduction and basic theory to the homonuclear and heteronuclear spinor problem. Then I show our experimental result for heteronuclear spin dynamics started from $|0,0\rangle$ mixture, which can not be explained by the mean-field and two body theory. We study the behaviour of the spin dynamics and we use microwave and light to control this dynamics. We prove that both the microwave dressing and light shift methods show negligible loss of atoms thus will be powerful techniques for investigating spin dynamics with fast temporal and high spatial resolutions.

Chapter 5 discusses the Bose polaron study. I present a brief introduction to the polaron problem and especially two theories for solving the Hamiltonian. Then I discuss the energy spectrum of the Bose polaron we observed by inverse rf spectroscopy. We give a detailed analysis of the spectrum, which includes both the simulation of the spectrum and the fitting of polaron energy and residue. We compared our result with the $\mathcal{T}$ approximation and the two-body variational theory. The comparison of the polaron

energy and residue shows evidence of the influence from Efimov trimer states.

Chapter 6 summarizes the major results and an outlook is also provided.

2

Interations and the behavior of ultracold Bose gases

In this chapter, we will mainly talk about the theory relative to the weak interacting Bose-Einstein condensate, which is the foundation for both spinor and polaron theories. This includes the theory of interatomic interactions and the theory of Bose-Einstein condensate.

In a BEC without interaction, all the atoms share the same wave function, that is, the wave function of a single atom. When we turn on the interaction between the atoms, the system can still be well understood if the atom cloud is dilute [88]. Here, the interparticle spacing is so large that it is hard to find more than two atoms within a region where they can interact with one another. Quantum mechanics provides the full solution for a two-body system or a homogeneous system dominated by the two-body interaction. Therefore I will introduce the two-body scattering, Feshbach resonance and Gross-Pitaevskii equation, which describes the behavior of a BEC dominated by two-body interactions.

However, the mean-field theory is not enough even for weak interacting bosons. Thus I will also give a brief introduction on Lee-Huang-Yang correlation and three-body physics. As we will introduce in Chapter 5, through the polaron theory is based on Bogoliubov approximation as we do for the weak interacting Bose gas and its Hamitonian is written as respect to the Bogoliubov modes. The three-body physics plays an important role that the existence of Efimov states can affect the behavior of Bose polaron. On the other hand, the three-body physics will also introduce the number loss of the atoms, which makes the experiments more challenging for the Bose gases.

2.1 Two-body interactions and Feshbach resonances

Compared with the range of van der Waals potential r_0, the averaging distance between the atoms is usually much larger for the dilute ultra-cold atom gases. Thus the two body scattering properties are enough for understanding phenomenon under this case. In general, the relative wave function between any two atoms can be decomposed into a series of components with angular momentum equal to an integer number l times $\hbar$ quanta. For bosons, the quantum statistics allow the scattering channel to have even value l and the s-wave ($l = 0$) is the strongest since the other channel will be mostly suppressed by the centrifugal barrier. That is because the scattering cross section will decrease as a result of the increase of collision energy.

To quantify the s-wave interaction between two atoms, we can define a parameter named scattering length for the scattering between two atoms. In scattering theory [89] we can write the wave function of a free particle moving in z direction being scattered by another atom as

$$\begin{aligned} \psi(r) &= e^{ikz} + f(\theta)\frac{e^{ikr}}{r} \\ &= \frac{sin(kr)}{kr} + \frac{cos(kr)}{r} \times f, \end{aligned} \tag{2.1}$$

where k is the wavevector of the atom, r is the position vector, f is the scattering amplitude and the second line is only valid for low energy cases of s-wave scattering. Though the short range interaction between two atoms is more like a complicated van der Waals potential, the s-wave approximation allows us to simplify it by replacing the short range interaction by a delta function like hard core potential, which vanishes at $r = a$. Using the boundary condition, the wave function of the atom is given by

$$\phi(r) = Asin(kr + \delta), \tag{2.2}$$

where $\delta = -ka$ is the phase shift. By comparing $\phi(r)$ and $\psi(r)$, we have the scattering amplitude:

$$f = \frac{1}{cot(\delta)k} \approx -a, \tag{2.3}$$

where a is the scattering length when $k \to 0$ and the cross section σ is $4\pi a^2$. $E = (\hbar k)^2/2\mu$ is the scattering energy of the scattered wave function, which can be defined as the open channel and μ is the reduced mass. However, there are much more channels for atoms because of the presence of the multiple hyperfine states. A Feshbach resonance is defined as the resonance between the open channel and a bound state provided by another channel, which is called close channel. If we tune the magnetic field, the energy of one close channel may happen to be approaching the energy of the open channel and a dramatic change of cross section will happen as the result of the phase shift δ of open channel crossing through $\pi/2$ due to the strong coupling.

For both ^{87}Rb and ^{23}Na, there are no broad Feshbach resonances below 1000 G and therefore we can simply treat them as the quantum gas with constant background scattering length. The background scattering length are $54.5a_0$ for ^{23}Na and $100.4a_0$ for ^{87}Rb [90, 91]. Here a_0 is the Bohr radius. The weak background interaction leads to the Bogoliubov phonon excitations in BEC, which is relevant to both the Bose plaron and the population fluctuation in spinor gases.

For a mixture of ^{87}Rb and ^{23}Na, a s-wave Feshbach resonance is used to control the interaction between Rb and Na both in the $|F = 1, m_F = 1\rangle$ state. The scattering length is given by

$$a = a_{bg}(1 - \frac{\Delta}{B - B_0}), \tag{2.4}$$

where $a_{bg} = 66.77a_0$ is the background scattering length, $\Delta = 5.2$ G is the width of the resonance and $B_0 = 347.64$ G is the position of the resonance [34, 92]. This Feshbach resonance is used to tune the interaction between the impurity and BEC background for Bose polaron experiment.

We notice that a_{bg} is only an approximation for the background scattering between two atoms since the background scattering lengths have very small

difference between the atoms in different spin states and the differences in the interaction energy can drive the coherent spin dynamics by the spin population oscillation.

The binding energy of the two-body bound state [93] which comes from the close channel can be calculated by the coupled channel calculation [13]. However, the equation for the binding energy is simple at the resonance centre since the close channel is mostly strong coupled to the scattering state and the binding energy is just the avoid crossing:

$$E_b = \frac{\hbar^2}{2\mu a^2}. \tag{2.5}$$

2.2 Bose-Einstein condensation in trap

The textbook example of BEC is in a cubical box with periodic boundary conditions. However, from the first Bose-Einstein condensation in 1995 to now, most of the BECs are created in a harmonic trap potential and the BEC formed by ultracold atoms is a clean system since it is dilute and can be described by the Gross-Pitaevskii (GP) equation [94, 95]. In this thesis I will only talk about the necessary knowledge for the experiments and many review papers provide a comprehensive introduction on ultracold Bose gas [96–99].

The GP equation is derived in 1961 and it is firstly used to describe the zero temperature wave function of bosons [100]. Although the equation is based on zero temperature, it is still valid for the condensed part of a BEC with finite temperature. However the equation works only for a weakly interacting BEC ($na^3 \ll 1$).

The wavefunction of a BEC can be written as the symmetrized product of single-particle state $\phi(r)$

$$\Psi(r_1, r_2, ..., r_N) = \prod_{i=1}^{N} \phi(r_i), \tag{2.6}$$

where N is the total number of the particle. The interaction can be included by mean-field approximation and using the effective contact interaction $g\delta(r_i - r_j)$, the Hamiltonian of the system with pseudopotential is

$$H = \sum_{i=1}^{N}[-\frac{\hbar^2}{2m}\frac{\partial^2}{\partial r_i^2} + V(r_i)] + g\sum_{i<j}\delta(r_i - r_j), \tag{2.7}$$

where $g = \frac{4\pi\hbar^2 a}{m}$, m is the mass of the particle and $V(r)$ is the external trap potential. The GP equation describe the ground state of Ψ that minimized the expectation value of the Hamiltonian under the normalization condition $\int |\Psi|^2 \, \mathrm{d}r = N$. And the calculation provides

$$[-\frac{\hbar^2}{2m}\bigtriangledown^2 + V(r) + g|\Psi(r)|^2]\Psi(r) = \mu\Psi(r), \tag{2.8}$$

which is the time-independent GP equation and μ is the chemical potential that keeps the conservation of total number of particles. The ground state is obtained by balancing the kinetic energy $-\frac{\hbar^2}{2m}\bigtriangledown^2$, trap potential $V(r)$ and contact interaction $g|\Psi(r)|^2$. With no interactions, the wave function of BEC is the ground state wavefunction of the trap. If the trap is harmonic, it gives the harmonic oscillator ground state with gaussian distribution and an oscillator length $a_{osc} = \sqrt{\hbar/m\bar{\omega}}$. For this thesis, the interaction is repulsive, finite and $na^3 \ll 1$, but the interaction energy is still much larger than the kinetic energy term ($\mu \approx ng \gg \hbar\bar{\omega}$ or $Na/a_{osc} \gg 1$), which is called the Tomas-Fermi regime. The repulsive interaction makes the BEC much larger since the larger size corresponds to the higher energy for repulsive interaction. The BEC takes the shape of external potential if we neglect the kinetic energy term:

$$n(r) = |\Psi(r)|^2 = \frac{\mu - V(r)}{g}. \tag{2.9}$$

The BEC density gives $n(r) = |\Psi(r)|^2$ and it is useful to write $\Psi(r) = \sqrt{n(r)}e^{i\phi(r)}$ with a phase term $\phi(r)$ for spinor gases. For a harmonic trap V(r), the chemical potential μ is determined by total number N:

$$\int n(r)\mathrm{d}r = \int \frac{\mu - V(r)}{g}\mathrm{d}r = \frac{1}{15}\left(\frac{2\mu}{\hbar\bar{\omega}}\right)^{5/2}\frac{a_{osc}}{a}. \tag{2.10}$$

By the given chemical potential, the Tomas-Fermi distribution of BEC in the harmonic trap is written as

$$n(r) = n_0 \left(1 - \frac{x^2}{R_x^2} - \frac{y^2}{R_y^2} - \frac{z^2}{R_z^2}\right), \tag{2.11}$$

where $R_{x,y,z} = \sqrt{\frac{2\mu}{m\omega_{x,y,z}^2}}$ is the Thomas-Fermi radius and $n_0 = \mu/g = \frac{15N}{8\pi R_x R_y R_z}$ is the peak density. The BEC density simply follows the inverse parabola distribution.

2.3 Beyond mean-field theory

2.3.1 Lee-Huang-Yang correlation

GP theory is a mean-field theory which is only valid for $na^3 \ll 1$. As we increase the na^3, the impact of quantum fluctuation is captured by Lee-Huang-Yang (LHY) correlation [101] to the mean-field energy. Recently, it was observed under some specific condition that the quantum fluctuation would keep a bosonic mixture from collapse by the mean-field attraction force. After a positive followed by a negative feedback loop, the balance between the mean-field and the quantum fluctuation term form a self-trapped quantum gas named droplet. The phenomenon can be observed with relatively weak interaction but an extremely high density. The LHY correlation gives the first beyond-mean-field form of the energy density of BEC, which is

$$\varepsilon = \frac{gn^2}{2}\left(1 + \frac{128}{15\sqrt{\pi}}\sqrt{na^3} + ...\right). \tag{2.12}$$

The first term of the equation is the mean-field energy and second term is the LHY correlation. It is only a perturbation theory and will not work for strongly interacting areas. Recently, there are a lot of beyond-mean-field studies related to this term, which is applied for both bosonic mixture and dipolar condensates [102–107].

2.3.2 Three-body recombination

Until now most of the interactions we are talking about come from the two body elastic collision since the inelastic collision is forbidden by the energy, momentum and spin conservation. However, the statistics nature of quantum mechanics allows for the collision of three bosons together, which is called three-body recombination [12, 108–110]. When three atoms collide, two free atoms form a molecule with the binding energy converted into the kinetic energy and the kinetic energy is distributed to the dimmer and the remaining atom. With the participation of the third atom, the energy and momentum are still conserved and both the atom and dimmer will fly away from BEC since the binding energy is usually much larger than the chemical potential μ. Because the inhomogeneous of the harmonic trap, the three-body recombination is more likely to happen near the centre of the trap, which is the coldest part with largest density. The atoms in the trap centre with lower energy are more likely to be removed, resulting in heating of the system. This heating process is opposite to the evaporative cooling and is referred to as anti-evaporation.

For two-body collisions, the probability of two atoms colliding is proportional to a^2, which is exactly from the scattering cross section σ. If we replace two colliding atom as a single atom, the probability of one more atom entering the collision gives another a^2 factor and thus the chance of three-body recombination is proportional to a^4 [111]. We also know that the total cross section of two-body collisions is proportional to the density n and the factor should be n^2 for three-body recombination. The loss rate of the atoms in cloud should be

$$\frac{\dot{N}}{N} = -L_3 n^2, \tag{2.13}$$

where N is the total number of the atoms and L_3 is the three-body recombination rate (or loss coefficient). The general three-body recombination rate is

$$L_3 = C\frac{3\hbar}{m}a^4. \tag{2.14}$$

C is a constant depending on system and the sharp increase of the three-body losses is the main limiting factor for the experiments related to strongly interacting Bose gas

2.3.3 Efimov physics

In 1970, Efimov predicted an infinite series of trimmer bound states for three identical particles interacting via two-body force [112]. The theory is originally proposed for nuclear physics but there is no success for the detection in nuclei so far. However, Efimov theory's universality allows it to be applied to a wide range of fields in low energy physics [113]. And the strongly interacting Bose gas is very interesting since the quantum statistics allows for a three-body bound state [114]. Though it is counter-intuitive that the trimmer bound state still exists with repulsive two-body interaction. The Efimov state was first observed by the three-body loss rate in strongly interacting ultracold caesium gas [115]. And the observed three body recombination rate L_3 is modified with a log-periodic structure by a bunch of Efimov states. The original work by Efimov is based on three identical particles. However, the Efimov physics can even be applied to our heteronuclear mixture with some modification [20, 116]. Recently, it is suggested that the energy of the Bose polaron near unitary regime will be significantly influenced by the avoid crossing between polaron and first Efimov trimer state [85, 87]. This effect will be discussed later.

3

Improved systems for the cooling, trapping, manipulation and detection of atoms

A stable and robust system is crucial for the cold atom experiment, which includes the cooling, trapping and manipulation of the atoms. The building of the first system of this lab starts from 2010, I am now the fifth graduate student who works with this machine and the second student mainly works on the Rb-Na mixture. The first system was originally designed for the molecular experiment and we have observed the first ground state molecule [36] and heteronuclear spin dynamics [24] in this system. The building and constructing of the first system is well documented by my predecessors' paper and thesis [117–120]. However, many specifications of this old system did not fit the requirement of the new experiment such as Bose polaron. In this chapter, I will present the improvements I made to upgrade the performance of this old system.

3.1 The preperation of double BEC

Before introducing the improvements we made, I will first give a breif introduction on the preperation of double BEC samples of ^{23}Na and ^{87}Rb in our system. Through many experiments are not started from the dual species BEC, we can easily tune it by adjusting the cooling processes which control the number and temperature of the samples.

The general sequence of the experiment follows standard techniques used in today's quantum gas lab. We use dispenser source for both ^{23}Na and ^{87}Rb. Since the vapor pressure of ^{23}Na is usually very small, we use light-induced atomic desorption (LIAD) to increase the density of Na. LIAD is an atomic analogue of the photoelectric effect, which uses weak non-resonant light to desorb atoms from the walls of the chamber. In an ultra-high vacuum (UHV) system, the ^{23}Na and ^{87}Rb atoms are slowed down and loaded in dual magneto-optical trap (MOT). When MOT loading is finished, the phase-space density (PSD) of the atoms are further increased by compressed magneto-optical trap (CMOT), which increases the restoring force and reduces the near resonance photon scattering. Then we turn off the magnetic field gradient for MOT, which is generated by the magnetic quadrupole trap (QT). After CMOT, We use optical molasses to further decrease the sample temperature for the ^{23}Na and ^{87}Rb. Finally, nearly all the ^{23}Na and ^{87}Rb are optical pumped to the spin down ground state $|F = 1, m_F = -1\rangle$ by the optical pumping laser. Since CMOT, optical molasses and optical pumping only takes several milliseconds and the spin down state is low field seeking, the samples is then recaptured by the magnetic quadrupole trap.

In the magnetic trap, the detuned microwave is enabled to modify the trap potential of ^{87}Rb and the evaporative cooling is processed by gradually tuning the microwave frequency and power. Since modified potential removes the high temperature ^{87}Rb atoms near the edge of the trap, the ^{87}Rb atoms is cooled during the evaporation. At the same time, ^{23}Na atoms are cooled by the elastic collision with the ^{87}Rb atoms, which is known as the synthetic cooling. However, the loss of atoms by the spin-flip occurs at the centre of QT, where the magnetic field is close to zero. The loss mechanism called Majorana loss is first predicted by Majorana [121] and this loss will increase at low temperature. During the evaporation, when the size of the sample becomes smaller or the gradient of the magnetic trap is lowered, this so called Majorana loss will decrease the atom number and increase the sample temperature by the anti-evaporation process.

To eliminate the Majorana loss and heating, one dipole trap beam is used to generate a potential dip which near the magnetic field zero point. The dip is so low that the atoms with lower temperature are more likely to stay

in the potential dip rather than the magnetic field zero point. However, the potential should not be too low since the three-body loss will occur when the sample density becomes too high, this is especially important for the heavy Rb atoms. After the microwave evaporation, the atoms are loaded into a crossed optical dipole trap (XODT) and magnetic quadrupole trap is off after the loading process.

In the optical dipole trap, further evaporative cooling is performed by lowering the dipole trap power. Since the trap depth for ^{87}Rb is usually much deeper than ^{23}Na in a 1070 nm trap, the ^{23}Na atoms is evaporated and ^{87}Rb atoms is coooled synthetically. Finally the both species can be cooled to the temperatures well below the critical temperature of Bose-Einstein condensation. Since the sample is much smaller in the XODT, the homogeneous magnetic field is allowed to be used for the state preparation of a desired hyperfine state by the MW and rf pulse. This magnetic field can also be used for tuning interactions via Feshbach resonances. From this point, the samples are prepared for the experiments, which will be presented in the next two chapters.

With achieving the double BEC of ^{23}Na and ^{87}Rb in optical dipole trap, we can tune the relative number of ^{23}Na and ^{87}Rb to prepare the thermal-BEC mixture. For example, if more ^{87}Rb atoms are kept in trap after MW evaporation, more ^{23}Na atoms will be evaporated in optical dipole trap and we can prepare the ^{23}Na thermal and ^{87}Rb BEC mixture. On the contrary, with a very small numer of ^{87}Rb atoms, the efficiency of ^{23}Na atoms' evaporative cooling will be much higher thus we can prepare the ^{87}Rb thermal and ^{23}Na BEC mixture.

3.2 The optimization MOT loading

As the first step of the experiment, the number of the atoms trapped in MOT will affect the atom number of all the following processes. Through MOT is a standard and widely used technique, the quantitative analysis is hard due to the combination complex three-dimensional polarized light and magnetic quadrupole field. Except this, the light-assisted inelastic collisions also affect the number of both Rb and Na, thus we have to push

the Rb MOT away from the trap centre. Despite the complexity and the imperfection, some basic knowledge can still help us to improve the MOT number.

From the atomic physics textbook [95], we know the photon scattering force of the atom in magneto-optical trap is

$$F_{MOT} = -\alpha v - \frac{\alpha\beta}{k} z, \tag{3.1}$$

where k is the wavevector, v is the speed of atom, z is the position from trap centre, α is the coefficient depending on photon-atom interaction and β is the coefficient depending on magnetic field gradient. The first term $-\alpha v$ is the damping force which slow down speed of atom and the second term $-\frac{\alpha\beta}{k} z$ keeps the atoms at around trap centre. In experiment, the best setting of α and β is achieved by tuning the trap beam power, frequency and magnetic field gradient.

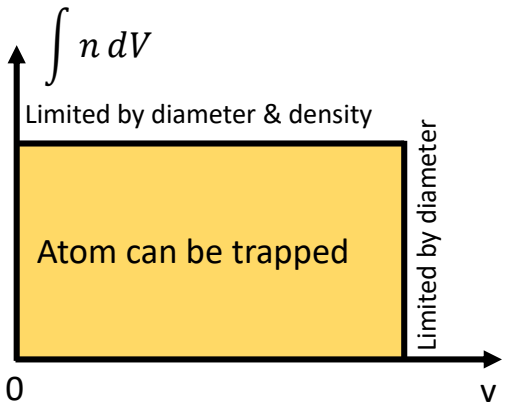

Fig. 3.1. The MOT loading range of the atoms in vacuum chamber. The axis defines the maximum atom velocity that can be traped and the vertical axis shows the number of atoms within the trap volume.

Not all the atoms in cell can be trapped in MOT, it depends on the recoil velocity and lifetime of the atom's excited state. As illustrated in Fig. 3.1, if the atom is moving too fast, the damping force may not large enough to slow down the atom speed within the range of the trap. Increasing the trap volume V or the trap beam diameter will work but the laser power is limited by technical problem. On the other hand, we can also increase the background atom density n in cell but the lifetime of the sample will be

affected by the one-body loss under poor vacuum. And that is the reason why there is a separated MOT chamber for most advanced systems.

To increase the atom density, dispensers is enough for ^{87}Rb but insufficient for ^{23}Na. This problem can be solved by using the Zeeman slower [122] or 2D MOT [123]. However, we use dispensers for both species and we found the Na number is mainly limited by the low background atom density after once I tried to increase the current of the dispenser to 4 A (We normally use 3 A maximum). Through the good vacuum condition will suddenly be destroyed by the impurities in dispenser if we apply a current higher than 2A, we found a great amount of Na can be coated near the glass-to-metal transition part of the chamber if we apply 4 A with only 30 minutes. After firing, the Na dispenser is disabled until the next time we run out of the Na atoms (that takes several months!). The recovery of the system from bad vacuum takes around 4 days for the ion pump and sometimes the titanium sublimation pump (TSP) is also needed.

Light-induced atomic desorption (LIAD) effect [124, 125] is utilized to temporarily increase the background atom density or the atomic vapor pressure. With the help of LIAD, we can get the best possible use of the Na and Rb atoms coated and absorbed in the Pyrex glass chamber. When the vapor pressure is increased, not only the MOT loading rate will increase, the MOT loss rate due to the density gradient between the inside and outside of the trap is also decreased. The rate equation and the saturated value of the MOT atom number are

$$\frac{\mathrm{d}}{\mathrm{d}t}N = R - [KP(t) + \Gamma]N, \tag{3.2}$$

and

$$N_S = \frac{R}{KP(t) + \Gamma}, \tag{3.3}$$

where R is the MOT loading rate, Γ is the constant MOT loss rate, $P(t)$ is the background vapor pressure and K is the constant that relates the vapor pressure to the MOT loss rate. The saturated MOT number will increases as we increase the loading rate as well as the background vapor pressure. LIAD only increase the vapor pressure of Rb and Na, the vacuum condition is quickly recovered in few seconds after we disabled the LIAD. To get the

saturated atom number, the MOT loading time is 25 s for daily operations of our system.

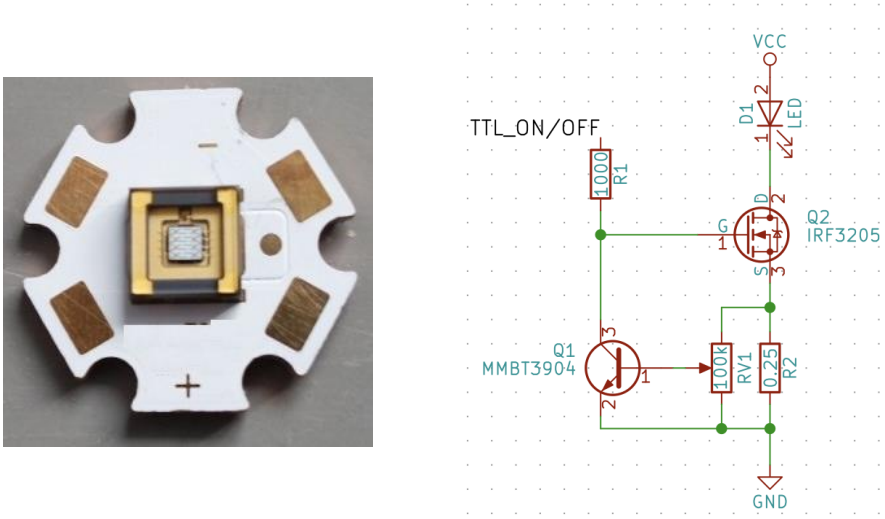

Fig. 3.2. The UV LED setup. Left: The new UV LED (NICHIA NVSU333A-U365) used to replace the old one. The high power LED is reflow soldered on a copper-based PCB which is mounted on a heatsink on the backside. Right: The homemade current driver circuit of the LED, which provide a constant 4 A current when TTL is in high level.

To increase the MOT loading rate, the UV LED with a maximum output power of 200mW (Thorlabs M365L2) is replaced with a homemade reflow soldering LED (NICHIA NVSU333A-U365) on a copper-based PCB. The maximum output power is 3.64 W and the wavelength is still 365 nm. The best position of the UV LED is found to be near the glass-to-metal transition part, which is near the coating of Na. The fluorescence of Na MOT is too small to be separated from environmental noise. However we can confirm the tremendous improvements of the atom number at later stages. After the optimization of all the following steps, the maximum pure BEC number of Na increased from 10^5 to around 4.5×10^5. The MOT number of Rb is increased with around 40%, which should be contributed by the both UV and the increasing of the MOT laser power.

It should be noted that, the increasing of the final BEC number is not achieved by simply increasing the UV light power or the trap power. The fine adjustment of all the parameters related to the change of MOT atom number is necessary.

3.3 The optimization from microwave evaporation to dipole trap loading

After the molasses and optical pumping, around 80% of Rb and Na is pumped to the low-field-seeking $|F = 1, m_F = -1\rangle$ state. The QT is then ramped up and nearly all the low-field-seeking state atoms are trapped. At the same time, one optical dipole trap beam ramped up, which adds a dip to the trapping potential. The centre of the dipole trap is horizontally shifted around 70 μm from magnetic gradient centre and decreases the spin-flip rate of the atoms near zero-point of the magnetic field from trappable state to non-trappable states. This configuration is called hybrid trap and the detailed trap potential and time sequence can be found in the thesis of former graduates [119].

3.3.1 Microwave evaporation

In the quadrupole trap, ^{87}Rb atoms are evaporatively cooled selectively while ^{23}Na atoms are cooled sympathetically. To selectively evaporate ^{87}Rb atoms, radio frequency (RF) transitions can not be used since ^{23}Na and ^{87}Rb have the same Zeeman splitting under low magnetic field. Instead we use microwave (MW) with a frequency around 6.8 GHz, which is close to the $|1, -1\rangle$ to $|2, -2\rangle$ transition of ^{87}Rb. The MW evaporation is started from 6794 MHz and stopped at around 6833.7 MHz.

However, the dipole trap potential of ^{23}Na is only one third of the ^{87}Rb for dipole trap of 1070 nm and the Majorana loss of ^{23}Na becomes severe when the sample temperature gets lower. In order to decrease the Majorana loss of ^{23}Na, the magnetic field gradient of quadruple trap is decreased from 160 G/cm to 64 G/cm, which effectively push away the zero-point of the magnetic field. Thus the microwave evaporation is divided into two part (i) MW frequency from 6794 to 6822 MHz and (ii) MW frequency from 6822 to 6833.7 MHz. The typical number and PSD of Rb and Na during the first part is shown in Fig. 3.3.

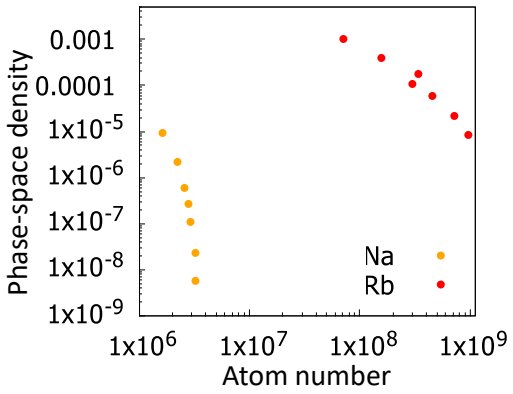

Fig. 3.3. The atom number and phase-space density of both species during the evaporative and sympathetic cooling of the first part. The microwave frequency sweeps from 6794 to 6822 MHz with variable ramping speed and power, which is optimized step by step. The data comes from the documentation of system condition.

3.3.2 Instability problem of ^{87}Rb atom number

For polaron experiment, we need Rb atom number be small and Na BEC be as large as possible. This goal can be easily achieved by changing the ending frequency of microwave evaporation of the second part. However, as we increase the ending frequency, the number fluctuation of Rb atom number loaded in XODT suddenly goes up. This sudden increase can not be explained by detection noise or the quantum fluctuation on the order of $\sqrt{N}$ [126]. The observed fluctuation is shown in Fig. 3.4.

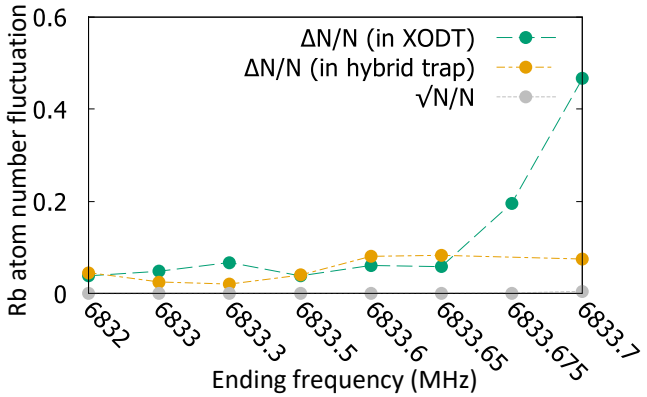

Fig. 3.4. The atom number fluctuation and ending frequency of ^{87}Rb's MW evaporation in QT. The green and yellow data points shows the number fluctuation of ^{87}Rb after and before being loaded into the XODT. ΔN is from the statistic error and $\sqrt{N}/N$ is shown for comparison.

At the same time, We also measure the number fluctuation of the Rb atoms in hybrid trap without ramping the QT and optical dipole trap. As shown in Fig. 3.4, the atom number of ^{87}Rb in hybrid trap is relatively stable but some condensate of ^{87}Rb is found for 6833.6 MHz and 6833.65 MHz, which is not observed in XODT. The temperature of ^{87}Rb sample is around 350 nK at 6833.59 MHz. For higher frequency, the condensate part disappeared since the density of ^{87}Rb dropped much faster than the temperature. As shown in Fig. 3.5, we can find the huge fluctuation is accompany with the sharp decrease of the ^{87}Rb's atom number. Thus the three-body loss is a possible reason of the instability if we consider a condensate of around 10^5 ^{87}Rb atoms being loaded into the XODT with an averaged trap frequency around 500 Hz.

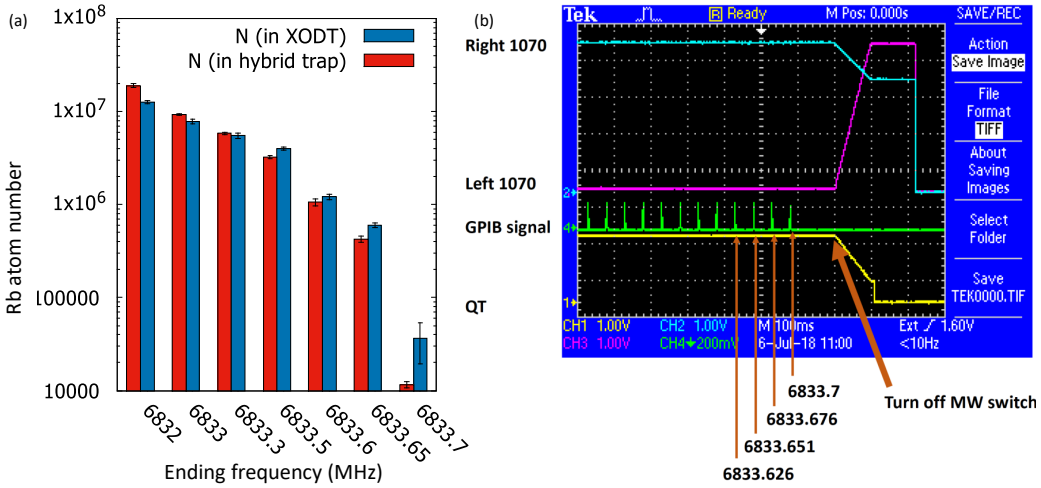

Fig. 3.5. The loading of ^{87}Rb atoms from hybrid trap to XODT. (a) The measured number of Rb atoms in hybrid trap and after the XODT loading. (b) The loading process recorded by the oscilloscope, which includes the intensity of XODT, microwave frequency command and magnetic field gradient of QT.

Through the condensate of ^{23}Na is also found in XODT when it is sympathetically cooled by ^{87}Rb, the number fluctuation of ^{23}Na is always below 5%. However, it is not very surprising since the mass and trap depth of ^{23}Na is much smaller than ^{87}Rb and density for ^{23}Na is not high enough to see a significant loss in few hundred milliseconds. During the microwave evaporation in hybrid trap, we found that a large trap depth can increase the Na atom number but a stong loss of Rb atoms occurs when the trap frequency is too high.

3.3.3 The microwave removal of ^{87}Rb atoms

Since the instability comes from the ^{87}Rb condensate, from experiment we found that the number of ^{87}Rb should not be less than 2×10^5 at the end of microwave evaporation. However, the number of ^{87}Rb atoms is hard to be decreased in 1070 nm dipole trap since the trap depth of ^{87}Rb is 3 times of ^{23}Na and the ^{87}Rb atoms are sympathetically cooled by ^{23}Na atoms during the evaporative cooling. Through the Rb atoms cools evaporatively for smaller trap depth due to its large gravitational sag, the overlap of Rb and Na will also be affected.

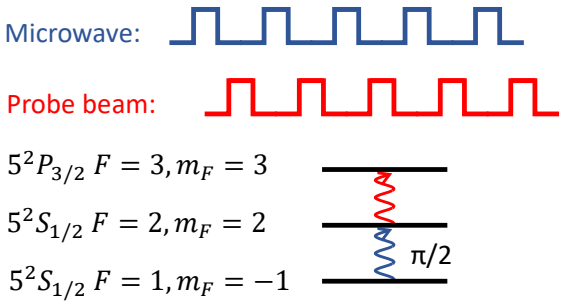

Fig. 3.6. The pulse sequence used to remove the Rb loaded in XODT. Microwave pulse transfer half of the Rb atoms to the F=2 state and then being removed by probe beam. Five pulses are shown in this figure.

Instead of improving the evaporative cooling, we use microwave and probe beam pulse sequence to remove most of the Rb atoms loaded in XOT. As shown in Fig. 3.6, half of the Rb atoms are transferred from $|1,1\rangle$ to $|2,2\rangle$ by the a $\pi/2$ pulse and pushed away by a resonant probe laser pulse. The probe pulse takes only several microseconds thus the sample will not be heated and $1/2^N$ of atoms are left after N pulses. Finally, the short-term number fluctuation of Rb in XODT is less than 20% for 10^4 atoms.

A high power microwave amplifier is needed for short $\pi/2$ pulse, which minimize the influence of magnetic field fluctuation. Since the commercial products are too expensive, we build high power microwave power amplifier (Cree CMPA5585025F) with a GaN field-effect transistor (FET) and a preamplifier (Mini circuits ZX60-83LN-S+). As shown in Fig. 3.7 (c), the working frequency ranges from 5.5 to 8 GHz and the maximum output power is tested to be around 17 W at 6.9 GHz. However, as indicated by Fig. 3.7 (a), some special technique is needed to control the DC operating

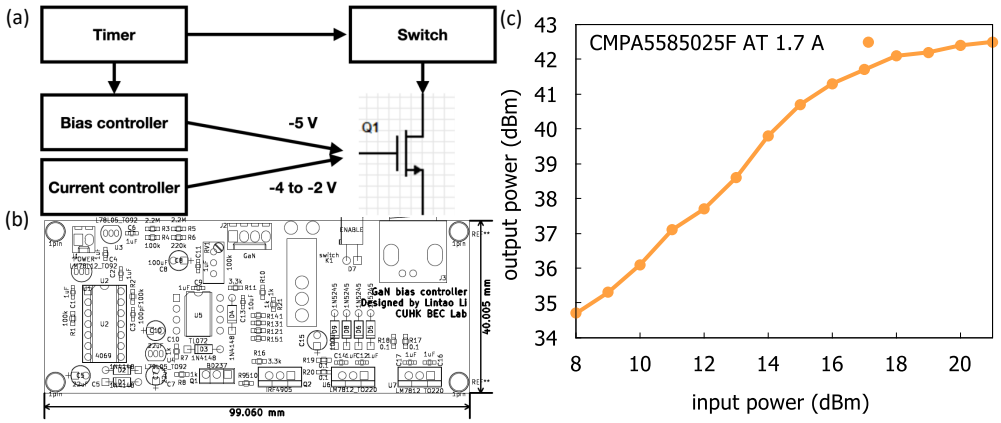

Fig. 3.7. The homemade high power microwave amplifier. (a) The block diagram of GaN bias controller. (b) The PCB layout of the GaN bias controller. (c) The testing result of the GaN module's gain and output power at 6.9 GHz.

point since the thermal breakdown is very common for GaN devices. And a negative gate voltage should always be applied before applying the drain current for the GaN FET. The details about the driver circuits can be found in the appendix Sec. A.3.

3.4 A modified optical dipole trap with better overlap between two species

The dipole trap [127] allows the spin degree of freedom and tuneable interactions of the system. The evaporative cooling in optical dipole trap is also essential for producing the ultra-cold atomic mixture. Due to the requirement of the high power for hybrid trap, a multi-mode 1070 nm fiber laser (IPG Photonics YLR-1070 series) is used for the evaporative cooling of both the hybrid trap and XODT. After the cooling in hybrid trap, the sample temperature is on the order of 1 μK and loaded into the crossed trap with a power around 1 W and a beam waist around 60 μm. For the preparation of ^{23}Na BEC, after the evaporation, the power of each beam will finally lower to around 0.2 W. As shown in Fig. 3.8, for this 1070 nm optical dipole trap, under same trap power, the trap depth of ^{87}Rb is usually much larger than

^{23}Na. During the evaporation, the ^{23}Na is evaporatively cooled and ^{87}Rb is thermalized sympathetically.

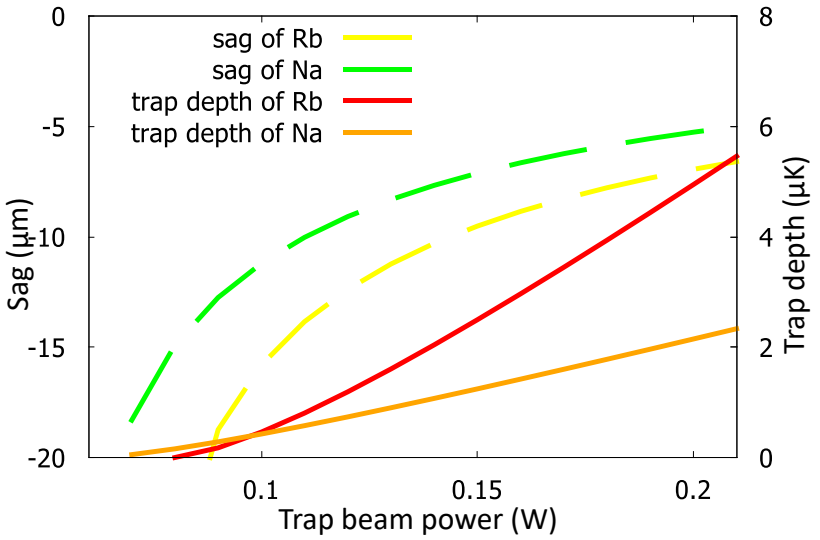

Fig. 3.8. The trap depth and gravitational sag as a function of a 1070 nm crossed dipole trap power. The beam waist is set to 55 μm for the calculation, which is similar to the parameter of the experiment.

However, the trap frequencies are different for the two species, when we lower the trap beam power, finally, the relative sag between the species will be too large for simultaneous condensation of both species. As shown in Fig. 3.8, the relative gravitational sag of the two species is increased as trap power is lowered. When the relative sag is comparable to the size of atomic cloud, the overlap between the different species becomes bad and affects the sympathetic cooling of ^{87}Rb. However, since ^{87}Rb is heavier than ^{23}Na, the gravitation pulls ^{87}Rb downwards with greater force and this allows the evaporative cooling of ^{87}Rb under an extremely low trap power. In Fig. 3.8, we can find the trap depth of ^{87}Rb is truly smaller than ^{23}Na when the trap beam power is less than 0.1 W. However, under such low power, the relative sag between ^{87}Rb and ^{23}Na BEC becomes very large. The overlap problem is especially obvious for our ^{23}Na-^{87}Rb mixture since the double BECs of ^{87}Rb and ^{23}Na are immiscible. We can also use the Feshbach resonance to tune the phase seperation, a detailed research related to this miscible and immiscible mixture can be found in the previous work of Fudong Wang [42]. To decrease the relative sag, we had to increase the beam power for better overlap after the evaporative cooling. With such

a deep optical potential, the heating effect is rather obvious and the BECs would become not so pure after several hundred milli-seconds.

3.4.1 The gravitation sag free trap

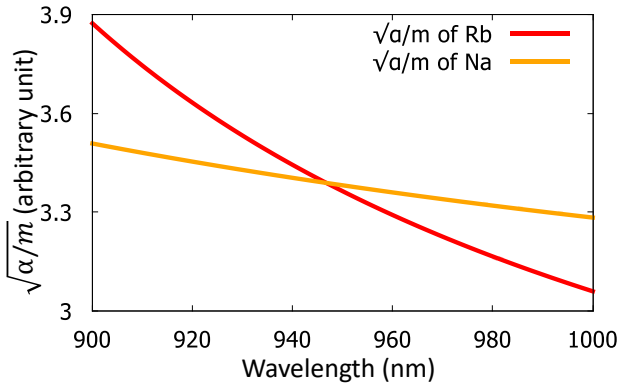

Fig. 3.9. The trap frequency ($\propto \sqrt{\alpha/m}$) of Rb and Na as the function of trap laser wavelength. The calculation base on the polarizability given by the parametrize results.

For the polaron, spinor or any experiments based on the interaction between two different species, the overlap of the wavefunction is very important. For the vertical direction, we can decrease relative gravitational sag of the two species by tune the wavelength of the trap beam since the polarizability of the atom depends on the frequency of the photon. For the harmonic trap, if we consider the balance between gravity and photon scattering force of the trap, the gravitational sag is

$$sag = \frac{g}{(2\pi f_y)^2}, \tag{3.4}$$

where g is the gravity constant and f_y is the trap frequency on vertical direction. The trap frequency f_y is propotinal to $\sqrt{\alpha/m}$, where α is the polarizability (real part) and m is the mass of the atom. And the same gravitational sag means the trap frequency should be same for both ^{87}Rb and ^{23}Na atoms. The frequency-dependent AC polarizability of the ground

state ns for the alkali-metal atom can expressed as the summation over all possible transitions [128]:

$$\alpha_{ns}(\omega) = \frac{2}{3\hbar}\sum_{n'}\left(\frac{\omega_{n'p_{1/2}}\langle n'p_{1/2}|\, D\,|ns\rangle}{\omega^2_{n'p_{1/2}} - \omega^2} + \frac{\omega_{n'p_{3/2}}\langle n'p_{3/2}|\, D\,|ns\rangle}{\omega^2_{n'p_{3/2}} - \omega^2}\right), \tag{3.5}$$

where $|ns\rangle$, $|n'p_{1/2}\rangle$ and $|n'p_{3/2}\rangle$ are individually the ground state and excited state with two different J, $\langle n'p|\, D\,|ns\rangle$ is the reduced dipole matrix element, $\omega_{n'p}$ are corresponding transition frequency and ω is the laser frequency. After some simplification, we can calculate the $\sqrt{\alpha/m}$ for both ^{87}Rb and ^{23}Na. As shown in Fig. 3.9, the wavelength that gives same gravitational sag for Rb and Na is around 947 nm.

The optical dipole trap we used in our experiments origins from a 2 W tapered amplifier (DILAS TA-0950-2000), which amplifies an external cavity diode laser (ECDL) with 40 mW output power (with the laser diode from Sheaumann Laser M9-940-0100-D5P). After the isolator, the power is split for the crossed dipole trap with half-wave plates and polarizing beam cubes as shown in Fig. 3.10. Two polarization maintaining fibers (Thorlabs P3-780PM-FC) are used to guide light from laser board to machine table where two custom cage system are used to mount the output collimating lenses.

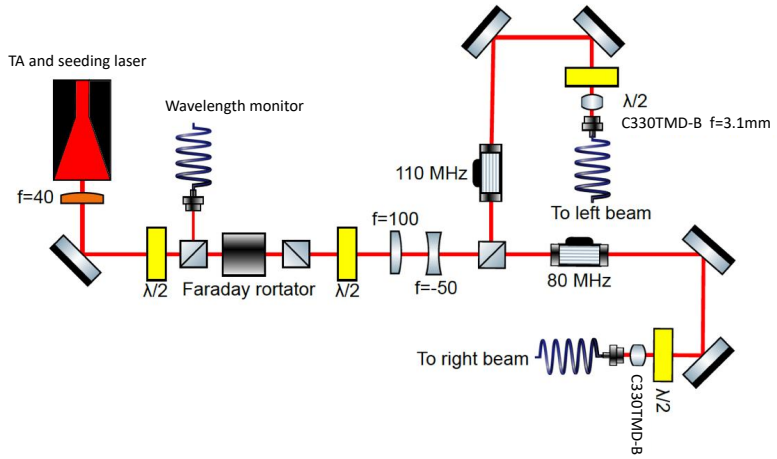

Fig. 3.10. Schematic illustration showing the layout for our 947 nm laser for the crossed optical dipole trap.

The collimator is designed for a pancake-shaped trap with a beam waist around 35 μm (110 μm) for vertical (horizontal) direction. After many

failed attempts including using different lenses and mounts, we finally settled on current setup. The astigmatism and spherical aberration are the main source of trouble in the setup of the collimator. The spherical aberration is mainly limited by the collimating lenses and only the aspherical lens with a small focal length shows a good behaviour. The reason of using a small focal length is that its numerical aperture (NA) can be much larger than the NA of fiber and the missing of the laser power beyond the NA of the lens will cause the spherical aberrations. The aspherical lens is also necessary for minimizing the aberration. On the other hand, the misalignment of lenses will cause the astigmatism.

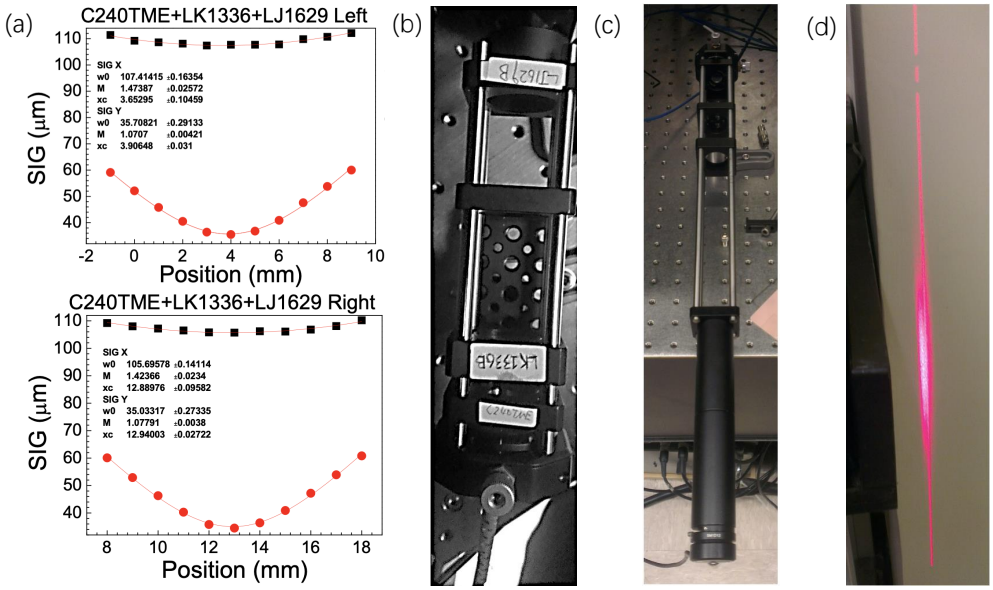

Fig. 3.11. The homemade collimator with cage system. (a) The beam profile after the collimator. (b) The collimator. (c) The adjustment of the relative position between the fiber port and aspherical lens. (d) The rotation adjustment of the first cylindrical lens by projecting the diverged beam to the wall.

In our setup, the beam is collimated with an aspherical lens (Thorlabs C240TME-B NA=0.5) to a measured beam diameter around 1.8 mm and a 3× beam expander formed by two cylindrical lenses (Thorlabs LK1629-B, LJ1336-B) is used to expand the beam diameter on vertical direction. The numerical aperture (NA) of fiber is 0.12, which is much smaller than the NA of collimating lens. As shown in Fig. 3.11 (b), all the lenses are mounted in cage system. We found it extremely helpful to use the a long tube and an aperture with power meter behind to align the centre of col-

limating lenses one by one (see Fig. 3.11 (c)). The astigmatism can be further adjusted in our setup. Since the focus position of vertical direction can be separately adjusted by the distance of the cylindrical lenses, we add a f=300 mm focus lens (Thorlabs LA4579-B) after the collimator and use a camera to check the astigmatism while we adjust the distance. Except the astigmatism between vertical and horizontal direction, we found the difference of the angle between two cylindrical lenses will cause the rotation of the focused beam profile, the angle of second cylindrical lens is also carefully adjusted by continuously checking the beam profile on camera.

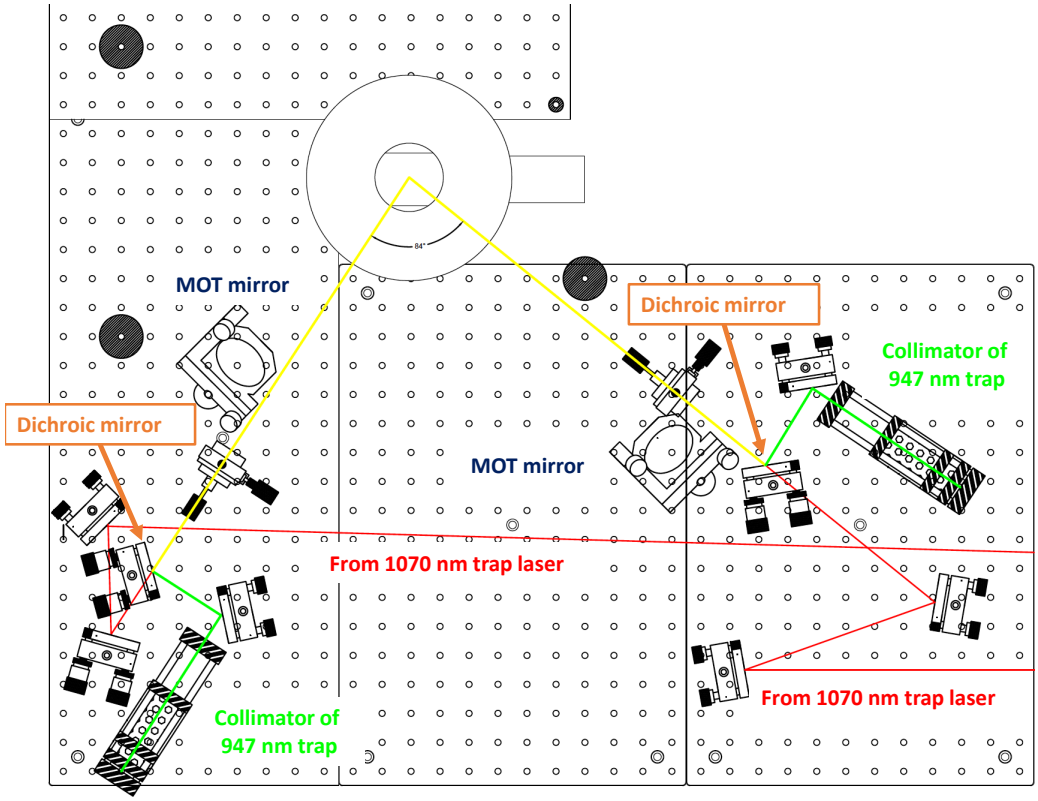

Fig. 3.12. The schematic illustration showing the optical dipole trap setup of the machine table.

However, due to the low beam quality of the tapered amplifier, the efficiency of AOM and fiber coupling is quiet low and the useable power is only 0.5 W. Thus we still use 1070 nm trap to produce the ultra-cold atoms and adiabatically load the them into the 947 nm trap. The optical path of the 1070 and 947 nm laser for one of the trap beam is shown in Fig. 3.12. We found a 300 ms linear ramp is good enough to transfer the atoms from 1070 nm to 947 nm trap as long as the trap depth is kept. After the trap

loading, the ^{87}Rb is thermalized sympathetically again and now we don't have to lower the trap power to cool the ^{87}Rb atomic cloud.

For saving the space, we share the light path of 1070 and 947 nm XODT by using the dichroic long pass mirror (Edmund #87-040). And two beams of different wavelength are focused by same f=300 lens (Thorlabs LA4579-B). We use the camera to check the focus position of both the 1070 and 946 nm laser beams and we adjust the lenses of 1070 nm trap laser to make sure that the focus of two beams are overlapped. During this online testing, we found the dichroic mirror can introduce quite amount of astigmatism thus we readjusted the collimators. In addition, it should be noted that the screws and rings of the mirror mount should not be too tight because the tension will cause the curvature of mirror. And the Ø2" mirror has smaller curvature than Ø1" mirror since it is much thicker.

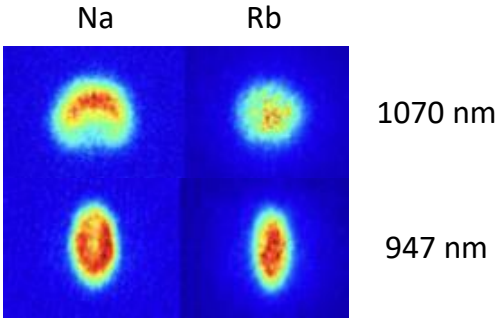

Fig. 3.13. Typical images of dual BEC after 18 and 23 ms TOF for ^{23}Na and ^{87}Rb respectively. We show the images from both 1070 and 947 nm crossed optical dipole trap.

Since the density of BECs are too large for the absorption image in trap. The atoms are detected by absorption imaging after time-of-flight (TOF) expansion. The dipole trap is abruptly switched off and atoms are expand freely. And the shape of BEC sample after TOF expansion is dominated by the interaction energy between atoms. Typical images of dual condensates in 1070 and 947 nm trap are shown in Fig. 3.13.

As shown by the upper panel of Fig. 3.13, two species are not concentric to each other. Because, for the ballistic expansion of 1070 nm trap of a power around 0.2 W, the calculated gravitational sag between ^{23}Na and ^{87}Rb is comparable to the Thomas-Fermi radius of the BECs. Since the trap is a spherical trap, both ^{23}Na and ^{87}Rb clouds are ball-shaped after the ballistic

expansion. However, we can find a notch at lower part of the ^{23}Na cloud due to the repulsive ^{23}Na-^{87}Rb interactions, which can be reproduced by numerically solving the coupled G-P equations [42].

After loading the samples from 1070 nm trap to 947 nm trap, we wait another 300 ms before the expansion. Since the 947 nm trap is a pancake-shaped trap with higer trap frequency in the vertical direction, the faster expansion of vertical direction elongate the cloud size of both ^{23}Na and ^{87}Rb after TOF. Because the differential gravitational sag is supposed to be zero in this trap, we do not expect to see any asymmetrical shape for ^{23}Na cloud. As shown by the lower panel of Fig. 3.13, instead of the notch at lower part, we can find a decreasing of ^{23}Na column density at the centre of the cloud. Because, as a result of the repulsive interaction, the ^{23}Na BEC density is suppressed by ^{87}Rb BEC at the centre of the trap, which can also be reproduced by the numerical simulations.

We also evaluate the trap frequency ratio between ^{23}Na and ^{87}Rb by directly measure the trap frequency using parametric heating method [127]. We hold the ^{23}Na (^{87}Rb) thermal clouds in trap with a 10% modulation depth for laser power. And we tune the modulation frequency and measure the corresponding cloud size with TOF, which indicates the sample temperature.

Fig. 3.14 shows the comparison between the measured and calculated trap frequency ratio under the trap wavelength ranges from 937.5 to 965.5 nm. For the trap frequency calculation, we use the given polarizabilities and trap beam parameters to calculate the trap potential, which includes the gravity and gravitational sag. We can find the measured trap frequency ratios for 946.8 and 956.4 nm are close to the calculated value. However we found a relatively large divergence for the data points at 937.5 and 965.5 nm. One possible reason for this is the laser frequency measurement. Since both two wavelengths are close to the edge of TA's operation range and there might be multiple frequency modes which affects the measurement of the wavelength meter.

The $\sqrt{\alpha/m}$ indicates a "magic wavelength" at 946.66 nm [128]. Finally, we select 946.8 nm, which gives a trap frequency difference smaller than 0.5%

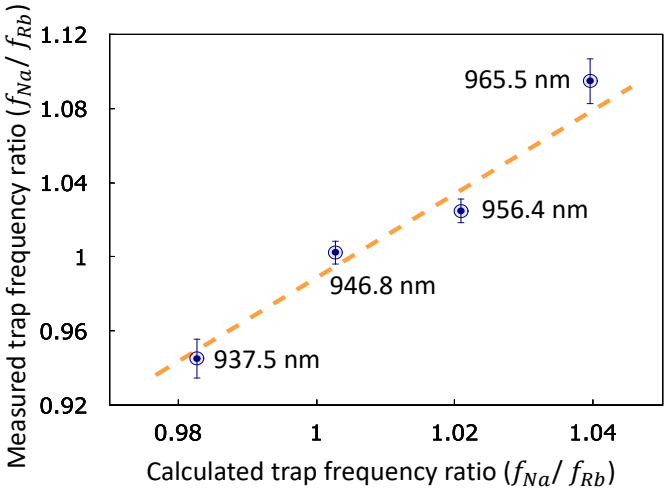

Fig. 3.14. The measurement of the trap frequency ratio between ^{23}Na and ^{87}Rb under the trap wavelength ranges from 937.5 to 965.5 nm. The horizontal axis represents the calculated trap frequency ratio, and the vertical axis shows the measured trap frequency ratio by parametric heating method. The orange curve is the linear fitting for eye guiding.

and we haven't found any significant photoassociation loss for ^{23}Na-^{87}Rb mixture.

3.4.2 The selective trapping of Rb

Through the trap frequency of Rb and Na is same in 947 nm trap, the size of the atom cloud in trap is still different. For thermal cloud, the size of the sample is $\sqrt{2k_BT/m\omega^2}$, where ω is same for ^{87}Rb and ^{23}Na but the size of ^{23}Na arom cloud is around two times of ^{87}Rb. Due to this reason, we use the mixture of ^{23}Na BEC and thermal ^{87}Rb samples for polaron experiment, which provides a relatively good wavefunction overlap between two species. However, we found there is still a significant amount of thermal ^{87}Rb atoms are outside of the ^{23}Na BEC, which affect the measurement of the rf spectroscopy.

To increase the wavefunction overlap, we apply a species dependent trap potential for ^{87}Rb in horizontal direction and the trap laser wavelength is selected to be 805 nm. Since the wavelength is close to ^{87}Rb's D2 line, the

trap intensity can be relatively low and will not affect the trap potential of the ^{23}Na atoms. As shown in FIg. 3.15, the beam is collimated with an aspherical lens (Thorlabs C110TMD-B) to a beam diameter around 0.6 mm and being focus by a f=100 lens (Thorlabs AL50100H-B) which is originally designed for the image system in vertical direction. The focused beam waist is measured to be around 52 μm and the trapdepth of ^{87}Rb is around 1.2 μK for 5 mW.

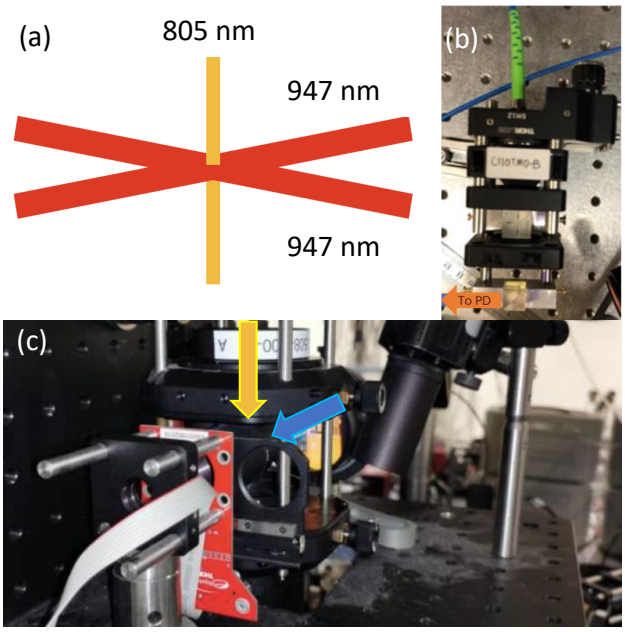

Fig. 3.15. The 805 nm trap for ^{87}Rb. (a) The schematic illustration showing the vertical 805 nm trap together with the 947 nm pancake-shaped trap. (b) The collimator of 805 nm laser. (c) The electro mechanical slider (Thorlabs ELL6K) above the vacuum cell. The slider is used to reflect the focused MOT beam (blue) or pass the vertical trap beam (yellow).

For given laser power, the horizontal trap frequency of Rb is measured to be around 82 Hz and the heating rate of ^{87}Rb is calculated to be smaller than 40 nK/s. Compare with the trap frequency of Na, the trap frequency of Rb is 60% larger in horizontal direction, which significantly improve the polaron signal. We will discuss about this in the polaron experiment section.

3.5 The optimization for high stability magnetic field

The stability of magnetic field is extremely important for tuning the Feshbach resonance and the radio frequency (rf) spectroscopy. The rf spectroscopy is also the main detection method of polaron physics. Here, I will first introduce the evaluation and analysis of the magnetic field stability and then discuss about the design of a high stability magnetic field servo system.

3.5.1 Evaluation and analysis of the magnetic field noise by rf pulse

The radio frequency spectroscopy of the single atom or a bunch of atoms without interaction is the best way to precisely determine the local magnetic field. Since the transition is dipole forbidden, there is no damping and power broadening effect and the natural linewidth of atom is extremely narrow. And the behaviour of the atom can be well described by an ideal two-level system.

Since the frequency response of the transition is extremely narrow, the population oscillation of the atom is the Fourier transform of the external field under small pulse area. The atoms select out the frequency component of rf signal that in resonance and convert it into the population of excited state: the stronger the signal, the higher the fraction of excited state. Since the pulse duration is always limited by other loss mechanisms, linewidth of the rf pulse is usually much larger than the natural linewidth of the transition. Thus the population of the excited state is directly the line shape of the rf signal.

For example, we apply a square rf pulse with a frequency ω_0 and duration T. As shown in Fig. 3.16, the Fourier transform of the pulse (b) is the convolution of the square pulse lineshape (c) and single frequency rf signal (d). This is exactly the convolution theorem. The atom act as a single frequency filter with an extremely narrow natural linewidth, if we scan the ω_0 around

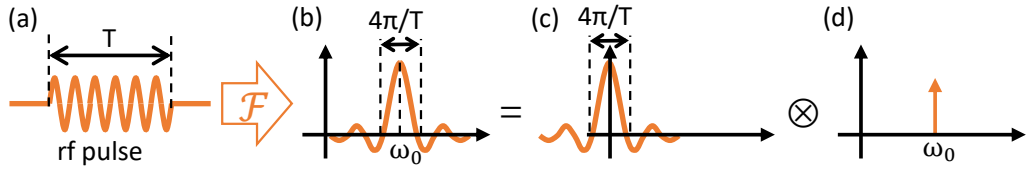

Fig. 3.16. The square rf pulse. (a) The rf pulse in time domain, which is the product of the square pulse and rf signal in time domain. (b) The rf pulse in frequency domain, which is the convolution of the square pulse (c) and rf signal (d) in frequency domain.

the resonance frequency of the atom, we can get the linewidth of the rf pulse by the population of the atom in excited state. However, it should be noted that the pulse area must be small to get a linear response.

On the other hand, the external field includes two parts, one is the AC field of rf signal, another is the DC magnetic field. The magnetic field decides the resonance frequency of the atoms and the noise of magnetic field will in turn affect the linewidth. Thus it is important to know how the magnetic field noise affects our measurement in frequency domain. The simplest idea is that if the frequency of noise is much higher than inverse of pulse duration, the noise will not be significant during the measurement. Thus the rf pulse is actually a low-pass filter for the noise of magnetic field and its transfer function is exactly the Fourier transform of the pulse line shape.

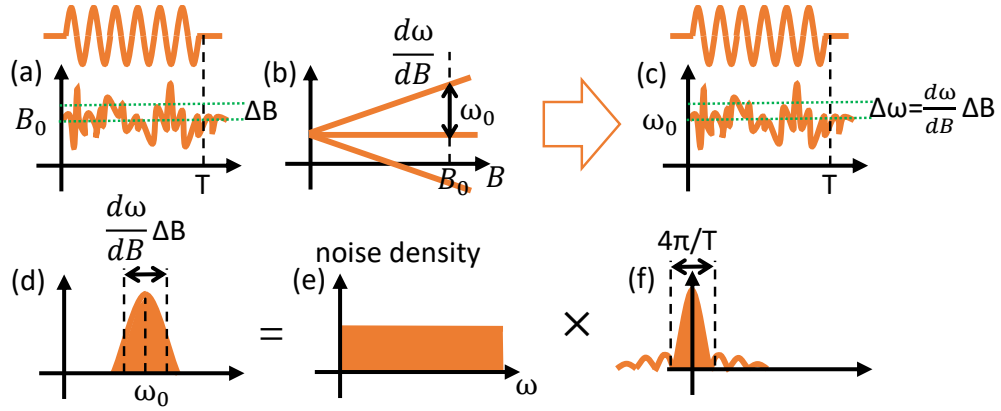

Fig. 3.17. The broadening of the linewidth by magnetic field noise. (a) The magnetic field noise in time domain. (b)(c) The Zeeman splitting that converts the magnetic field fluctuation into the fluctuation of resonance frequecny. (d) The magnetic field noise broadened rf lineshape. (e) The noise density of magnetic field, use white noise as example. (f) The lineshape of the pulse (amplitude), which acts as a low-pass filter.

For example, we still use a square rf pulse with a frequency ω_0 and duration T, as shown in Fig. 3.17. The fluctuation ΔB of the magnetic field at B_0 cause the fluctuation $\Delta\omega$ of atom's resonance frequency ω_0. And the coefficient between the magnetic field and resonance frequency is decided by the Zeeman splitting. During the rf pulse, the noise of the magnetic field (e) is low-pass filtered by the linewidth function of the square pulse (f) and the total noise ΔB is

$$\Delta B = \sqrt{\int_0^\infty \left| sinc(\frac{T}{2}\omega) \right| B_n(\omega)^2 \mathrm{d}\omega}, \tag{3.6}$$

where $B_n(\omega)$ is the noise density of the magnetic field and T is the rf pulse duration. However, the equation doesn't include the contribution from the long term drift, which will limit the pulse duration to hundreds of milliseconds. Through the noise density is independent from the rf pulse, the magnetic field noise we measured by rf pulse is relevant to the pulse duration. In experiment, we first scan the line shape of the pulse by tune the rf frequency and then we fix the rf frequency at the slope of line shape, thus the population fluctuation of excited state can be connected to the noise of magnetic field.

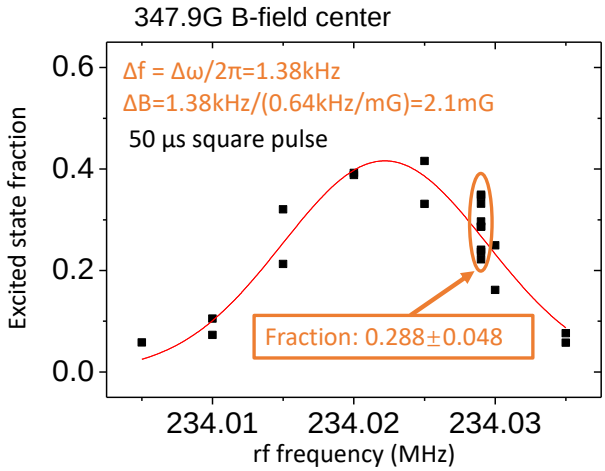

Fig. 3.18. The testing of magnetic field at 347.9 G. The $|1,0\rangle$ to $|1,1\rangle$ transition of ^{87}Rb is used with applying a 50 μs square pulse.

As shown in Fig. 3.18, the total magnetic field noise given by the standard error of excited state fraction on the slope is 2.1 mG for the 50 μs pulse. However, this noise is not equivalent to the short term stability, one of

our test shows the fitting of the line shape gives a centre frequency of 234.0222 MHz in Fig. 3.18 and the value is 234.0217 MHz after 2 hours, which corresponds to a drift around 0.8 mG.

If the white noise is dominant, we can also calculate the noise density of the magnetic field. Here, we ignore the sidelobes of sinc function and the total area of the filter gives:

$$\int_0^{2\pi/T} sinc(\frac{T}{2}\omega)(B_n)^2 \mathrm{d}\omega \approx \frac{\pi}{T}(B_n)^2 = (\Delta B)^2. \tag{3.7}$$

Thus the noise density of the magnetic field is

$$B_n = \Delta B\sqrt{\frac{T}{\pi}}. \tag{3.8}$$

For T=50 μs and ΔB=2.1 mG, the noise density B_n is 3.3 μG/$\sqrt{Hz}$. And if we consider the magnetic field noise within 100 kHz, the total noise should be 1.1 mG. It should be noted that during our test the linewidth of the rf pulse should be much larger than the standard deviation of ω_0 since the line shape is also affected by the magnetic field noise.

3.5.2 Type of noise in a servo system

So far we have described the procedure which enable us to evaluate the noise of the magnetic field. But we still need to know where these noise come from and how to achive the desired noise level of magnetic field. First of all, there are basically four kinds of technical noise in our system [129]:

- Long-term drift.
- Temperature coefficient.
- Wideband noise.
- Interference.

Long-tern drift means the drift of system over multiple months to many years [130]. This drift mainly comes from the aging of resistor, Zener

diodes, transistors or other electrical components and it also links to the 1/f noise in semiconductors. Since the magnetic field should always be calibrated by atoms first and the experiment are finished within several hours. We don't need to worry to much about the long-tern drift. However, we should always care about the long-term drift when we are selecting the electrical components. A system with small long-tern drift save you a lot of time and you will otherwise struggle all day long to find several atom transitions.

Temperature coefficient mainly comes from the sensor, operational amplifier, voltage reference (Zener diode) and resistors. It is usually expressed in ppm/°C (parts per million per degree Centigrade) units. Similar to the long-tern drift, the temperature varying within several hours may not to be much. However, the temperature coefficient of regular electrical components can be hundreds to thousands of ppm/°C, which sometimes can cause a very bad stability of the system. For the temperature coefficient, we need to understand how the drift of one component affect the overall drift of the system, which is very important for the analysis of system performance. Another important thing is to isolate the sensitive operational amplifier from the power resistors and transistors on circuit board and the thermal gradient on circuit board will cause the thermoelectric effect [131].

The wideband noise includes thermal noise (Johnson−Nyquist noise), contact noise and shot noise. The contact noise widely exists in vintage carbon resistors and it is not a problem now. The shot noise and thermal noise exist in semiconductor. However, thermal noise is the main source of noise of a metal film resistor [132, 133]. The thermal noise and shot noise are flat frequency spectrum which is same as the white noise in the example of the evaluation part. However, it is hard to tell whether shot noise or thermal noise is dominant for the wideband noise exists in current transducer (sensor), operational amplifier, voltage reference, digital-to-analog coverers or any active components. What we have is the effective input or output noise density of the individual component, which is given by the datasheet. Finally, a good magnetic field system is free from the temperature coefficient and the wideband noise limit the performance of the rf spectroscopy.

Interference is the noise source outside of the servo system, for example, the noise of switched-mode power supply and the 50 (60) Hz power line noise. Some interferences like the ripple of the power supply can be stabilized by servo system but the interferences like the residue magnetic field from nearby transformers can not be canceled.

3.5.3 The calculation of noise

The block diagram of the magnetic field system is shown in Fig. 3.19. The magnetic field we need is around 350 G, which beyond the range of usual magnetic field Hall sensor. Instead of measuring the magnetic field, we use current transducer to detect the current of magnetic coil. The value given by the transducer is compare with the setting value and the error signal is produced to give the feedback of the current in coil.

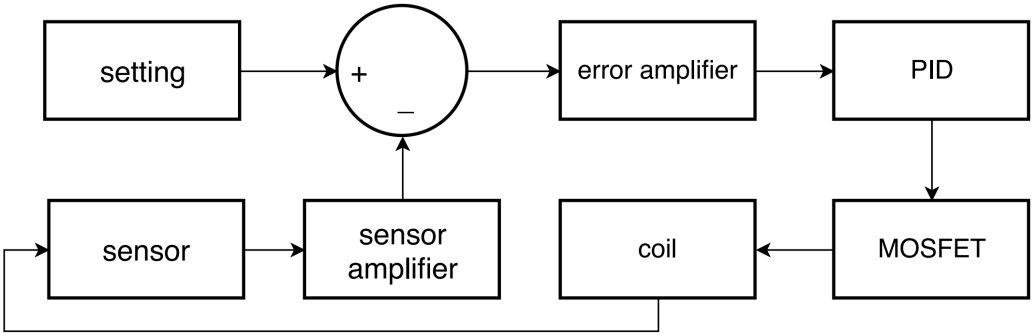

Fig. 3.19. Block diagram for the magnetic field servo system.

As you can find in Fig. 3.19, the different part has different contribution to the noise of magnetic field. For example, the noise of sensor and sensor amplifier will strongly affect the noise of the magnetic field since the measurement may be wrong. The noise of setting value and error amplifier will also destroy the stability since the feedback might be wrong. However, the noise contribution of PID, MOSFET, power supply or any component that do not handle the weak or accurate signal is small and any of the interference will be compensated by the feedback system since the current is being monitored. This can also be understand by the noise model of a multiple stage amplifier shown in Fig. 3.20.

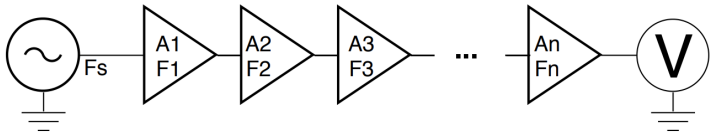

Fig. 3.20. Block diagram of a multiple stage amplifier to compute overall noise.

In Fig. 3.20, the overall effective noise expression at the signal source is

$$F = F_s + F_1 + \frac{F_2}{A_1} + \frac{F_3}{A_1 A_2} + ..., \tag{3.9}$$

where F_s is the noise level of signal source, A_i is the gain and F_i is the noise level of each stage of the amplifier. For an ideal amplifier, the overall effective noise at the signal source is still F_s. However, we can find that only the noise of first stage is dominant as long as the gain A_1 is large enough. For our case, since the PID, MOSFET and power supply are after the error amplifier, the noise of them are not dominant for the overall noise.

Considering the effective noise at the output of current transducer, we give the dominant noise term in the block diagram of magnetic field system in Fig. 3.21. The overall effective noise at the current sensing side is

$$\begin{aligned} i_{total}^2 =& i_{HALL}^2 + \left(\frac{e_{A_1}}{R_s}\right)^2 + \left(\frac{e_{DAC}}{A_1(s)R_s}\right)^2 + 2\left(\frac{e_{R_1}}{A_1(s)R_s}\right)^2 + \left(\frac{i_{A_2}R_1}{2A_1(s)R_s}\right)^2 \\ &+ \left(\frac{2e_{A_2}}{A1(s)R_s}\right)^2 + \left(\frac{2R_2 e_{TUNE}}{A_1(s)A_2(s)R_3R_s}\right)^2 + \left(\frac{2(R_2+R_3)e_{SUPPLY}}{A_1(s)A_2(s)Y(s)R_3R_s}\right)^2, \end{aligned} \tag{3.10}$$

where:

- $A_1(s)$ is transfer function model of the differential amplifier for the current transducer.
- $A_2(s)$ is transfer function model of the error amplifier.
- $Y(s)$ transfer function model of the PID, MOSFET and coils together.
- i_{HALL} is the noise of current transducer.

- e_{A_1} is the input voltage noise of the differential amplifier, which includes the input noise of operational amplifier and thermal noise of feedback resistors.

- e_{A_2} is the input voltage noise of the error amplifier, which includes the input noise of operational amplifier and thermal noise of feedback resistors.

- i_{A_2} is the input current noise of the error amplifier, which cannot be neglected here since R_1 is relatively large.

- e_{DAC} is the noise level of reference voltage, which includes the noise of the Zener diode and the digital to voltage converter.

- e_{R_1} is the thermal noise of the resistor with value R_1.

- e_{TUNE} is the voltage noise at the magnetic field trim port, which is connected to the PXI 6733 DAC board.

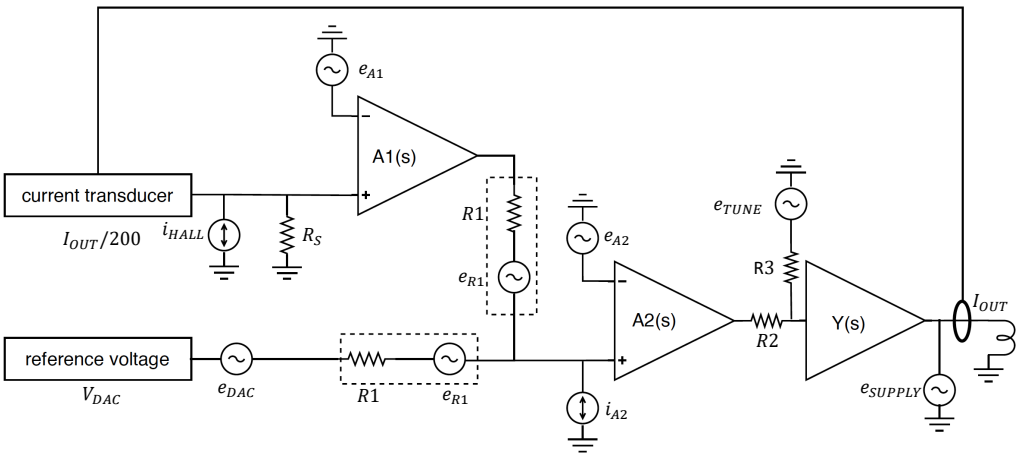

Fig. 3.21. Noise analysis block diagram for the magnetic field servo system.

Except the term i_{HALL}, all the noises come from the servo system and i_{HALL} is the only thing that we can not optimize. Thus our job is to design a servo that gives noise level, drift and bandwidth better than the performance of current transducer.

3.5.4 The design of servo system

We use a high stability current transducer (LEM IT 200-S) with very low temperature drift and noise level. This current transducer generates a secondary current that proportional to the primary current but reduced by a factor of 1000. Tab. 3.1 summarizes the relative parameters given by the datasheet. We can converted the parameters into the current of the

Parameters	Min	Typ	Max
Conversion ratio		1:1000	
Secondary current (mA)	-200		200
Long-term stability (ppm/month)			1
Temperature coefficient (ppm/K)			2
Small signal bandwidth (kHz)	0	500	
Noise density from 0 to 50 kHz (ppm/$\sqrt{Hz}$)			0.07

Tab. 3.1. Parameters of the IT 200S current transducer. All ppm figures refer to full scale which corresponds to a maximum secondary current of 200mA.

transducer's output. Thus the temperature drift is 0.4 μA/°C and the noise density is 14 nA/$\sqrt{Hz}$. According to the drift and noise level of the current transducer, we select the operational amplifiers, the resistors, the voltage references and DACs that meet our requirement. All the relative components are shown in Fig. 3.22.

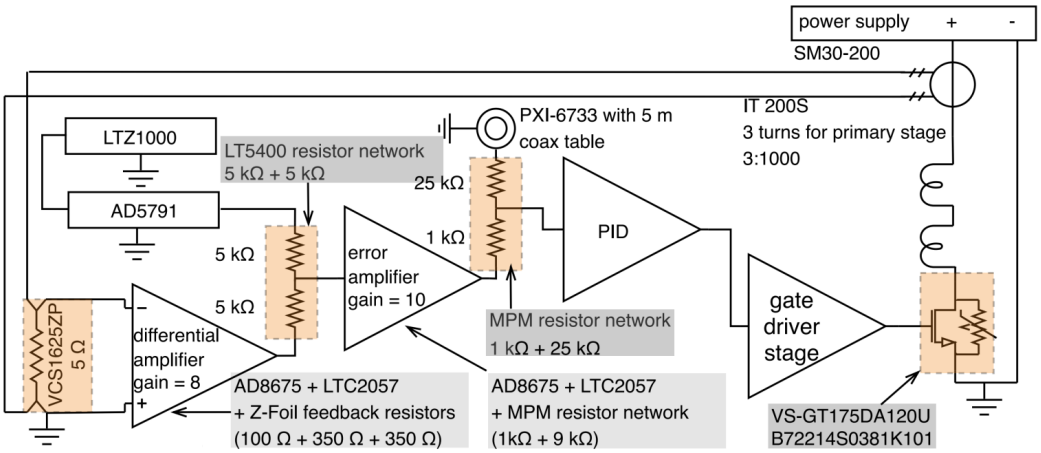

Fig. 3.22. Schematic implementation for the magnetic field servo system.

The current of the Feshbach coil is only around 47 A for 350 G. However, the range of the current transducer is 200 A. Thus we use 3 turns for the

primary stage and we have the full dynamic range of the current transducer. The sensing resistor convert the current output of the transducer into voltage and its temperature drift is only 0.05 ppm/°C, which is much smaller than the transducer. For the amplifiers, we use the chopper stabilized operational amplifier to correct the voltage drift and the drift at the input stage is 15 nV/°C, which corresponds to only 3 nA/°C. The high gain stability of differential amplifier is achived by using the feedback resistors with very low temperature drift (0.2 ppm/°C) and we use very low feedback resistance to decrease the thermal noise of the differential amplifier. The bandwidth of the differential and error amplifier is 2 and 0.8 MHz, which is good enough for the feedback. The temperature drift of the voltage reference (AD5791+LTZ1000) is better than 0.1 ppm/°C, which is also much better than the transducer. We summarize the contribution of noise in Tab. 3.2, the calculation is based on the equation 3.10. We can find

Source	Maximum drift (nA/°C)	noise (nA/$\sqrt{Hz}$)
Current transducer	400	14
VCS1625ZP resistor	10	0.06
Differential amplifier	40 (from resistors)	1.2
LT5400 resistor network	40	0.3
Voltage reference	20	1.3
Error amplifier	4 (from resistors)	0.2
MPM resistor network	3	0.1
External tuning port	3	0.02

Tab. 3.2. The noise contribution from different part of magnetic field system. The calculation is based on the equation 3.10 and the parameters are given by the datasheet. The maximum drift of the resistor is calculated by the full dynamic range, which are 200 mA for current transducer's output and 10 V for external tuning port.

that the performance of the magnetic field system is determined by the noise of current transducer. Since the a good PID controller provides an infinite gain for the $Y(s)$ within the bandwidth we desired, the e_{SUPPLY}'s contribution is not given in Tab. 3.2. And the total noise should be close to the performance of the current transducer. We use the current noise to calculate the maximum noise of the magnetic field:

$$B_n = 14nA/\sqrt{Hz} \times 1000 : 3 \times 7.5G/A = 35\mu G/\sqrt{Hz}. \tag{3.11}$$

However, the current noise will be low pass filtered by the Feshbach coils and the magnetic field noise will becomes lower for the frequency above several kHz. Our measurement gives an average noise density of only around 3.3 μG/$\sqrt{Hz}$ but the frequency range of the integration is 200 kHz and we suppose the noise density is irrelevant to the frequency. However, we can say that the noise level of the magnetic field is comparable to the performance of the current transducer.

3.5.5 Tips for the magnetic field servo system

Decreasing the influence of high power components

When we calculate the influence temperature drift, we think the temperature of components is same to the environment. However, it is not the case for sensing resistors, Zener diodes and power transistors. The power dissipation of them can cause the temperature gradient on PCB board and cause the drift of themselves and nearby components.

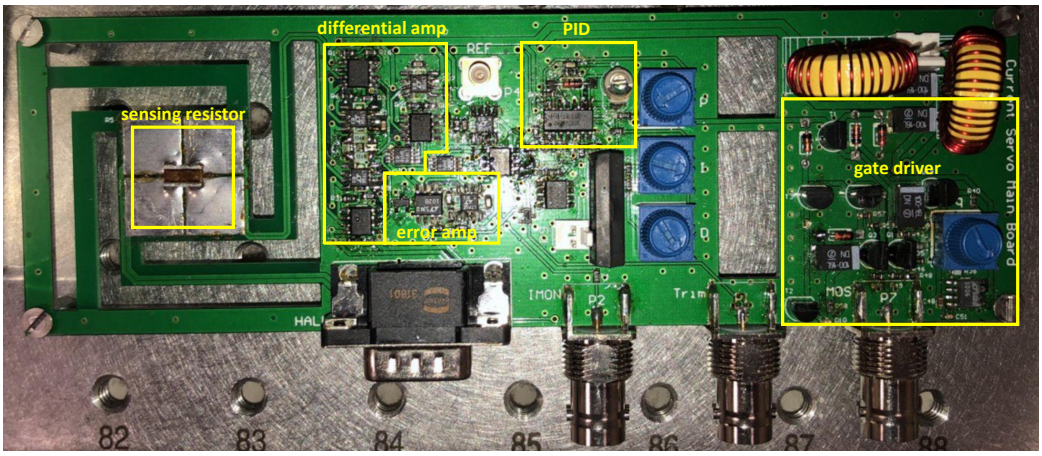

Fig. 3.23. The PCB layout of the servo board for magnetic field system.

The design of servo board is shown in Fig. 3.23, for the sensing resistor, a large soldering pad can provide a relatively small thermal resistance between the resistor and environment. And the high precision resistor networks and operational amplifiers can be thermally isolated by the slots on PCB. Through the temperature gradient between the components and

surrounding environments is inevitable, the repetition of same experiment sequence can still provide a relatively high stability from shot to shot.

Ground connection

There are always multiple connection of ground in the magnetic field servo system. However, the potential of ground is important for the control of magnetic field. In our design, the voltage reference board (AD5791 and LTZ1000) and servo board are closely connected in the chassis to avoid any interference between the ground potential of two boards. And the ground of chassis is directly connected to the optical table to avoid any interference from outside. The high current path on ground should be avoided, thus we use a homemade isolated power supply to isolate the ground of the power supply. For the current transducer, the output and return line should be directly connected to the driving side of the sensing resistor by 4-wire connection. And only one sensing side of the resistor can be connected to the ground thus we can avoid any error caused by the ground path (Actually, we didn't connect any ground for sensing resistor, the connection is inner the current transducer). Other ground path includes the magnetic field trim port, digital signal receiving of DAC and driving of the MOSFET. They are either not so sensitive to the interference of ground potential or can be compensated by the closed loop.

Increasing the slew rate of the current

The ramping speed of the magnetic field is limited by $\frac{\mathrm{d}I}{\mathrm{d}t} = \varepsilon/L$, where I is the current, L is the inductance and ε is the electromotive force (emf) of the coils. If we increase the current, the speed is limited by the maximum voltage of the power supply. The maximum voltage of the power supply is 30V and the maximum ramping up speed is around 120 G/ms. If we want get a faster speed, the inductance of the coil should be kept very small [134].

However, the ramping down of the current will produce the reverse electromotive force, which is the limitation of the slew rate since the emf is directly applied to the drain and source of the MOSFET. And a varistor

is need to limit the maximum voltage across the MOSFET, as shown in Fig. 3.22. To increase the ramping down speed, we replace the MOSFET (IXYS IXFN520N075T2) with the high voltage IGBT (Vishay VS-GT175DA120U) and the ramping down speed is increase from 500 G/ms to 5000 G/ms.

Thermal instability of the MOSFET or IGBT in linear mode

The development of MOSFET and IGBT enable us to use only one or two IGBT or MOSFET modules instead of using dozens of power bipolar junction transistors. However, the power transistor today are designed for the on and off for switching applications, which only needs the transistors be fast and show low on-state resistance ($R_{DS(ON)}$). However, these advantages of new devices are not ideal for operating in linear mode, which we control the R_{DS} by the transconductance of the transistor. Fig. 3.24 shows

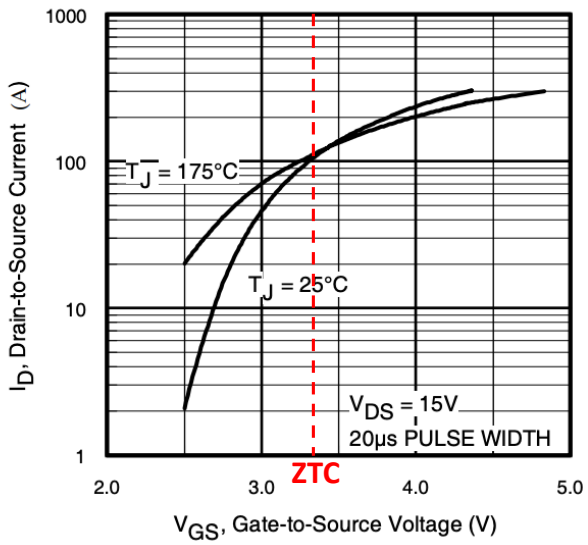

Fig. 3.24. A typical I_{DS} vs. V_{GS} response curves of a MOSFET showing converging point of ZTC.

the I_{DS} vs. V_{GS} curves of a certain power MOSFET. You can find a point where the drain current as a function of gate voltage is independent from temperature. The zero temperature coefficient point (ZTC) indicates the gate voltage at which the DC performance of the device remains constant with temperature.

The power MOSFET (IGBT) consists of millions of individual unit "cells" making up the total device structure [135, 136]. Below the ZTC, any increase in the cell temperature will cause the higher drain current of this cell and it will pull in current from its neighbours and having more current conducted through it, which makes the cell temperature become even higher. Thus a possible thermal runaway can occur below ZTC and a very large current noise can be found. Through the servo system are trying to control the current by gate voltage but the runaway occurs again and again.

Compared with old MOSFET (IGBT), the ZTC point becomes much higher for the new devices, which means V_{DS} (V_{CE}) should be kept relatively low when we need a stable current. Otherwise the V_{GS} will be below the ZTC point and the thermal runaway will happen. In other words, we need a high power supply voltage when we ramp up the magnetic field but we need to lower it when we need a stable magnetic field.

3.6 The antenna for hyperfine state manipulation and rf spectroscopy

In this section, I will first introduce the relevant Zeeman sublevels for $F = 1$ atoms. Then I will introduce two rf antennas that are most frequently used in our experiment. The first antenna is used for the spin flips with rapid adiabatic passage at around 60 G. And the second antenna is used for the rf spectroscopy of polaron experiment, which detects the energy of ^{87}Rb impurities in ^{23}Na BEC background.

3.6.1 The Linear and quadratic Zeeman shift

If we apply a magnetic field B_0 in vertical direction, there will be energy splitting between different Zeeman sublevels. For ^{87}Rb and ^{23}Na, we let

J=1/2, I=3/2, F=1 and expand the series of B_0 to the second order, the Zeeman energy are given by the Hamiltonian

$$\begin{aligned} H &= -\frac{A_{hfs}}{4} + \frac{5g_I - g_J}{4}\mu_B B_0 F_z + \frac{(5g_I - g_J)^2\mu_B^2 B_0^2}{16(2I+1)A_{hfs}}(F_z^2 - 4) \\ &= E_0 + pF_z + qF_z^2. \end{aligned} \tag{3.12}$$

Here, E_0 is a constant, A_{hfs} is the magnetic dipole constant of the atom and F_z is the z component of angular momentum matrix divided by $\hbar$ [137]. For F=1, we define the basis $|1, m_F\rangle = (1,0,0)^T, (0,1,0)^T$ and $(0,0,1)^T$ for $m_F = 1, 0$ and -1 respectively. The three spin operators are given by

$$F_x = \frac{1}{\sqrt{2}}\begin{pmatrix} 0 & 1 & 0 \\ 1 & 0 & 1 \\ 0 & 1 & 0 \end{pmatrix}, F_y = \frac{i}{\sqrt{2}}\begin{pmatrix} 0 & -1 & 0 \\ 1 & 0 & -1 \\ 0 & 1 & 0 \end{pmatrix}, F_z = \begin{pmatrix} 1 & 0 & 0 \\ 0 & 0 & 0 \\ 0 & 0 & -1 \end{pmatrix}. \tag{3.13}$$

Thus the Zeeman energy is

$$E(m_F) = E_0 + pm_F + qm_F^2, \tag{3.14}$$

where $p = \frac{5g_I - g_J}{4}\mu_B B_0 < 0$ is the linear Zeeman energy and $q = \frac{p^2}{(2I+1)A_{hfs}}B_0^2$ is the quadratic Zeeman energy. Through the linear Zeeman energies are same for ^{87}Rb and ^{23}Na, their quadratic Zeeman energies are different.

The above Hamiltonian defines a three-level system. In the spinor experiment, we need the pure ^{87}Rb and ^{23}Na mixture in $|1,0\rangle$ state, which means we need a two-level system to flip the spin state from the initial $|1,-1\rangle$ to $|1,0\rangle$ without considering the exitance of $|1,1\rangle$ state. Thus the quadratic Zeeman energy is important for the decoupling of third energy level. For same reason, the spin flip of Rb and Na can be separated by their different quadratic Zeeman energy. Thus we can prepare the ^{87}Rb$|1,0\rangle$ and ^{23}Na$|1,1\rangle$ mixture for the polaron experiment. We use a magnetic field of around 60 G to separate the rf transition frequencies between different sublevels of ^{87}Rb and ^{23}Na.

3.6.2 The spin flip

The spin flip is achieved by introducing the off-diagonal terms into the Hamitonian of the system. This can be easily done by adding a small rotating magnetic field in the horizontal direction. And this perturbation can be described as $\Omega(cos\theta F_x + sin\theta F_y)$, where θ gives the rotation of field at horizontal plane and Ω is the Rabi frequency that is proportional to the amplitude of the perturbation magnetic field. More theory about the spin flip is discussed in Sec. A.1 and A.2.

3.6.3 The rf antenna

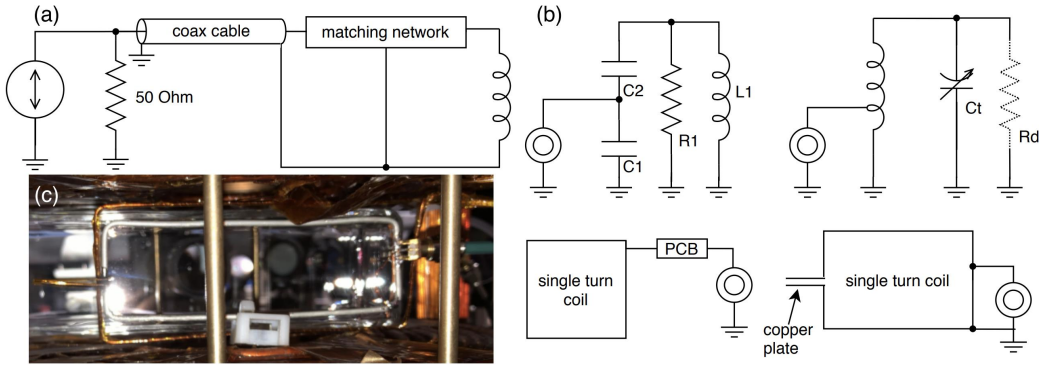

Fig. 3.25. The rf antenna of our system. (a) The general structure of rf antenna including the signal generator, coax cable, impedance matching network and the coil. (b) Two different types of impedance matching networks, which are used for the rapid adiabatic passage at around 60 G and rf spectroscopy at around 350 G respectively. (c) The picture of antennas placed near the vacuum chamber, which includes the antenna for 60 G (orange) and 350 G (silver).

We use the loop antenna to generate the B_{AC} in horizontal direction and thus the Rabi frequency is

$$\Omega = \frac{g_F \nu_B B_{AC}}{2\hbar}, \tag{3.15}$$

where $g_F = (\frac{5}{4}g_I - \frac{1}{4}g_J)$ is the g-factor that accounts for the magnetic dipole moments.

If we want to achieve a very high Rabi frequency, the turns and current of the coil should be as large as possible. However it is not simply to connect the output of the power amplifier to the coil since the impedance of the antenna and amplifier should match each other or otherwise the reflection will destroy the amplifier and the efficiency is low [138]. Except the current, the size of the loop antenna is important for the radiation efficiency. For the antenna that needs to be closely placed around the glass chamber the size of the loop antenna is alway much smaller than the wavelength. This kind of antenna is defined as the small loop antenna. Through the small loop antenna are less efficient radiators for far field, the atoms will only see the near-field B_{AC} which is irrelevant to the far-field antenna pattern [139].

Fig. 3.25(a) shows the general structure of the rf antenna. The output impedance of the rf power amplifier is 50 Ω and the signal is delivered to antenna by passing through the 50 Ω transmission line. At the other side of the coax cable, the matching network convert the inductive load (the coil) to a resistive load, which should be exactly like a 50 Ω resistor. We use Norton equivalent circuit to describe the power amplifier and one half of the current will flow into the matching network and the coil, which means the matching network needs to vary the phase and amplitude of the signal to match the impedance of the coil. For the rapid adiabatic passage at around 60 G and rf spectroscopy of Rb at around 350 G, we built the antenna works at 42 ± 4 and 234 ± 1 MHz.

There are two way to understand the impedance matching, one is to match the inductive load of the coil, the other is to match the effective radiation or the damping resistor across the coil. The second way is better for the understanding of the circuit. We use the resonant circuit formed by inductors and capacitors to "amplify" the voltage of the signal, which provides the same amount of current as the input to the effective resistor.

The loop antenna for 60 G

The design of the antenna is shown in the left panel of Fig. 3.25(b). We first calculate the inductance of the coil, which is single turn with minimum parasitic capacitance. The calculated inductance is around 300 nH. We use

the centre frequency $f = 42$ MHz, thus the effective capacitance in parallel should be

$$C_{parallel} = \frac{C_1 C_2}{C_1 + C_2} = \frac{1}{4\pi^2 f^2 L} \approx 48pF. \tag{3.16}$$

Since the bandwidth is designed to be 8 MHz and centre frequency is 42 MHz, the Q factor should be around 5. Thus the effective damping resistor R_1 should be:

$$R_1 = R_{source}(1 + Q^2) \approx 50(1 + 5^2) = 1.255k\Omega. \tag{3.17}$$

We add the resistor $R_1 = 1$ kΩ to serve as the damping resistor since the Q factor we need is relatively low and the effective resistance given by the loss and radiation of the coil is not important here. Thus R_1/R_{source} gives the ratio of C_1 and C_2:

$$\frac{R_1}{R_{source}} \approx \left(1 + \frac{C_1}{C_2}\right)^2 \approx 20. \tag{3.18}$$

Thus the equation 3.16 and 3.18 limit the value of C_1 and C_2. We use 220 and 47 pF for C_1 and C_2 and a maximum Rabi frequency of around $2\pi \times 20$ kHz is achieved by using a 3 W power amplifier (Mini circuits ZVE-3W-183+). It should be noted that the parasitic capacitance and inductors affect the parameters of the antenna, which can only be adjusted by the online testing results.

The loop antenna for 350 G

For the antenna working at around 230 MHz, the impedance matching circuit board can not be used since the lead cable from coil to the matching circuit will introduce a significant amount of parasitic capacitance. Instead of using capacitor network, we use a autotransformer liked structure to convert the impedance, which is shown in the right panel of Fig. 3.25(b). We select two nodes on the single turn coil to serve as the primary winding of the transformer and the whole coil is the secondary winding. The

inductance is similar to the previous loop antenna and the capacitance in parallel should be

$$C_t = \frac{1}{4\pi^2 f^2 L} \approx 1.6pF. \tag{3.19}$$

which is small but critical. As shown in Fig. 3.25(c), we use a homemade variable capacitor made by two closely placed copper foil and Kapton tape for insulation. The capacitance can be adjusted by bending copper foil and its voltage rating is much higher than the commercial variable capacitor.

For the construction of antenna, we first adjust the copper foil to tune the centre frequency. And then we use the SWR meter to evaluate the impedance matching. By adjusting the node position of the primary stage, we can tune the effective impedance of the antenna. Since we neglected the damping resistor for best efficiency, the bandwidth of the antenna needs to be tested. After the adjustment, the bandwidth is tested to be around 3 MHz and the SWR of the antenna is better than 2 at the resonance frequency.

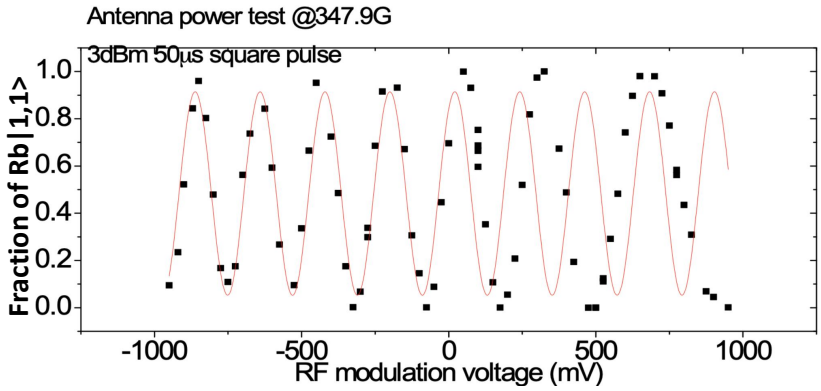

Fig. 3.26. The testing of the rf antenna at 234 MHz. We use a fixed 50 μs square pulse to spin flip the ^{87}Rb atoms from $|1,0\rangle$ to $|1,1\rangle$ state with variable input power ranges from around 5mW to 50W. The nonlinear relation at higher power comes from the satuation of the power amplifier.

For the ejection spectroscopy of polaron experiment, we need a π pulse within several microseconds, which means the antenna should be high power. As shown in Fig. 3.26, we achieve a maximum Rabi frequency at around $2\pi \times 140$ kHz with a 50 W power amplifier (Mini circuits ZHL-50W-52+). The pulse modulation is achieved by a homemade module with a linear in V/V variable gain amplifier (Texas Instruments, VCA824), which

is excellent for modulation since it has linear relation between the modulation voltage and pulse amplitude in voltage (not power).

3.7 The absorption image

Absorption image is one of the most widely used technology to detect the density distribution of the ultracold atom cloud. As shown in Fig. 3.27, the atoms are illuminated by a probe beam and the shadow cast by atoms is imaged on the surface of the charge-coupled device (CCD) of the camera. Since the photons would be scattered to other direction by the atoms, the intensity of probe beam is reduced when it passes through the atom cloud. By comparing the fraction of the transmitted light with the probe beam without the atoms, the column density of atoms in probe beam direction can be measured.

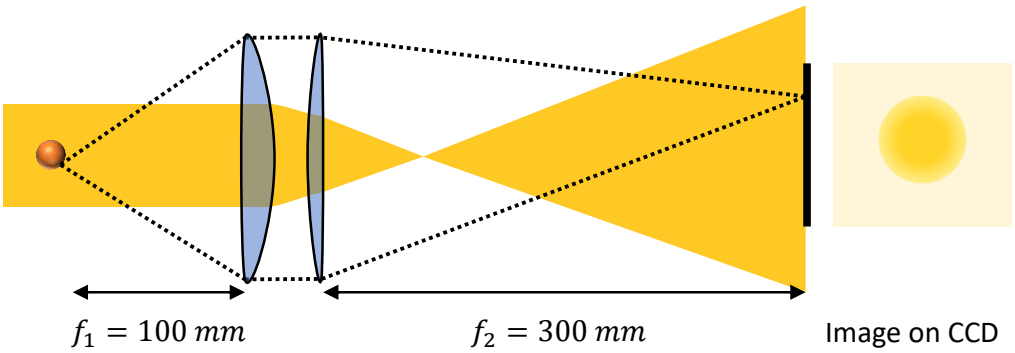

Fig. 3.27. The schematic of the absorption imaging.

3.7.1 The theory of absorption image

We consider a laser beam of intensity I incident on a cloud of atoms with uniform space density n. As illustrated in Fig. 3.28, the probability of the photons being absorbed (scattered) by atoms is $n\sigma(\omega)\mathrm{d}z$, where $\sigma(\omega)$ is the absorption cross section of the atom, ω is the angular frequency of the

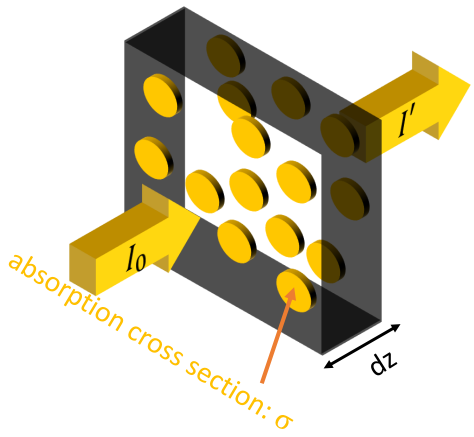

Fig. 3.28. The illustration of absorption image for low atom density.

beam and $\mathrm{d}z$ is the depth of the sample. Thus the attenuation of light passing through the atom cloud is

$$\frac{\mathrm{d}I}{I} = -n\sigma(\omega)\mathrm{d}z, \tag{3.20}$$

which is also known as the Beer's law. However, this law only applies for the low atom density and low probe beam intensity.

Firstly, if the density of atoms is too high, the atoms could be hide behind by the previous atoms. Additionally the photons being scattered by atoms can be reabsorbed by other atoms in the cloud. These two mechanism distort the column density measurement when the atom density is high. Thus we should use the absorption image only when the it is a optically thin cloud.

Secondly, if the intensity of probe beam is high enough, there will be significant amount of atoms that is not in ground state. For the case of two-level system, the significant fraction of atoms will be in excited state, which reduce the probability of absorption. On the other hand, the atoms in excited state could undergo stimulated emission, which leads to the gain of probe beam intensity. And the rate of stimulated emission is equal to the absorption for a two-level system, which is also linked to the equality of the Einstein coefficients $B_{12} = B_{21}$. If we consider the influence from stimulated emission, the equation 3.20 should be rewritten as

$$\frac{\mathrm{d}I}{\mathrm{d}z} = -\left(n_g - n_e\right)\sigma(\omega)I, \tag{3.21}$$

where n_g and n_e are the density of ground state and excited state respectively. Here we haven't consider the effect from spontaneous emission since the momentum distribution of these photons is arbitrary and most of the photons will not be captured by image system.

By considering the energy conservation of the atoms under steady state, we have the relation

$$n_g\sigma(\omega)I = n_e\sigma(\omega)I + n_e\Gamma\hbar\omega, \tag{3.22}$$

where Γ is the rate of spontaneous emission or the decay rate of excited state. And the number conservation under steady state requires

$$n_g + n_e = n. \tag{3.23}$$

Using equation 3.22 and 3.23, the equation 3.21 can be expressed as

$$\frac{\mathrm{d}I}{\mathrm{d}z} = -n\sigma(\omega)\frac{1}{1+\frac{I}{I_{sat}(\omega)}}I, \tag{3.24}$$

where $I_{sat} \equiv \frac{\Gamma\hbar\omega}{2\sigma(\omega)}$ is defined as the saturation intensity for the two-level system. For the two-level system, the cross section is given by

$$\sigma(\omega) = \sigma_0\frac{1}{1+\left(\frac{\omega-\omega_0}{\Gamma/2}\right)^2}, \tag{3.25}$$

where ω_0 is the resonance frequency of the two-level system and $\sigma_0 = \sigma(\omega_0)$ is the on-resonance cross section.

We consider the case for resonance probe beam. The above calculation is applied to a homogeneous sample with density n. But both the column density $n(x,y,z)$ and probe beam intensity $I(x,y,z)$ are inhomogeneous over the space. However, the Beer's law does not limit the inhomogeneous of $n(x,y,z)$ and $I(x,y,z)$ over the probe bean direction z since the absorption image only cares about the column density of the atom which is defined as $n(x,y) = \int_{-\infty}^{\infty} n(x,y,z)\mathrm{d}z$. And each pixel of the CCD integrate the local density of $n(x,y)$ since the path of the probe beam is supposed to be irrele-

vant to the density distribution. The Integration of equation 3.24 gives the optical depth

$$\begin{aligned} OD(x,y) &\equiv \sigma_0 n(x,y) \\ &= \int_{-\infty}^{\infty} \sigma_0 n(x,y,z)\mathrm{d}z \\ &= -\int_{-\infty}^{\infty} \frac{1+\frac{I(x,y)}{I_{sat}}}{I(x,y)} \frac{\mathrm{d}I(x,y)}{\mathrm{d}z}\mathrm{d}z \\ &= -ln\frac{I'(x,y)}{I_0(x,y)} - \frac{I'(x,y)-I_0(x,y)}{I_{sat}}, \end{aligned} \tag{3.26}$$

where $I_0(x,y)$ and $I'(x,y)$ are the probe beam intensity before and after passing through the atom cloud respectively. For the probe beam power that is much smaller than I_{sat}, we can use the optical density given by

$$od(x,y) \equiv -ln\frac{I'(x,y)}{I_0(x,y)} \tag{3.27}$$

to replace the optical depth. The light field $I'(x,y)$ and $I_0(x,y)$ is reproduced on the surface of CCD chip and the intensity distribution is converted to the charge distribution of the pixel matrix. The charges of each pixels are then moving out from the chip one by one and being quantified by the analog-to-digital converter (ADC). And finally we have the signal strength $S(i,j)$ for pixel (i,j). The optical depth is determined by

$$OD(i,j) = -ln\frac{S'(i,j)-S'_b(i,j)}{S_0(i,j)-S'_b(i,j)} - \frac{S'(i,j)-S_0(i,j)}{I^0_{sat}}, \tag{3.28}$$

where I^0_{sat} is the digital counting value of I_{sat}. The signal image $S'(i,j)$ and reference image $S_0(i,j)$ are the pictures taking by camera with and without the exitance of atoms respectively. The background image $S'_b(i,j)$ is the picture taking by camera without the probe beam, which accounts for the dark current and background counting from the camera and environment. And the total atom number is

$$N = \sum_{i,j} n(i,j)A = \sum_{i,j} \frac{OD(i,j)}{\sigma_0}A = \frac{A}{\sigma_0}\sum_{i,j} OD(i,j), \tag{3.29}$$

where $A = A_{pixel}/m^2$ is the effective area of a pixel, A_{pixel} is the area of a pixel in CCD chip and m is the magnification of the image system. We can

find that we can get the atom number N without knowing the coefficient between S(x,y) and I(x,y) as long as the probe beam intensity is much smaller than I_{sat}.

3.7.2 The limitations of absorption image

The limitation of maximum OD

We have previously discussed some of the imperfection of the absorption image of optically thick cloud. However, the imperfection of the system also limit the maximum OD that we can measure. In previous calculation, we suppose that all the photons arrive at the CCD can interact with the atom, which is not true since the probe beam may contain off resonance light and some of the probe light might be scattered into the camera by dust or the imperfections of optical elements without passing through the atom cloud. Thus the maximum optical density of the image system is

$$od_{max} = -ln\left(\frac{I_{incoh}}{I_{coh}+I_{incoh}}\right), \tag{3.30}$$

where I_{incoh} and I_{coh} distinguish the two parts of the probe light. And od_{max} is the maximum optical density we measured for a extremely thick atom cloud. Thus the measurement value of optical density with the exitance of the I_{incoh} is

$$od_{meas} = -ln\left(\frac{I_{incoh}+I_{coh}e^{-od_{real}}}{I_{coh}+I_{incoh}}\right), \tag{3.31}$$

where od_{real} is the actual optical density of the sample. Using the equation 3.30 and 3.31, the od_{real} can be written as

$$od_{real} = -ln\left(\frac{e^{-od_{meas}}-e^{-od_{max}}}{1-e^{-od_{max}}}\right). \tag{3.32}$$

For example, if 3% of probe beam doesn't interact with the atoms:

$$od_{max} = -ln\left(\frac{3}{100}\right) \approx 3.5. \tag{3.33}$$

And we suppose an atom cloud has $OD_{real} = 2.2$ with $I_0 = 0.1I_{sat}$:

$$\begin{aligned} OD_{real} &= od_{real} + \frac{(1 - e^{-od_{real}})I_0}{I_{sat}} \\ &= od_{real} + 0.1 - 0.1e^{-od_{real}} \\ &= 2.2 \end{aligned} \tag{3.34}$$

Thus the od_{real} should be around 2.112 to fulfil the value of OD_{real}. With above mentioned image system, it will gives the optical density:

$$\begin{aligned} od_{meas} &= -ln\left(e^{-od_{real}}(1 - e^{-od_{max}}) + e^{-od_{max}}\right) \\ &\approx 1.913. \end{aligned} \tag{3.35}$$

Thus the measured optical depth should be

$$\begin{aligned} OD_{meas} &= od_{meas} + \frac{(1 - e^{-od_{meas}})I_0}{I_{sat}} \\ &\approx 1.998, \end{aligned} \tag{3.36}$$

which is 10% smaller than the actual value. The maximum od for our system is around 4 for the absorption image of both ^{87}Rb and ^{23}Na and we keep the od_{meas} smaller than 2 for the reliable measurements. This requirement is much more strict than the limitation of optically thin cloud.

The limitation of resolution

We recall the calculation of total atom number:

$$\begin{aligned} N &= \frac{A}{\sigma_0}\sum_{i,j} OD(i,j) \\ &= \frac{A}{\sigma_0}\sum_{i,j}\left[-lnT(i,j) - \frac{I_0(i,j)}{I_{sat}}\left(T(i,j) - 1\right)\right], \end{aligned} \tag{3.37}$$

where $T(i,j) = \frac{I'(i,j)}{I_0(i,j)}$ is transmission of pixel (i,j). However we can find that $\sum_{i,j} ln\left(T(i,j)\right) \neq ln\left(\sum_{i,j} T(i,j)\right)$. Thus the variation of column density should be kept small within each picel. And the size of the atom cloud should be much larger than the pixel size. If the sample size is already very

small, any binning operation of the pixel size will cause the counting error of atom number.

However, the image resolution also limit the smallest area for the counting of optical density. The image system we used in the experiment is shown in Fig. 3.27, we use a $d = 25$ mm diameter objective lens (Edmund #49-360-INK) with a numerical aperture $NA \approx d/2f = 0.125$. The diffraction-limited resolution is $D = 0.61\lambda/NA = 3.8$ μm for ^{87}Rb and 2.9 μm for ^{23}Na. In comparison the effective pixel size is $l = \sqrt{A_{pixel}/m^2} = 2.15$ μm, which is smaller than the image resolution. However it should be notice that the resolution corresponds to the airy disc of the image system's point spread function, which is around 2.7 times larger than the σ of equivalent Gaussian function.

The smallest sample that we need to take the picture is the the Rb thermal atoms in 947 nm pancake shaped trap, which has a $1/e$ diameter of around 18 μm on vertical direction. As shown in Fig. 3.29, We use the numerical simulation to evaluate the effect of limited resolution. The simulation shows the counting error should be smaller than 10% for the resolution better than 30 νm. Thus the image resolution do not have significant effect for the number counting.

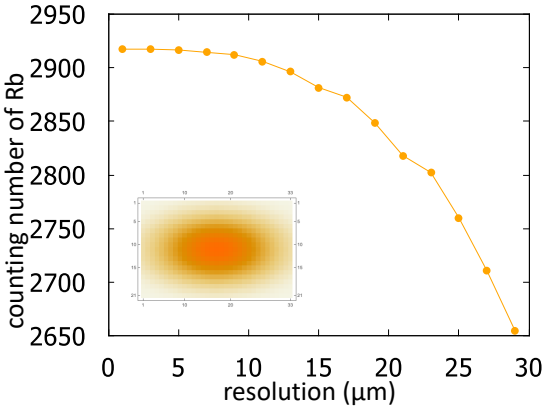

Fig. 3.29. The numerical evaluation of the ^{87}Rb's counting number in 947 nm pancake shaped trap as a function image resolution. We can find that the counting error is smaller than 10% for the resolution better than 30 μm.

The lensing effect

The interaction between atoms and light can be included by the polarizability of atoms. When the light frequency is different from the resonance frequency of atom, there will be a out-of-phase component of the dipole oscillation, which comes from the imaginary part of the polarizability. And the out of phase components will cause the variation of the phase speed of light over space, which change the index of refraction [140, 141].

For blue-detuning light, the index is smaller than 1 and the trapped atom cloud behaves as a concave lens since the canter has higher optical depth. And the atoms behave as a convex lens for red-detuning light.

However, there will be no lensing effect if the light is on resonance since the index of atom is equal to 1. Since the lensing effect will affect the image resolution and the counting of atom number, we always use resonant probe beam to image the small sample with large OD.

The heating effect

Different from an ideal two-level system with infinite lifetime for the excited state, the wavefunction overlap and energy difference between the ground state and excited state here is enough to trigger a significant spontaneous emission, which is not shown in the population oscillation of rf pulse.

The introduce of spontaneous emission not only bring us the power broadening effect but also heat the atoms. The recoil momentum from the photon accelerate the atom after each spontaneous emission. And the scatter-

ing rate of the photon is decided by the spontaneous emission rate times fraction population of the atoms in excited state

$$\begin{aligned} R_{scatt} &= \Gamma \frac{n_e}{n} \\ &= \frac{\Gamma}{2} \frac{1}{1 + \frac{I_{sat}(\omega)}{I}} \\ &= \frac{\Gamma}{2} \frac{1}{1 + \frac{\Gamma^2}{2\Omega^2} \frac{\delta^2 + \Gamma^2/4}{\Gamma^2/4}} \\ &= \frac{\Gamma}{2} \frac{\Omega^2/2}{\delta^2 + \Omega^2/2 + \Gamma^2/4}, \end{aligned} \tag{3.38}$$

where $\delta = \omega - \omega_0$ is the detuning of the probe light and we use the relation $I/I_{sat}(\omega_0) = 2\Omega^2/\Gamma^2$ with Ω defined as the Rabi frequency of the light. After knowing the scattering rate, we can calculate the speed of atoms doing the random walk and the effect of the movements can be divided into two parts.

The first part is the movements in probe beam direction. The movements of this direction will introduce the doppler shift, which is proportional to the moving speed of atoms. If we use resonance probe beam, the absorption cross section is given by

$$\sigma(v) = \sigma_0 \frac{1}{1 + \left(\frac{kv}{\Gamma/2}\right)^2}, \tag{3.39}$$

where v is the velocity of atoms along the probe beam direction. Through the atoms are doing the random walk in momentum space, the dominant term comes from the atoms being pushed by the momentum of photons in this direction. Thus the speed of atom in probe beam direction at time t_0 is.

$$\begin{aligned} v_{probe}(t_0) &= \int_0^{t_0} v_{rec} R_{scatt} \mathrm{d}t \\ &= v_{rec} R_{scatt} t_0, \end{aligned} \tag{3.40}$$

where v_{rec} is the recoil velocity of the atom. For example, if we use a probe intensity with $I = 0.5I_{sat}$ for ^{87}Rb atoms, the velocity of the atom at 100 μs should be

$$v_{probe}(100\mu s) = 5.88mm/s \times \frac{2\pi \times 6.07MHz}{6} \times 100\mu s \approx 1.9m/s. \quad (3.41)$$

And the the absorption cross section will be decreased from 1 to $0.29\sigma_0$ at 100 μs. To decrease the effect from the doppler shift, we usually use a probe intensity around $0.25I_{sat}$ with a probe time around 50 μs. However, the real absorption cross section should be $\sigma_{eff} = \frac{1}{\alpha}\sigma_0$, which is smaller than the theoretical value. For the calibration of atom number, we need to know the real number of α. This calibration can be easily done by measuring the I_{sat} since $I_{sat}^{meas} \equiv \frac{\Gamma\hbar\omega}{2\sigma_{eff}}$ and $I_{sat}^{meas}/I_{sat} = \alpha$. We will talk more about this in the section of number calibration. And the displacement of the atoms in probe beam direction is

$$z(t) = \int_0^{t_0} v_{probe}(t)\mathrm{d}t = \frac{1}{2}v_{rec}R_{scatt}t_0^2, \quad (3.42)$$

which is around 180 μm for $0.5I_{sat}$ and 100 μs probe time. Thus the field of view of image system is important for a long probe time.

The second part is the movements perpendicular to the probe beam direction, which is exactly the plane of image. The movement of the atoms can be described by the random walk following the spontaneous emission, the root mean squared velocity of the atoms at time t are given by

$$\bar{v}(t) = v_{rec}\sqrt{R_{scatt}t}, \quad (3.43)$$

Thus the displacement of the atoms should be $\int \bar{v}(t)\mathrm{d}t = \frac{2}{3}v_{rec}\sqrt{R_{scatt}}t^{3/2}$. For $I = 0.25I_{sat}$, this displacement is 2.7 μm at 100μs, which is still comparable with the image resolution. However, this limitation is only important for in situ image since the vertical image blur from 10 ms TOF is already 9.8 μm for 100 μs probe time.

3.7.3 The noise of absorption image

The noise of absorption image includes the shot noise and technical noise. And the technical noise includes the readout noise of CCD and the fringe pattern comes from the interference of multiple optical surface in the optical path.

The fringe paten comes from the optical system and it can be reproduced by taking the images without the existence of atoms. In the polaron experiment, we use a software to recognized the known interference from 40 to 100 images with no atoms and use them as orthonormal basis to remove the patterns.

Different from fluorescence image, a large amount of the photons are directly detected by CCD chip, which is much larger than the readout noise of the ADC. However, the shot noise of the photon will be significant since the noise of photon number should be

$$\sigma_{N_p} = \sqrt{N_p}, \tag{3.44}$$

where N_p is the number of photon. Since the CCD chip and ADC linearly convert the photon number into the counting of electron number, the noise of the counting number in CCD should follow the same rule

$$\sigma_{N_e} = \sqrt{N_e} = \sqrt{qN_p} = \sqrt{\frac{qA\tau}{\hbar\omega}I}, \tag{3.45}$$

where N_e is the counting number of electrons, q is the quantum efficiency of the CCD, τ is the probe time and I is the intensity of the light. Knowing the noise contribution from the shot noise, we can calculate the effective detection noise of atom number by equation 3.26. The atom number detection noise of a single pixel is

$$\begin{aligned}\sigma_{N_a} &= \sqrt{\left(\frac{\partial N_a}{\partial N_e^0}\right)^2 \sigma_{N_e^0}^2 + \left(\frac{\partial N_a}{\partial N_e'}\right)^2 \sigma_{N_e'}^2} \\ &= \sqrt{\frac{A}{\sigma_0 \frac{\Gamma}{2} q\tau}\left[4 + \frac{I_{sat}}{I_0}\left(1+\frac{I_0}{I'}\right) + \frac{I_0}{I_{sat}}\left(1+\frac{I'}{I_0}\right)\right]^{\frac{1}{2}}},\end{aligned} \tag{3.46}$$

where I' is the intensity of probe beam on single pixel after passing through the atom cloud and I_0 is directly the intensity of probe beam for reference. Since the optical depth is calculated by atom image and reference image, the shot noise of both two picture have contributions to the final atom number. It should be noted that this equation is only applied for the resonant probe beam, where $I_{sat} = \frac{\Gamma\hbar\omega}{2\sigma_0}$. The normalized shot noise given by equation 3.46 is shown in Fig. 3.20(a).

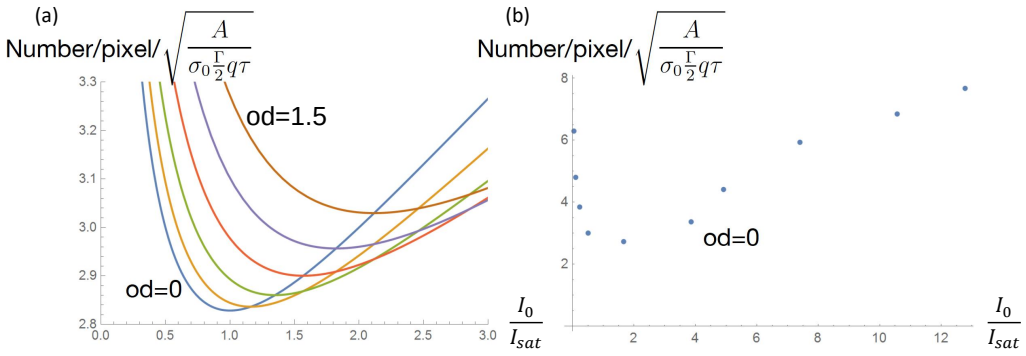

Fig. 3.30. The normalized shot noise of absorption image. (a) The theoretical curves of the shot noise as a function of probe beam intensity with the optical density varies from 0 to 1.5, the noise per pixel is normalized by the factor $\sqrt{\frac{A}{\sigma_0\frac{\Gamma}{2}q\tau}}$. (b) The normalized noise of ^{87}Rb's absorption image data under different probe beam intensity. The probe time τ is given by the experimental value with the quantum efficiency q and pixel's effective area A given by the parameters of the camera (PCO pco.pixelfly usb).

In comparison, we also measured the shot noise given by each pixel of the final absorption image. For simplification, we only measure the case for $od = 0$, which is the absorption image without the atoms. Due to the limited dynamic range of camera (16000 counts/pixel maximum), we have to vary the probe time τ of the image and this term is included in the normalization factor $\sqrt{\frac{A}{\sigma_0\frac{\Gamma}{2}q\tau}}$. The noise given by experimental data is shown in Fig. 3.20(b). Thus we can find that the noise of our absorption image is mostly limited by the shot noise of probe beam. We can also prove this by simple calculation. For example, if we use $I_0 = 0.1I_{sat}$ for probe beam intensity, the shot noise of I_0 is $\sqrt{\frac{qA\tau}{\hbar\omega}0.1I_{sat}} = 18.4$ counts/pixel, which is still much larger than the readout noise of camera ($\sigma_{pco} = 5 \sim 7$ counts/pixel).

Through the noise seems to be smallest for $I_0 \approx I_{sat}$, the noise of atom number also dependes on the absorption cross section σ, which is decided by the probe beam intensity and probe time. We have already discussed the heating effect of the probe beam. However, the effect is too complicated and it is not included in the equation 3.46.

From the normalized factor in equation 3.46 we can find that the quantum efficiency of the camera is the most important parameter for the absorption image. The other terms like effective area A and probe time τ are trivial since they are connected to the total photon number of single pixel during each measurement. If we want to further decrease the noise, we can take multiple image of I_0 and the noise $\sigma^2_{N_e^0}$ can be decrease by factor $\sqrt{m}$ with m defined as the number of repetitions. However, this method is limited by the interference patterns in our image system.

For the polaron experiment, the signal of ^{87}Rb$|1,1\rangle$ state atom number is usually very small, thus the shot noise of the absorption image has strong effect on the final signal to noise ratio. Since the signal noise ratio can be written as

$$\begin{aligned} S/N &= \frac{\sum_{i=1}^{N_{pixel}} S_i}{\sqrt{\sum_{i=1}^{N_{pixel}} \sigma^2_{N_a^i}}} \\ &= \frac{\sum_{i=1}^{N_{signal}} S_i}{\sqrt{\sum_{i=1}^{N_{pixel}} \sigma^2_{N_a^i}}}, \end{aligned} \tag{3.47}$$

where N_{pixel} is the total pixel number of the image within the counting area and N_{signal} is the number of pixel that contains the signal, which is the pixel with od larger than zero. We can find that the selection of pixel counting area for the atom number is very important since the signal to noise ratio will be poor if N_{pixel} is significantly larger than N_{signal}.

The Fig. 3.31 shows one group of raw data for polaron spectroscopy with different selection of counting area. We can find the signal to noise ratio is improved a lot with a suitable selection of pixel counting area. The area can also be selected by some algorithms, which are widely used for the noise reduction [142].

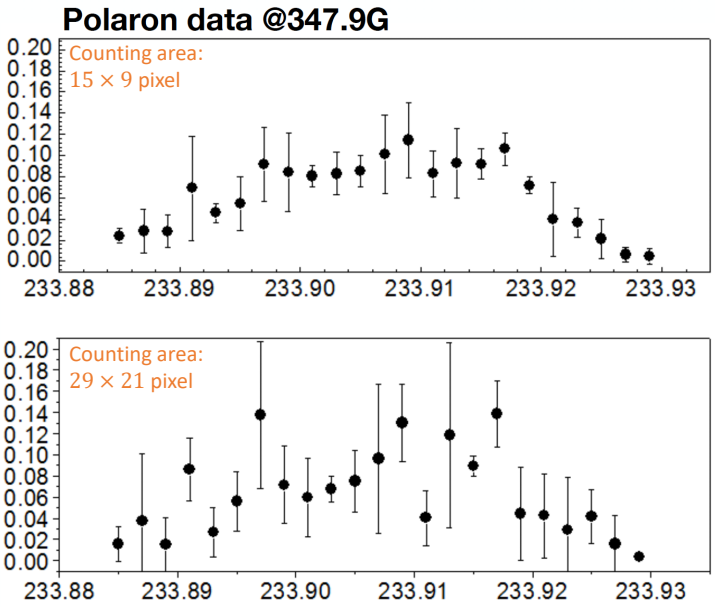

Fig. 3.31. The raw data of polaron spectroscopy at 347.9G (from Nov 2018) with different selection of pixel counting area. We can find that the signal to noise ratio becomes very poor if we count too many pixels with no contribution to the signal.

3.7.4 The energy structure and number calibration

As we have discussed in previous section, the atoms are heated by the probe beam within the probe duration and this will effectively decrease the absorption cross section of the atoms. Except the heating, the impurity of the probe beam frequency and polarization will also affect the cross section. In previous theory part, we use a two-level system to calculate the cross section and corresponding rate equation. However, this scheme is a little bit different for the real case.

The low field and high field scheme with multilevel structure

To evaluate the influence of the probe beam polarization, it is important to know the specific transitions and states in the scheme of our absorption image. And the scheme can be divided to the low magnetic field scheme and high field scheme.

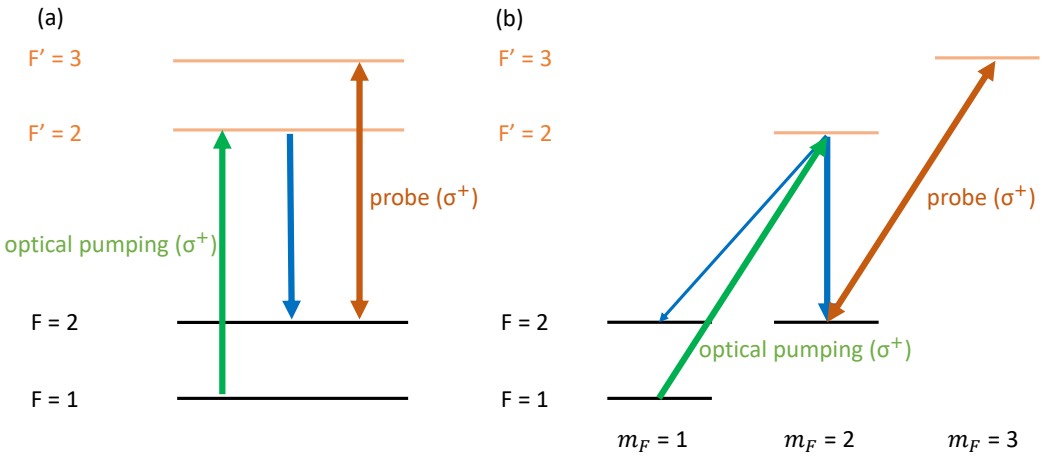

Fig. 3.32. The energy levels scheme for low and high magnetic field image. (a) The scheme for low field image, which includes the optical pumping (green arrow), spontaneous decay (blue arrow) and cycling transition for probe (brown arrow). Here, we neglect Zeeman splittings for different m_F since they are much smaller than the transition linewidth. (b) The scheme for high field image, which also includes the optical pumping and probe transition with additional Zeeman splitting. We neglect all the irrelevant energy levels with large detuning.

As shown in Fig. 3.32 (a), for the low magnetic field image, we use optical pumping light to transfer the atoms from $F = 1$ to $F = 2$ state. And then we use the probe light to drive the cycling transition between $F = 2$ ground state and $F' = 3$ excited state. Instead of a two-level system, there are five Zeeman levels in ground state and seven Zeeman levels in excited state and the transition dipole varies for different transition. However, since the magnetic field is low (around 1 G) and the Zeeman splitting is relatively small compared with the linewidth of the atom, we can use circularly polarized $\sigma_+(\sigma_-)$ light propagates in parallel with the magnetic field to exclusively drive the $|2,2\rangle \Leftrightarrow |3,3\rangle$ ($|2,-2\rangle \Leftrightarrow |2,2\rangle$) transition. This cycling transition gives the maximum cross section $\sigma_0 = \frac{3\lambda^2}{2\pi}$, where λ is the wavelength of the resonant probe light. Thus the impurity of the probe beam frequency or polarization will decrease the absorption cross section. And if we use a linearly polarized light instead of circularly polarized light, ideally, the cross section should be divided by half.

As shown in Fig. 3.32 (b), the Zeeman levels are not degenerate for high magnetic field image, we selectively detect the ^{87}Rb atoms in $|1,1\rangle$ state. And we can either use the microwave or optical pumping light to transfer

the atom from $|1,1\rangle$ to $|2,2\rangle$ ground state. For the optical pumping method, we use resonant optical pumping light to transfer the $|1,1\rangle$ ground state to the $|2,2\rangle$ excited state and around 99% atoms will go back to the $|2,2\rangle$ ground state, which can be calculated by the spontaneous emission rate. Then we use the resonant probe beam of $|2,2\rangle \Leftrightarrow |3,3\rangle$ transition under high field to probe the $|2,2\rangle$ state ^{87}Rb atoms. Different from low field image, we use linearly polarized light that propagates perpendicular to the magnetic field. Since the polarization of the light is perpendicular to the magnetic field, the cross section should be similar to the case of low field image with linearly polarized light.

Through we can still use two-level structure to calculate the ideal absorption cross section of the atoms, we still need some time to build up the cycling transition between ground state and excited state. By considering the rate equation given by 3.22, we need at least several Γ to reach the steady state. The smallest probe time is 1 μs in our experiment, which is enough for both ^{87}Rb and ^{23}Na atoms.

The number calibration

For the spinor experiment, we use the low field scheme of ^{87}Rb and ^{23}Na with circularly polarized light. And for the polaron experiment, we use high field scheme for the ^{87}Rb atoms in $|1,1\rangle$ state and low field scheme for atoms of ^{87}Rb atoms in $|1,0\rangle$ and ^{23}Na atoms in $|1,1\rangle$ state with linearly polarized light. Thus we need five different number calibrations.

We can use the saturation effect of the two-level system to evaluate the saturation intensity of the system for steady state [143]:

$$\alpha I_{sat} = \frac{\Gamma\hbar\omega}{2(\sigma_0/\alpha)} = \frac{\hbar\omega^3\Gamma\alpha}{12\pi c^2}, \tag{3.48}$$

where c is the speed of light. We rewrite the equation 3.26 by optical density and replace I_{sat} by αI_{sat}:

$$OD(x,y) = od(x,y) + \frac{I_0(x,y)}{\alpha I_{sat}}\left(1 - e^{-od(x,y)}\right). \tag{3.49}$$

From the saturation effect in equation 3.25, we can find that the optical density will be changed if we probe the atom with different probe intensity I_0. However, since the atom number is conserved for each measurement, the optical depth will still keep the same even if we tune the probe intensity. Therefore, we can determine the value of α by calculate the optical depth from the given optical density under different I_0. And we select the α that provides the optical depth with smallest standard deviation.

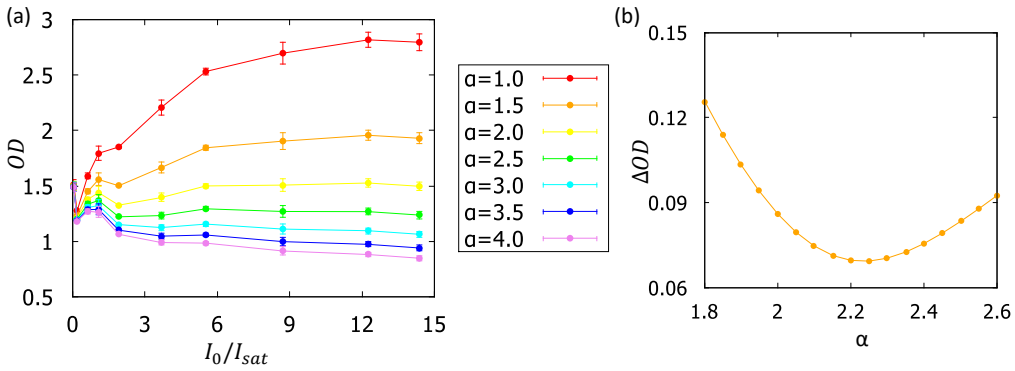

Fig. 3.33. The low field number calibration of ^{23}Na atoms with linear polarized probe beam. (a) The calculated optical depth as the function of probe intensity. The different curves are calcualted with different setting of α. (b) The standard deviation of the curves in (a) with smaller steps of α, the smallest point indecates the closest value of α.

species	condition	polarization	α
^{87}Rb	low field	σ_+	1.67
		linear	4.06
	high field	linear	2.96
^{23}Na	low field	σ_+	1.1
		linear	2.25

Tab. 3.3. The image calibration parameter α for different conditions.

One example of this kind of number calibration is shown in Fig. 3.33. In this experiment, we calibrate the low field scheme of ^{23}Na with linearly polarized light. We tune the probe intensity from 0.04 to 14 I_{sat} and the optical density are given by the gaussian fitting of the atom cloud. The probe time is adjusted for different probe intensity and the total photon number is controlled to avoid significant heating of atom cloud. As shown in Fig. 3.33(a), we select different α and calculate the corresponding optical depth with different probe intensity. We can find that the smallest

fluctuation indicates a value around two. In order to better clarify the selection of α, we calculate the standard deviation of each curve, which is shown in Fig. 3.33(b). We find the α is around 2.25 for this case.

Using the same method we measure the α for all the other cases, the results are show in Tab. 3.3. Compare with the number calibration of ^{23}Na, the ^{87}Rb shows a larger α. One possible reason is that we use the current modulation for the frequency lock of ^{87}Rb's saturated absorption spectroscopy, which will introduce the sidebands of the probe light.

4

Manipulation of heteronuclear spin dynamics with microwave and vector light shift

The spin degree freedom in ultracold atom gases has been recognized as a great asset for rich physics since 1998 [44, 45, 144]. And the observation of coherent spin population oscillations [49–52, 54, 57, 58] indicate the collisional coherence can be extended to the internal spin degrees of freedom [145, 146]. In this chapter, we will talk about the manipulation of heteronuclear spin dynamics in a spin-1 Bose-Bose mixture of ultracold ^{87}Rb and ^{23}Na atoms. The dynamics is driven by the interspecies spin-dependent interaction and quadratic Zeeman shifts.

The spinor physics for single species is extensively discussed in [46, 147]. In section 4.1, I will give a brief introduction to the theory of spin-1 spinor gases from homonuclear to the heteronuclear Bose-Bose mixture, including the Hamiltonian, the two-body theory, the mean-field treatment and the single-mode approximation. In section 4.2, I will describe our work related to the manipulation of previously study of the coherent heteronuclear spin dynamics. Similar to the well-studied homonuclear cases, the interspecies spin dynamics can be controlled by tuning the quadratic Zeeman shift with magnetic field or far-detuned microwave fields [53, 56, 65, 148–150]. In addition, we successfully realize spin dynamics control with vector light shifts which act as a species-selective effective magnetic field on ^{87}Rb atoms. Both methods show negligible loss of atoms thus will

be powerful techniques for investigating spin dynamics with fast temporal and high spatial resolutions.

4.1 The introduction to the spinor gases

4.1.1 The single-particle Hamitonian

The single particle hamitonian describe the energy of the single atom that can be written as the field operator $\psi_m(r)$, where $m \equiv m_F = -1, 0, 1$ denotes the magnetic quantum number for $F = 1$. The field operator satisfy the canonical commutation relations

$$\begin{aligned} \left[\psi_m(r), \psi^\dagger_{m'}(r')\right] &= \delta_{mm'}\delta(r - r'), \\ \left[\psi^\dagger_m(r), \psi^\dagger_{m'}(r')\right] &= [\psi_m(r), \psi_{m'}(r')] = 0, \end{aligned} \tag{4.1}$$

where $\delta_{mm'}$ is the Kronecker delta, which takes value 1 if $m = m'$ and 0 for other cases. Similar to the terms in 2.7 and 3.12, the non-interacting single-particle Hamitonian includes the kinetic energy, trapping potential and Zeeman energy terms and the second quantization form is

$$H = \int \mathrm{d}r \sum_{m=-1}^{1} \psi^\dagger_m(r) \left(-\frac{\hbar^2\nabla^2}{2M} + V_{trap}(r) - pm + qm^2 \right) \psi_m(r), \tag{4.2}$$

where $V_{trap}(r)$ is the external trapping potential, M is the mass of atom, p and q are the linear and quadratic Zeeman energy. For linear polarized optical dipole trap, $V_{trap}(r)$ is same for the atoms with different m.

4.1.2 The interaction Hamitonian

As we have already discussed in first chapter, the two-body scattering interaction is usually enough for a dilute ultra-cold atom gases and only the s-wave interaction is dominant for the low energy cases. Similar to the

contact interaction in 2.7, The contact interaction between the atoms with different m can be written as

$$V_{int} = \delta(r - r') \sum_{m_1 m_2 m_1' m_2'} g_{m_1 m_2 m_1' m_2'}, \tag{4.3}$$

where m_i and m_i' $(i = 1, 2)$ are the magnetic quantum number for the two atoms before and after the collision. The magnetization is conserved for the coherent binary collision, where $m_1 + m_2 = m_1' + m_2'$. More generally, the total spin $\mathcal{F}$ is conserved in this two-body collision. And the contact interaction can be simplified under the representation of total spin $\mathcal{F}$:

$$V_{int} = \delta(r - r') \sum_{\mathcal{F}} g_{\mathcal{F}} P_{\mathcal{F}}, \tag{4.4}$$

where $g_{\mathcal{F}} = \frac{4\pi a_{\mathcal{F}} \hbar^2}{M}$ is the coupling constant of the collision channel with total spin $\mathcal{F}$, $P_{\mathcal{F}} = \sum_{m_{\mathcal{F}}=-F}^{F} |\mathcal{F}, m_{\mathcal{F}}\rangle \langle \mathcal{F}, m_{\mathcal{F}}|$ is the projection operator for the representation of total spin $\mathcal{F}$ state and $m_{\mathcal{F}} = m_1 + m_2$ is the total magnetization of two colliding atoms. Only even F is allowed for interaction between two identical bosons. However, the odd value is also allowed for the heteronuclear interaction. The second quantization form of interacting Hamitonian is

$$\begin{aligned} H &= \frac{1}{2} \int\int \mathrm{d}r \mathrm{d}r' \sum_{m_1 m_2 m_1' m_2'} \psi_{m_1'}^{\dagger}(r) \psi_{m_2'}^{\dagger}(r') \langle m_1', m_2' | V_{int} | m_1, m_2 \rangle \psi_{m_2}(r') \psi_{m_1}(r) \\ &= \frac{1}{2} \int\int \mathrm{d}r \mathrm{d}r' \delta(r - r') \sum_{\mathcal{F}} g_{\mathcal{F}} A_{\mathcal{F} m_{\mathcal{F}}}^{\dagger}(r, r') A_{\mathcal{F} m_{\mathcal{F}}}(r, r'), \end{aligned} \tag{4.5}$$

where $A_{\mathcal{F} m_{\mathcal{F}}}(r, r') = \sum_{m_1, m_2=-F}^{F} \langle \mathcal{F}, m_{\mathcal{F}} | m_1, m_2 \rangle \psi_{m_2}(r') \psi_{m_1}(r)$ is defined as the irreducible operator. And we can find that the irreducible operator is related to the decoupled field operators of two atoms via the Clebsch-Gordan coefficients $\langle \mathcal{F}, m_{\mathcal{F}} | m_1, m_2 \rangle \equiv \langle \mathcal{F}, m_{\mathcal{F}} | F_1, m_1, F_2, m_2 \rangle$, where $F_1 = F_2 = 1$ is the spin of individual spin-1 atoms.

The homonuclear interaction for spin-1

For the homonuclear interaction with spin-1 atoms, the total spin $\mathcal{F}$ can only be 0 and 2. Thus we have the completeness relation:

$$P_0 + P_2 = \hat{1}, \tag{4.6}$$

where $\hat{1}$ is the unit operator. From the composition law of the angular momentum, we have the relation:

$$\begin{aligned}
\hat{F}_1 \cdot \hat{F}_2 &= \frac{1}{2}\left[\left(\hat{F}_1 + \hat{F}_2\right)^2 - \hat{F}_1{}^2 - \hat{F}_2{}^2\right] \\
&= \frac{1}{2}\left[\hat{\mathcal{F}}^2 - \hat{F}_1{}^2 - \hat{F}_2{}^2\right] \\
&= \frac{1}{2}\left[\mathcal{F}(\mathcal{F}+1) - F_1(F_1+1) - F_2(F_2+1)\right](P_0 + P_2) \\
&= -2P_0 + P_2,
\end{aligned} \tag{4.7}$$

where $\hat{F}_1$ and $\hat{F}_2$ are the individual spin operators of two colliding particle. Applying equation 4.6 and 4.7, we obtain

$$\begin{aligned}
\sum_{\mathcal{F}} g_{\mathcal{F}} P_{\mathcal{F}} &= g_0 \frac{\hat{1} - \hat{F}_1 \cdot \hat{F}_2}{3} + g_2 \frac{2\hat{1} + \hat{F}_1 \cdot \hat{F}_2}{3} \\
&= \frac{g_0 + 2g_2}{3}\hat{1} + \frac{g_2 - g_0}{3}\hat{F}_1 \cdot \hat{F}_2 \\
&= c_0\hat{1} + c_2\hat{F}_1 \cdot \hat{F}_2,
\end{aligned} \tag{4.8}$$

where $c_0 = \frac{g_0+2g_2}{3}$ and $c_2 = \frac{g_2-g_0}{3}$. Thus the second quantization form of the interacting Hamiltonian with the individual spin operators is

$$H = \frac{1}{2}\int \mathrm{d}r \sum_{m_1 m_2 m_1' m_2'} \left(c_0 \delta_{m_1 m_1'} \delta_{m_2 m_2'} + c_2 \hat{F}_{m_1 m_1'} \cdot \hat{F}_{m_2 m_2'}\right) \psi^\dagger_{m_1'}(r)\psi^\dagger_{m_2'}(r)\psi_{m_2}(r)\psi_{m_1}(r), \tag{4.9}$$

where $\hat{F}_{m_1 m_1'}$ ($\hat{F}_{m_2 m_2'}$) is the elements of spin-1 operators with $\hat{F} = (F_x, F_y, F_z)^T$, whose elements are defined by equation 3.13.

The heteronuclear interaction for spin-1

For the heteronuclear interaction with two spin-1 atoms, the total spin $\mathcal{F}$ ranges from $F_1 - F_2$ to $F_1 + F_2$. Thus we have the similar completeness relation:

$$P_0 + P_1 + P_2 = \hat{1}, \tag{4.10}$$

From the composition law of the angular momentum, we have the relation:

$$\begin{aligned} \hat{F}_1 \cdot \hat{F}_2 &= \frac{1}{2}\left[\mathcal{F}(\mathcal{F}+1) - F_1(F_1+1) - F_2(F_2+1)\right](P_0 + P_1 + P_2) \\ &= -2P_0 - P_1 + P_2, \end{aligned} \tag{4.11}$$

Similarly, we obtain

$$\begin{aligned} \sum_{\mathcal{F}} g_{\mathcal{F}} P_{\mathcal{F}} &= g_0 P_0 + g_1 \frac{\hat{1} - \hat{F}_1 \cdot \hat{F}_2 - 3P_0}{2} + g_2 \frac{\hat{1} + \hat{F}_1 \cdot \hat{F}_2 + P_0}{2} \\ &= \frac{g_1 + g_2}{2}\hat{1} + \frac{g_2 - g_1}{2}\hat{F}_1 \cdot \hat{F}_2 + \frac{2g_0 - 3g_1 + g_2}{2}P_0 \\ &= \alpha\hat{1} + \beta\hat{F}_1 \cdot \hat{F}_2 + \gamma P_0, \end{aligned} \tag{4.12}$$

where $\alpha = \frac{g_1+g_2}{2}$, $\beta = \frac{g_2-g_1}{2}$ and $\gamma = \frac{2g_0-3g_1+g_2}{2}$. And the second quantization form of the interacting Hamiltonian with the individual spin operators is

$$\begin{aligned} H = \frac{1}{2}\int \mathrm{d}r \sum_{m_1 m_2 m_1' m_2'} &\left(\alpha\delta_{m_1 m_1'}\delta_{m_2 m_2'} + \beta\hat{F}_{m_1 m_1'} \cdot \hat{F}_{m_2 m_2'}\right)\psi^\dagger_{m_1'}(r)\psi^\dagger_{m_2'}(r)\psi_{m_2}(r)\psi_{m_1}(r) \\ &+ \gamma\psi_0^\dagger(r)\psi_0^\dagger(r)\psi_0(r)\psi_0(r). \end{aligned} \tag{4.13}$$

4.1.3 The mean-field treatment and single-mode approximation

We have introduced the single-particle Hamiltonian and the interaction Hamiltonian for the spinor physics. However, the Hamiltonian is still too

difficult analyse the behaviour of the system. And two different approximations are made to simplify the problem.

Firstly, we apply the mean-field theory. We can replace the field operator with its expectation value $\langle\psi_m(r)\rangle$ and we neglect the fluctuations, which means we redefine the field operator as

$$\hat{\psi}_m(r) = \left\langle \hat{\psi}_m(r) \right\rangle . \tag{4.14}$$

And the expectation value can be the averaging value in a homogeneous system, a BEC or a thermal gas. Since the density distribution of atoms are not homogeneous in an optical dipole trap, it is still difficult to use $\langle\psi_m(r)\rangle$ as field operator. The single mode approximation is usually applied for a trapped system, where we assume all the spin components share the same spactial distribution and only the spin populations vary in time. Thus the spin state and spacial distribution are decoupled for the atoms. And we can use

$$\hat{\psi}_m(r) = \sqrt{N}\xi_m(t) \left\langle \hat{\psi}_{sma}(r) \right\rangle , \tag{4.15}$$

where $\xi_m(t)$ is the space-independent spinor, N is the number of the particle and $\psi_{sma}(r)$ is spacial mode function under single mode approximation and $\psi_{sma}(r)$ is determined from the spin-independent part of the Hamiltonian:

$$\left[-\frac{\hbar^2\nabla^2}{2M} + V_{trap}(r) + \frac{1}{2}c_0 N \left|\psi_{sma}(r)\right|^2 \right] \psi_{sma}(r) = \mu\psi_{sma}(r), \tag{4.16}$$

where c_0 should be α for heteronuclear interaction. However, the approximation is not exactly correct for case that we have couplings or the size of the system is much larger than the healing length of spin interaction. And the invalid of single mode approximation have introduced a lot of new topics like spin-orbit coupling and spin texture. However, we will only talk about the basic theory here for the spinor physics.

As an example, the overall Hamiltonian of homonuclear spin-1 system is

$$\begin{aligned} H &= H_0 + H_s \\ &= N\int \mathrm{d}r \left(\frac{\left|-i\hbar\nabla\psi_{sma}(r)\right|^2}{2M} + \left|V_{trap}(r)\right| + \frac{c_0}{2}\frac{\left|\psi_{sma}(r)\right|^4}{N} \right) \\ &+ N\int \mathrm{d}r \left(-p\left|F_z\right| + q\left|F_z\right|^2 + \frac{c_2}{2}\left|\hat{F}_1\cdot\hat{F}_2\right|\frac{\left|\psi_{sma}(r)\right|^4}{N} \right) \\ &= N\int \mathrm{d}r \left(\frac{\left|-i\hbar\nabla\psi_{sma}(r)\right|^2}{2M} + \left|V_{trap}(r)\right| + \frac{c_0 n}{2} \right) \\ &+ N\int \mathrm{d}r \left(-p\left|F_z\right| + q\left|F_z\right|^2 + \frac{c_2 n}{2}\left|\hat{F}_1\cdot\hat{F}_2\right| \right), \end{aligned} \tag{4.17}$$

where N is the particle number of the system, $n = \left|\psi_{sma}(r)\right|^4/N$ is the average number density and $||$ stands for the averaging over all different combination of spinor state ξ_m.

4.1.4 The ground state of homonuclear spin-1 system

Using the single mode approximation, the Hamiltonian is divided into the spin-independent part for ψ_{sma} and spin-dependent part for ξ_m. We want

to calculate the ground state of the system, which corresponds to the minimum value of the Hamiltonian

$$
\begin{aligned}
H_s &= -p\left|F_z\right| + q\left|F_z\right|^2 + \frac{c_2 n}{2}\left|\hat{F}_1 \cdot \hat{F}_2\right| \\
&= \begin{pmatrix} -p+q & 0 & 0 \\ 0 & 0 & 0 \\ 0 & 0 & p+q \end{pmatrix} + \frac{c_2 n}{2} \begin{pmatrix} 1 & 0 & 0 & 0 & 0 & 0 & 0 & 0 & 0 \\ 0 & 0 & 0 & 1 & 0 & 0 & 0 & 0 & 0 \\ 0 & 0 & -1 & 0 & 1 & 0 & 0 & 0 & 0 \\ 0 & 1 & 0 & 0 & 0 & 0 & 0 & 0 & 0 \\ 0 & 0 & 1 & 0 & 0 & 0 & 1 & 0 & 0 \\ 0 & 0 & 0 & 0 & 0 & 0 & 0 & 1 & 0 \\ 0 & 0 & 0 & 0 & 1 & 0 & -1 & 0 & 0 \\ 0 & 0 & 0 & 0 & 0 & 1 & 0 & 0 & 0 \\ 0 & 0 & 0 & 0 & 0 & 0 & 0 & 0 & 1 \end{pmatrix} \\
&= p\left(\xi_{-1}^{\dagger}\xi_{-1} - \xi_1^{\dagger}\xi_1\right) + q\left(\xi_1^{\dagger}\xi_1 + \xi_{-1}^{\dagger}\xi_{-1}\right) \\
&+ \frac{c_2 n}{2}(\xi_1^{\dagger}\xi_1^{\dagger}\xi_1\xi_1 + \xi_{-1}^{\dagger}\xi_{-1}^{\dagger}\xi_{-1}\xi_{-1} + 2\xi_1^{\dagger}\xi_0^{\dagger}\xi_0\xi_1 + 2\xi_{-1}^{\dagger}\xi_0^{\dagger}\xi_0\xi_{-1} - 2\xi_1^{\dagger}\xi_{-1}^{\dagger}\xi_{-1}\xi_1 \\
&+ 2\xi_1^{\dagger}\xi_{-1}^{\dagger}\xi_0\xi_0 + 2\xi_0^{\dagger}\xi_0^{\dagger}\xi_1\xi_{-1}).
\end{aligned}
\tag{4.18}
$$

And we also have two containments on total atom number N and the magnetization $|F_z|$, respectively. Thus the ground state is the solution that minimize the Hamiltonian

$$
H' = H_s - p_0\left(\xi_1^{\dagger}\xi_1 - \xi_{-1}^{\dagger}\xi_{-1}\right) - \mu\left(\xi_1^{\dagger}\xi_1 + \xi_0^{\dagger}\xi_0 + \xi_{-1}^{\dagger}\xi_{-1}\right), \tag{4.19}
$$

where p_0 and μ are the Lagrange multiplier to be determined. We can choose the overall phase that let the phase of zero components be zero and $\xi_{\pm 1} = \xi_{\pm 1}^{Re} + i\delta$. The equation of motion for spinor is

$$
i\hbar\frac{\partial \xi_m}{\partial t} = \frac{\partial H'}{\partial \xi_m^*}. \tag{4.20}
$$

We replace $p + p_0$ by $\tilde{p}$ and the ground state of H' gives

$$
\begin{aligned}
\left(-\tilde{p} + q + c_2 n f_z - \mu\right)\xi_1 + c_2 n\left(\xi_1^{Re} + \xi_{-1}^{Re}\right)\xi_0^2 &= 0, \\
\left[c_2 n\left(\xi_1^{Re} + \xi_{-1}^{Re}\right)^2 - \mu\right]\xi_0 &= 0, \\
\left(\tilde{p} + q + c_2 n f_z - \mu\right)\xi_{-1} + c_2 n\left(\xi_1^{Re} + \xi_{-1}^{Re}\right)\xi_0^2 &= 0,
\end{aligned}
\tag{4.21}
$$

where $f_z = \xi_1^*\xi_1 - \xi_{-1}^*\xi_{-1}$. The solution of the euquation 4.21 and be dvided into two different cases. And they are either (i) $\xi_0 = 0$ or (ii) $\mu = c_2 n \left(\xi_1^{Re} + \xi_{-1}^{Re}\right)^2$. For the case (i) we have three ground state:

I. Longitudinal ferromagnetic state (F)

$$\begin{aligned} &(e^{i\theta_1}, 0, 0)^T, f_z = 1, \\ &E = -\tilde{p} + q + \frac{1}{2}c_2 n \end{aligned} \tag{4.22}$$

II. Longitudinal ferromagnetic state (F)

$$\begin{aligned} &(0, 0, e^{i\theta_{-1}})^T, f_z = -1, \\ &E = \tilde{p} + q + \frac{1}{2}c_2 n, \end{aligned} \tag{4.23}$$

III. Antiferromagnetic state (AF)

$$\begin{aligned} &(e^{i\theta_1}\sqrt{\frac{1}{2}\left(1 + \frac{\tilde{p}}{c_2 n}\right)}, 0, e^{i\theta_{-1}}\sqrt{\frac{1}{2}\left(1 - \frac{\tilde{p}}{c_2 n}\right)})^T, f_z = \frac{p}{c_2 n}, \\ &E = \tilde{p} + q + \frac{1}{2}c_2 n, \end{aligned} \tag{4.24}$$

where $\theta_{\pm 1}$ are the arbitrary phase.

For the case (ii), we have other two ground state:

IV. Longitudinal polar state (P)

$$\begin{aligned} &(0, e^{i\theta_0}, 0)^T, f_z = 1, \\ &E = 0, \end{aligned} \tag{4.25}$$

V. Broken-axisymmetry state (BA)

$$\begin{aligned} &(e^{i\theta_0+\theta}\frac{q+\tilde{p}}{2q}\sqrt{\frac{-\tilde{p}^2+q^2+2c_2 nq}{2c_2 nq}}, \\ &e^{\theta_0}\sqrt{\frac{q^2-\tilde{p}^2}{2q}}\sqrt{\frac{-\tilde{p}^2-q^2+2c_2 nq}{2c_2 nq}}, \\ &e^{i\theta_0-\theta}\frac{q-\tilde{p}}{2q}\sqrt{\frac{-\tilde{p}^2+q^2+2c_2 nq}{2c_2 nq}})^T, \\ &f_z = \frac{\tilde{p}(-\tilde{p}^2+q^2+2qc_2 n)}{2c_2 nq^2}, E = \frac{(-\tilde{p}^2+q^2+2qc_2 n)^2}{8c_2 nq^2}. \end{aligned} \tag{4.26}$$

We can find that the state V exists only when $c_2 < 0$ and it is the only state that total spin is tilted against the direction of magnetic field. The state is called broken-axisymmetry state because the axial symmetry with respect to the magnetic field is broken.

It should be noted that the above calculation doesn't require a fixed $\tilde{p}$. On the other hand, we choose the magnetization f_z and calculation gives the corresponding $\tilde{p}$ to minimize the energy of the system. And there is no direct connection between f_z and $\tilde{p}$. The phase diagram in the parameter space of p and q for $c_2 > 0$, $c_2 = 0$ and $c_2 < 0$ are shown in Fig. 4.1.

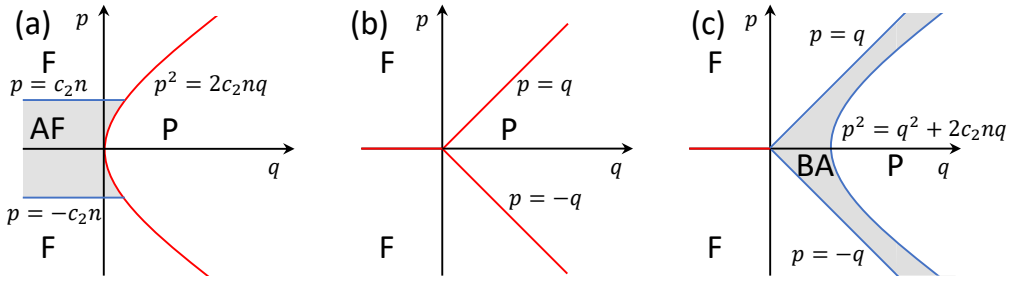

Fig. 4.1. The ground state phase diagram of spin-1 homonuclear spinor gases for (a) $c_2 > 0$ (b) $c_2 = 0$ and (c) $c_2 < 0$. The solid lines are phase boundaries. The red (blue) boundaries indicate first-order (second-order) phase transitions. The shaded area indicates the region that the rotational symmetry about the magnetic field axis is broken.

4.1.5 The two-body theory of spinor dynamics

We focus on the spin exchange process between spin-1 ^{87}Rb and spin-1 ^{23}Na and the total spin channels $\mathcal{F} = 0, 1, 2$ are all allowed [151, 152]. Previously, we have observed the coherent heteronuclear spin oscillation in a spin-1 mixture of ^{87}Rb and ^{23}Na atoms via the spin exchange process $|m_1 = 0, m_2 = -1\rangle \leftrightarrow |m_1 = -1, m_2 = 0\rangle$ [24]. Here, we denote a pair of spin-1 atoms with ^{87}Rb in $|m_1\rangle$ and ^{23}Na in $|m_2\rangle$ as $|m_1, m_2\rangle$. In the following experiment, I will mainly focus on the process

$$|0, 0\rangle \leftrightarrow |1, -1\rangle\,, \tag{4.27}$$

which is started from a pure $|0, 0\rangle$ mixture of ^{87}Rb and ^{23}Na atoms. We first only consider the heteronuclear spin-exchange interaction. Since the to-

tal magnetization M is zero, the heteronuclear spin-dependent interaction Hamitonian for a two-particle system can be expressed as

$$\begin{aligned} H_{NR} &= \sum_{\mathcal{F}} g_{\mathcal{F}}^{NR} \left|\mathcal{F}, M\right\rangle \left\langle \mathcal{F}, M\right| \\ &= g_2^{NR} \left|2,0\right\rangle \left\langle 2,0\right| + g_1^{NR} \left|1,0\right\rangle \left\langle 1,0\right| + g_0^{NR} \left|0,0\right\rangle \left\langle 0,0\right|, \end{aligned} \tag{4.28}$$

where $g_{\mathcal{F}}^{NR}$ is the coupling constant of the collision channel with total spin $\mathcal{F}$ between ^{87}Rb and ^{23}Na . And we evaluate the Clebsch-Gordan coefficient between $|m_1, m_2\rangle$ and $|F, M\rangle$, which gives

$$\begin{aligned} \left|2,0\right\rangle &= \sqrt{\frac{1}{6}} \left|1,-1\right\rangle + \sqrt{\frac{2}{3}} \left|0,0\right\rangle + \sqrt{\frac{1}{6}} \left|-1,1\right\rangle, \\ \left|1,0\right\rangle &= \sqrt{\frac{1}{2}} \left|1,-1\right\rangle - \sqrt{\frac{1}{2}} \left|-1,1\right\rangle, \\ \left|0,0\right\rangle &= \sqrt{\frac{1}{3}} \left|1,-1\right\rangle - \sqrt{\frac{1}{3}} \left|0,0\right\rangle + \sqrt{\frac{1}{3}} \left|-1,1\right\rangle. \end{aligned} \tag{4.29}$$

In the basis of $|1,-1\rangle$, $|0,0\rangle$ and $|-1,1\rangle$, H_{NR} can be expressed as

$$H_{NR} = \begin{pmatrix} \frac{1}{6}g_2^{NR} + \frac{1}{2}g_1^{NR} + \frac{1}{3}g_0^{NR} & \frac{1}{3}g_2^{NR} - \frac{1}{3}g_0^{NR} & \frac{1}{6}g_2^{NR} - \frac{1}{2}g_1^{NR} + \frac{1}{3}g_0^{NR} \\ \frac{1}{3}g_2^{NR} - \frac{1}{3}g_0^{NR} & \frac{2}{3}g_2^{NR} + \frac{1}{3}g_0^{NR} & \frac{1}{3}g_2^{NR} - \frac{1}{3}g_0^{NR} \\ \frac{1}{6}g_2^{NR} - \frac{1}{2}g_1^{NR} + \frac{1}{3}g_0^{NR} & \frac{1}{3}g_2^{NR} - \frac{1}{3}g_0^{NR} & \frac{1}{6}g_2^{NR} + \frac{1}{2}g_1^{NR} + \frac{1}{3}g_0^{NR} \end{pmatrix}. \tag{4.30}$$

We neglect all the spin-independent term of the Hamiltonian and it remains the Zeeman energy

$$H_Z = \begin{pmatrix} -p_{Rb} + p_{Na} + q_{Rb} + q_{Na} & 0 & 0 \\ 0 & 0 & 0 \\ 0 & 0 & p_{Rb} - p_{Na} + q_{Rb} + q_{Na} \end{pmatrix}, \tag{4.31}$$

where p_i and q_i ($i = Rb, Na$) are the linear and quadratic Zeeman energy of species i. An advantage of heteronuclear spin dynamics is that we can tune only one of the diagonal element in H_z to zero and select out the dynamics we interest. Here we can tune the term $-p_{Rb} + p_{Na} + q_{Rb} + q_{Na}$ to around

zero and we study the $|0,0\rangle \leftrightarrow |1,-1\rangle$ process. Thus the Hamiltonian can be simplified by a 2×2 matrix.

$$H_Z + H_{NR} = \begin{pmatrix} \frac{1}{3}\gamma + \alpha - \beta + E_{Zeeman}^{|1,-1\rangle} & \beta - \frac{1}{3}\gamma \\ \beta - \frac{1}{3}\gamma & \frac{1}{3}\gamma + \alpha \end{pmatrix}, \tag{4.32}$$

where $E_{Zeeman}^{|1,-1\rangle} = -p_{Rb} + p_{Na} + q_{Rb} + q_{Na}$.

Except the Zeeman energy and heteronuclear interaction, we also have the homonuclear spin interaction. Through the homonuclear interaction doesn't affect the spin population oscillation, it still affects the energy of the system. We can use the equation 4.17 and 4.18 to evaluate the contribution from homonuclear interaction. For ^{87}Rb atoms, the Hamiltonian of is given by

$$\begin{aligned} H_{Rb} &= \left(c_0^{Rb} + c_2^{Rb}\right) \xi_1^\dagger \xi_1^\dagger \xi_1 \xi_1 + 2\left(c_0^{Rb} + c_2^{Rb}\right) \xi_1^\dagger \xi_0^\dagger \xi_1 \xi_0 + c_0^{Rb} \xi_0^\dagger \xi_0^\dagger \xi_0 \xi_0 \\ &= \begin{pmatrix} c_0^{Rb} + c_2^{Rb} & c_0^{Rb} + c_2^{Rb} \\ c_0^{Rb} + c_2^{Rb} & c_0^{Rb} \end{pmatrix}. \end{aligned} \tag{4.33}$$

Similarly, the Hamiltonian for ^{23}Na is

$$\begin{aligned} H_{Na} &= \left(c_0^{Na} + c_2^{Na}\right) \xi_{-1}^\dagger \xi_{-1}^\dagger \xi_{-1} \xi_{-1} + 2\left(c_0^{Na} + c_2^{Na}\right) \xi_{-1}^\dagger \xi_0^\dagger \xi_{-1} \xi_0 + c_0^{Na} \xi_0^\dagger \xi_0^\dagger \xi_0 \xi_0 \\ &= \begin{pmatrix} c_0^{Na} + c_2^{Na} & c_0^{Na} + c_2^{Na} \\ c_0^{Na} + c_2^{Na} & c_0^{Na} \end{pmatrix}. \end{aligned} \tag{4.34}$$

Since the magnetic field is usually around 1 G, the homonuclear dynamics are supressed and the off-diagonal terms have no effect to the system. And the Hamtonian of the system should be

$$H = H_Z + H_{NR} + \begin{pmatrix} c_0^{Na} + c_2^{Na} + c_0^{Rb} + c_2^{Rb} & 0 \\ 0 & c_0^{Na} + c_0^{Rb} \end{pmatrix}, \tag{4.35}$$

which is simply a two-level system. And the energy of different state is defined by Zeeman energy and spin-dependent interaction. However, the

coupling is only decided by heteronuclear interaction. And the Rabi frequency is given by

$$\Omega = \frac{1}{\hbar}\sqrt{\left(E_{Zeeman}^{|1,-1\rangle} - \beta + c_2^{Na} + c_2^{Rb}\right)^2 + (\beta - \frac{1}{3}\gamma)^2} \tag{4.36}$$

This model predict the resonant oscillation at $E_{Zeeman}^{|1,-1\rangle} = \beta - c_2^{Na} - c_2^{Rb} \approx 0$ or $B_0 = 0.99$ G with longest period and largest amplitude. And we can find this spin-exchange process is driven by the $\beta - \frac{1}{3}\gamma$ term. However, the singlet pairing term γ is usually much smaller than the spin-exchange term β and process is mainly driven by β term [151, 152]. For the ^{87}Rb and ^{23}Na system, we have verified previously that the sign of the β term is negative, i.e. ferromagnetic, which tends to align the spins of the two atoms along the same direction.

As we observed in Sec. 4.2.4, the prediction of the oscillation agrees with the result of double BEC mixture. However, the dynamics always starts after a delay. And this behaviour can be explained by the fact that the $|0\rangle$ state of the homonuclear spin-1 system is metastable and spin dynamics can only be initiated by quantum fluctuation which needs some time to build up. Similar physics may be also dictating the heteronuclear dynamics here, but this has not been investigated thoroughly.

However, in Sec. 4.2.5 we can find that the prediction can not be applied the mixture of BEC and thermal atoms, which is hard to be treated theoretically, especially with the possible thermal and quantum fluctuations involved. Additionally, different from the two-particle model we are talking about here, the spinor mixture is a many-body system and the exact resonance position will be affected by the β^{RN}, c_2^{Na} and c_2^{Rb} terms times the density overlap. Thus the exact resonance position also depends on the homonuclear spin-dependent interaction and possibly the number ratios.

4.2 The manipulation of the heteronuclear spin dynamics

As we have already discussed in previous section, one profound feature of heteronuclear spin dynamics compared with the homonuclear one is the additional two-body scattering channel with $\mathcal{F} = 1$. Considering the all scattering process for homonuclear spin-1 case, we can find that only one spin changing process $2\,|0\rangle \leftrightarrow |1\rangle + |-1\rangle$ is relevant. However, for the heteronuclear case, the spin changing process only require the conservation of total magnetization:

$$|m_1, m_2\rangle \leftrightarrow |m_1', m_2'\rangle\,, \tag{4.37}$$

where $m_1 \neq m_2$ and $m_1 + m_2 = m_1' + m_2'$. In this work, we focus on the process 4.27. However, starting from $|0,0\rangle$, both the process 4.27 and $|0,0\rangle \leftrightarrow |-1,1\rangle$ can satisfy the above requirement. However, the processes are driven by the competition between the β term and the total Zeeman energy difference ΔE between two side of the process. Since the energy scale of the β term is only several Hz, the heteronuclear spin oscillation can only occur near $\Delta E = 0$ point. In the ^{87}Rb and ^{23}Na system the process 4.27 indicates

$$\Delta E = E_{\text{Zeeman}}^{|0,0\rangle} - E_{\text{Zeeman}}^{|1,-1\rangle} = p_{Rb} - p_{Na} - q_{Rb} - q_{Na}, \tag{4.38}$$

which has zero crossing at around $B_0 = 0.99$ G. ΔE is shown by the solid curve in Fig 4.2(a). And $E_{Zeeman}^{|m_1,m_2\rangle}$ is the total Zeeman shift of a pair of atoms with ^{87}Rb in $|m_1\rangle$ and ^{23}Na in $|m_2\rangle$ state. Heteronuclear spin exchange following process 4.27 can thus happen near B_0. However, the other process indicates $\Delta E = p_{Na} - p_{Rb} - q_{Rb} - q_{Na}$, which keeps decreasing with B (dash-dot curve in Fig 4.2(a)). Thus the other process is strongly supressed near B_0.

After checking all the homonuclear and heteronuclear processes we can find that nearly all of them are suppressed by ΔE except the process 4.27 and $|-1,0\rangle \leftrightarrow |0,-1\rangle$. The zero-crossing of second one is located around 1.691 G and it has already been studied in our previous work. The two

processes provide the possibility to separate the irrelevant processes and simplify the dynamics.

4.2.1 The idea of tuning $\triangle E$ for heteronuclear spin dynamics

Tuning $\triangle E$ by microwave

Microwave dressing is widely used method for controlling spin oscillation dynamics in homonuclear spinor gases. At a fixed dc magnetic field B, the presence of microwave field off-resonantly connecting the $F = 1$ and $F = 2$ hyperfine levels can introduce an additional quadratic Zeeman shift. The shifts $\delta E_{\text{MW}}(m, \Delta)$ of the $F = 1$ hyperfine state for $m = 0, \pm 1$ Zeeman levels are different from one to another due to their differences in detuning and transition strengths. The sign of the microwave induced quadratic Zeeman shift can also be readily changed by controlling the detuning Δ for exploring phases not accessible with the dc magnetic field only.

When the Rabi frequency of the microwave transition is much smaller than the detuning, the ac Zeeman shift for each m can be expressed as [53, 148]

$$\delta E_{\text{MW}}(m, \Delta) = \frac{h}{4} \sum_{m'} \frac{\Omega^2_{mm'}}{\Delta - (m' g'_F - m g_F)\mu_B / h}, \tag{4.39}$$

where Δ is defined as the detuning with respect to the $|F = 1, m = 0\rangle \leftrightarrow |F = 2, m' = 0\rangle$ transition, $g_{F=1} = -0.5018$ and $g_{F=2} = 0.4998$ are the hyperfine Landé g-factors, and μ_B is the Bohr magneton. As shown in the inset of Fig. 4.2(b) are δE_{MW} for the $m = 0$ (solid black curve) and 1 (solid red curve) levels of $F = 1$ ^{87}Rb atoms at $B = 0.96$ G when Δ is tuned.

In the heteronuclear spinor system, because of the very different hyperfine splitting, the microwave field can be selectively applied to one species while leave the other species intact. For instance, the hyperfine splitting of ^{87}Rb is about 6.8 GHz, while that of ^{23}Na is only around 1.7 GHz. Thus a microwave field near resonance with the ^{87}Rb hyperfine transition will not affect the energy levels of ^{23}Na because of the large detuning. This can

still be used to control the spin dynamics in process 4.27 since δE_{MW} is different for $|F=1,m=0\rangle$ and $|F=1,m=1\rangle$ levels of ^{87}Rb.

Taking the microwave induced shifts on the ^{87}Rb energy levels into account, the total internal energy difference between the two sides of process 4.27 is now

$$\Delta E(B,\Delta) = (E_{\text{Zeeman}}^{|0,0\rangle} - E_{\text{Zeeman}}^{|1,-1\rangle}) + (\delta E_{\text{MW}}(0,\Delta) - \delta E_{\text{MW}}(1,\Delta)). \quad (4.40)$$

At a fixed B, by changing the detuning Δ of the microwave field, ΔE and thus the spin dynamics can be tuned.

As shown in Fig. 4.2(b), applying a σ^+ polarized microwave field with fixed frequency and power while varying B, the zero crossing point of ΔE will be shifted to different B field values. For this calculation, the microwave frequency is fixed at 6836.5545 MHz while B is tuned from 0 to 2 G. Due to selection rules, there are only three non-zero microwave Rabi frequencies ($\Omega_{-1,0}, \Omega_{0,1}, \Omega_{1,2}$) with ratios determined by the relative transition strengths. We note that under this configuration, there are actually several zero crossings in Fig. 4.2(b) due to the transitions of different sublevels. In principle, all of them can be used for spin dynamics control.

To calculate the microwave shift for our system, we need to know the Rabi frequency in equation 4.40, which can be easily measured by driving the resonant spin oscillation between different Zeeman levels (like what we did for the rf spectroscopy). Unfortunately, the polarization seen by the atoms is not purely σ^+, σ^- or π but the combination of them. Since there are only three free parameters for the microwave polarization, we don't have to measure nine different Rabi frequencies one by one and we can measure just three of them. And the other Rabi frequencies can be calculate by the relative strength of the transition dipoles [153]. The transition dipole is

$$\langle F,m|\,\mu_B B_{\Delta m}\,|F',m'\rangle = \langle F|\,\mu_B B\,|F'\rangle\,(-1)^{F'-1+m_F}\sqrt{2F+1}\begin{pmatrix} F' & 1 & F \\ m' & \Delta m & -m \end{pmatrix}, \quad (4.41)$$

where $-\Delta m = m' - m = 1, 0, -1$ and $\mu_B B_{\Delta m}$ corresponds to the magnetic dipole for σ_+, π and σ_-, respectively. Additionally, they are independently

connected to strength of three polarization components. The matrix in the equation describes the 3-j symbol (or Clebsch-Gordan coefficient), which vanishes when $m - m' \neq \Delta m$.

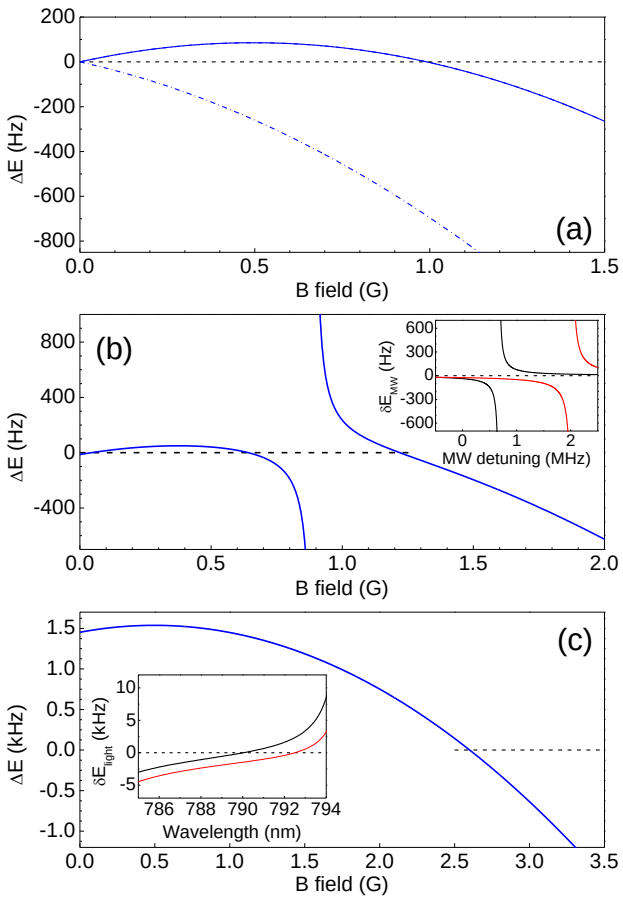

Fig. 4.2. ΔE for the relevant heteronuclear spin oscillation processes in the spin-1 ^{87}Rb and ^{23}Na mixture. (a) $\Delta E(B)$ for processes $|0,0\rangle \leftrightarrow |1,-1\rangle$ (solid curve) and $|0,0\rangle \leftrightarrow |-1,1\rangle$ (dash-dot curve). (b) $\Delta E(B,\Delta)$ with the microwave dressing field (Eq. 4.40). The microwave is σ^+ polarized with Δ = 1.872 MHz. Here, the three non-zero Rabi frequencies are $(\Omega_{-1,0},\Omega_{0,1},\Omega_{1,2}) = (10/\sqrt{3},10,10\sqrt{2})$ kHz. Inset: $\delta E_{MW}(0,\Delta)$ (solid black curve), $\delta E_{MW}(1,\Delta)$ (solid red curve) as a function of Δ at B = 0.96 G. (c) $\Delta E(B,\Delta_{D1},\Delta_{D2})$ with the vector light shift (Eq. 4.43). Here, the intensity of the σ^- polarized 790 nm laser is set at 5 W/cm^2. Inset: δE_{light} for $|0\rangle$ (solid black curve) and $|1\rangle$ (solid red curve) states of ^{87}Rb.

For each Δm, we measure one Rabi frequency and the remaining Rabi frequencies can be calculated by the transition dipole. For the microwave power used in this work, the several measured on resonance Rabi frequencies are $\Omega_{-1,-2} = 8.1$ kHz, $\Omega_{-1,-1} = 4.5$ kHz and $\Omega_{-1,0} = 3.7$ kHz. We then

calculate the other several Rabi frequencies as $\Omega_{0,-1} = 5.7$ kHz, $\Omega_{0,0} = 5.1$ kHz, $\Omega_{0,1} = 6.3$ kHz, $\Omega_{1,0} = 3.3$ kHz, $\Omega_{1,1} = 4.5$ kHz and $\Omega_{1,2} = 8.9$ kHz.

Tuning ΔE by vector light shift

In previous work, we already demonstrated controlling the resonance position of the heteronuclear spin oscillations with species and spin-dependent vector light shift [24]. In that work, the vector light shift was induced by adding various amounts of circular polarization components to the optical trap laser with a quarter waveplate. Here we introduce an additional single frequency laser to induce the vector light shift more flexibly. For alkali atoms, when the laser detuning is much larger than the excited state hyperfine splitting, the light shift can be generally expressed as

$$\delta E_{\text{light}}(m, \Delta_{D1}, \Delta_{D2}) = \frac{\pi c^2 \Gamma}{2\omega_0^3}\left[\left(\frac{2}{\Delta_{D2}} + \frac{1}{\Delta_{D1}}\right) + \wp\left(\frac{g_F m}{\Delta_{D2}} - \frac{g_F m}{\Delta_{D1}}\right)\right] I(\vec{r}). \tag{4.42}$$

Here Γ is the linewidth of the $D-$lines, ω_0 is the transition frequency, Δ_{D1} (Δ_{D2}) is the detuning of the laser with respect to the D_1 (D_2) line, and $\wp = 0$ and ± 1 for linear and circular $\sigma^{\pm}$ polarized light. In the above equation, the first term comes from the spin-independent scalar ac polarizability. If the laser frequency is tuned to in between the excited-state fine structures, this part of the light shift could become zero as the signs of Δ_{D1} and Δ_{D1} are opposite. For ^{87}Rb, the corresponding wavelength for zero scalar light shift is 790.0 nm. The second, spin-dependent term, which is only non-zero when circular polarized light is used ($\wp \neq 0$), is from the vector polarizability. The inset of Fig. 4.2(c) shows δE_{light} vs. the dressing laser wavelength for $|0\rangle$ (solid black curve) and $|1\rangle$ (solid red curve) Zeeman levels of ^{87}Rb under low magnetic field. The light polarization is σ^- ($\wp = -1$).

In the heteronuclear ^{87}Rb and ^{23}Na spinor system, since the D-line transition frequencies are very different for the two species and δE_{light} is inversely proportional to the detuning, the light shift can also be made essentially species-selective. In the experiment, we use a laser operating at

around 790 nm which affects mainly the energy levels of ^{87}Rb with negligible effect on ^{23}Na. Taking δE_{light} on ^{87}Rb into account, the total internal energy difference between the two sides of process 4.27 can be expressed as

$$\begin{aligned}\Delta E(B, \Delta_{D1}, \Delta_{D2}) = (E_{\text{Zeeman}}^{|0,0\rangle} - E_{\text{Zeeman}}^{|1,-1\rangle}) \\ +[\delta E_{\text{light}}(0, \Delta_{D1}, \Delta_{D2}) - \delta E_{\text{light}}(1, \Delta_{D1}, \Delta_{D2})].\end{aligned} \tag{4.43}$$

It can be seen that only the spin-dependent vector light shift has influence on the spin dynamics. We note that the use of near 790 nm light also minimizes possible perturbation to the optical trap potential which otherwise will modify the sample density distribution. As shown in Fig. 4.2(c), fixing the laser wavelength and intensity while changing the B fields, the zero crossing point of ΔE can be tuned to far from that without the σ^- polarized laser.

In the homonuclear case, since the vector light shifts of the $|+1\rangle$ and $|-1\rangle$ spin states have the same magnitude but the opposite sign, the process $2\,|0\rangle \leftrightarrow |+1\rangle + |-1\rangle$ is not sensitive to uniform light field illumination.

4.2.2 Experiment and results

4.2.3 Spinor mixture preparation and spin dynamics detection

We produce the ultracold ^{87}Rb and ^{23}Na mixture in a crossed optical trap formed by two linearly polarized 1070 nm laser beams with both atoms in their $|-1\rangle$ spin state. By adjusting the final evaporation in the optical trap, either a mixture of essentially pure Bose-Einstein condensate (BEC) of both species or a pure ^{23}Na BEC plus a ^{87}Rb thermal cloud can be obtained. The magnetic field is then ramped up to 60 G and subsequently a single rapid adiabatic passage is applied to transfer simultaneously both atoms to their $|0\rangle$ state with near 100% efficiency. Such a high B filed is necessary to generate enough frequency differences between the $|-1\rangle \rightarrow |0\rangle$ and $|0\rangle \rightarrow$

$|1\rangle$ transitions in order to avoid populating the $|1\rangle$ states via the cascade transition $|-1\rangle \rightarrow |0\rangle \rightarrow |1\rangle$.

The $|0,0\rangle$ mixture is then hold at 4 G for one second to make sure full equilibrium is reached. At this stage, no spin dynamics is detected since ΔE is hI will mainly focus on the processigh. Finally, the magnetic field is ramped to a range of lower values to observe the spin population oscillations at different holding time t. For detection, we switch off the optical trap and apply a magnetic field gradient to separate the different spin states during the time of flight expansion. Absorption image is then used to record the number of atoms N_m^i in each spin states $|m\rangle$ of species i, with i = Na or Rb. The fractional spin population $\rho_m^i = N_m^i/N^i$ can then be obtained from the total number of each species $N^i = N_{-1}^i + N_0^i + N_{+1}^i$.

4.2.4 Coherent heteronuclear spin oscillations in double BEC mixture

We have investigated the heteronuclear spin dynamics in the double BEC mixture. Fig. 4.3 shows the coherent spin population following process (4.27) measured with the double BEC at $B = 0.922$ G. Similar to the previously investigated $|0,-1\rangle \leftrightarrow |-1,0\rangle$ case [24], the synchronized oscillations between the two species as well as between different components of the same species are obvious signatures of the coherent heteronuclear spin dynamics.

With both the double BEC mixture and the BEC + thermal mixture, we have observed the appearance of the third spin state for both ^{87}Rb and ^{23}Na (Fig.2). We have verified experimentally that, with either ^{87}Rb or ^{23}Na atoms alone in spin state $|0\rangle$, no homonuclear spin dynamics can happen at the range of magnetic fields used in this investigation. We thus believe these small amount of population is a result of other heteronuclear spin processes. For instance, the $|-1\rangle$ ^{23}Na atoms generated by process (4.27) may initiate the $|0,-1\rangle \leftrightarrow |-1,0\rangle$ process to produce ^{87}Rb atom in $|-1\rangle$ spin state.

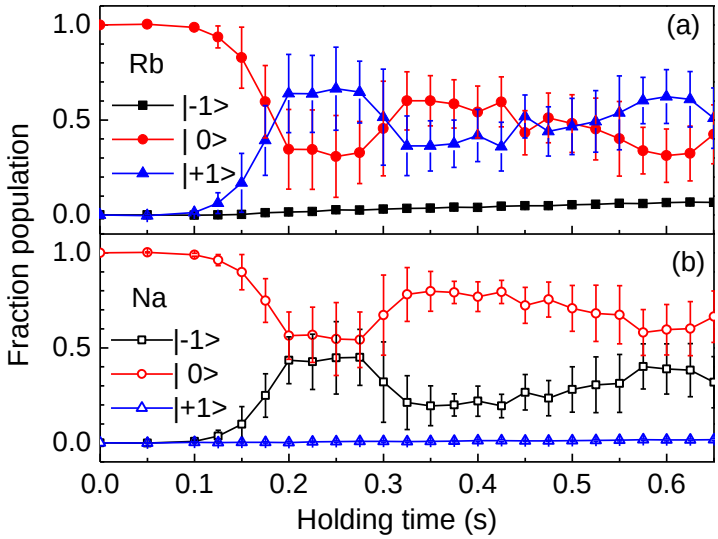

Fig. 4.3. Coherent heteronuclear spin oscillations in the spin-1 ^{87}Rb and ^{23}Na dual BEC mixture following the $|0,0\rangle \leftrightarrow |1,-1\rangle$ process. (a) and (b) show the time evolution of the spin population for ^{87}Rb and ^{23}Na, respectively. The magnetic field is held at $B = 0.922$ G during the whole process. The measured trap frequencies are $(\omega_x, \omega_y, \omega_z) = 2\pi \times (240, 240, 120)$ Hz for Rb and $2\pi \times (280, 280, 140)$ Hz for Na. The number of atoms in the Rb (Na) condensate is $3.0(2) \times 10^4$ ($5.8(4) \times 10^4$). The calculated peak densities are 8.5×10^{14} cm^{-3} and 1.0×10^{14} cm^{-3} for Rb and Na, respectively. Error bars represent 1 standard deviation of typically six repetitions.

In the previous work, the starting point is a non-equilibrium spin configuration, thus the $|0,-1\rangle \leftrightarrow |-1,0\rangle$ spin population oscillation always happens immediately [24]. Here, starting from the zero magnetization $|0,0\rangle$ state, a delay can be observed before the spin dynamics starts. In Fig. 4.3, this delay is on the order of 150 ms. This is very similar to the homonuclear spin-1 case, i.e., starting from spin state $|0\rangle$ of ^{87}Rb or ^{23}Na, the homonuclear spin population oscillation $2\,|0\rangle \leftrightarrow |-1\rangle + |1\rangle$ always starts after a delay [49, 56]. Such a behavior can be explained by the fact that the $|0\rangle$ state of the homonuclear spin-1 system is metastable and spin dynamics can only be initiated by quantum fluctuation which needs some time to build up. Similar physics may be also dictating the heteronuclear dynamics here, but this has not been investigated thoroughly.

4.2.5 Spin dynamics in the mixture of a ^{87}Rb thermal cloud and a ^{23}Na BEC

A complication in using the double ^{87}Rb and ^{23}Na BEC mixture is the phase separation which leads to poor density overlap. This is due to the relatively large interspecies repulsive interaction [42]. In addition, the difference in the trap frequencies for the two species results in a differential gravitational sag which displaces the centers of mass of the two clouds in the vertical direction. The rather high trap frequencies used in Fig. 4.3 are chosen to compensate these effects and increase the density overlap. Nevertheless, we have found experimentally that the spin dynamics in the BEC mixture depends very sensitively on the optical dipole trap. For instance, when a very weak optical trap is used, the spin oscillation becomes totally non-repeatable. We believe this is because of the modulation of the double BEC overlap and thus the spin exchange energy due to the aforementioned reasons. Because of this, for the purpose of investigating control of the spin dynamics, we choose to use a mixture of a thermal cloud of ^{87}Rb atoms and a BEC of ^{23}Na for the rest of this work. In this configuration, the overlap between the two species is always good, and the signal is more repeatable.

Similar to the double BEC case, correlated heteronuclear spin population changes following process 4.27 can also be observed. However, as shown by the time evolution of ρ_0^{Rb} in Fig. 3, the oscillations are strongly over-damped with no periodical features. From Fig. 4.4(a), the B field dependence can be clearly observed from changes of the delay time before the dynamics and the equilibrium fractional population. To quantify this dependence, we fit the data with a Sigmoid function to extract both the cross-over time $T_{1/2}$ and the final saturated fractional population ρ_{min} of ^{87}Rb, with the relation between the two parameters defined by $\rho_0^{Rb}(T_{1/2}) = (1 + \rho_{min})/2$. Fig. 4.4(b) and (c) show the rate of the spin exchange $\Gamma = 1/T_{1/2}$ and ρ_{min} versus B. A maximum of Γ can be observed at around 0.85 G, beyond which the spin dynamics slows down and min keeps increasing. Near the zero crossing point of E at 0.99 G, ρ_{min} is about 0.8 after one second which indicates a very slow spin dynamics.

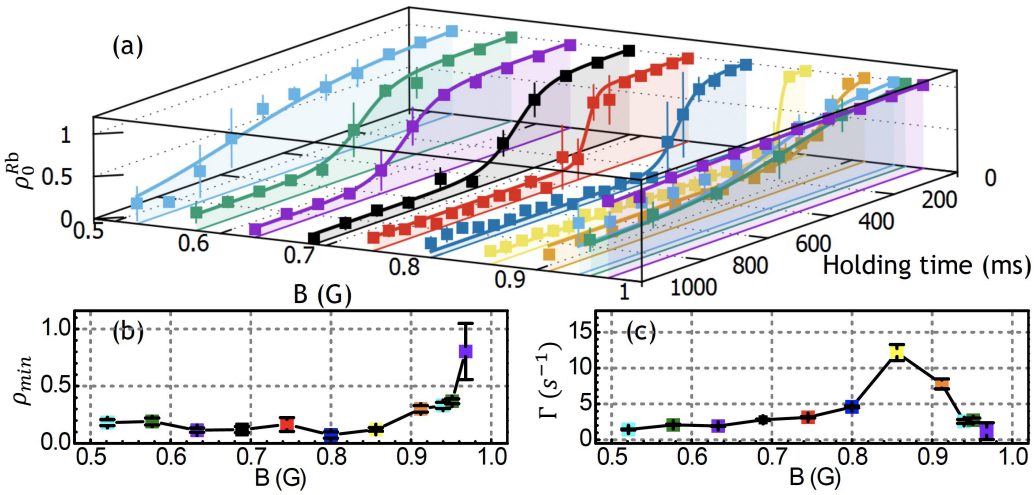

Fig. 4.4. Heteronuclear spin dynamics in the thermal ^{87}Rb and ^{23}Na BEC spin-1 mixture following process 4.27. (a) The time evolution of the spin population for ρ_0^{Rb} for the magnetic field is tuned between 0.521 and 0.968 G. The solid curves are from fit to the Sigmoid function. The error bars represent 1 standard deviation of typically 3 to 5 repetitions. (b) The final fraction ρ_{min} versus magnetic field extracted from the Sigmoid fitting. (c) Γ versus magnetic field from the sigmoid fitting. For these measurements, a nearly spherical trap with measured trap frequencies of $2\pi \times 64$ Hz for Rb and $2\pi \times 72$ Hz for Na is used. The calculated peak densities are 4.6×10^{12} cm^{-3} for the ^{87}Rb thermal gas and 5.6×10^{13} cm^{-3} for the ^{23}Na BEC.

Currently, we lack a quantitative understanding of the mismatch between the maximum of Γ and the zero crossing of ΔE. The fact that we are using a mixture of BEC and thermal atoms makes it hard to treat the problem theoretically, especially with the possible thermal and quantum fluctuations involved. Nevertheless, as has been pointed out in [24], the spinor mixture is a many-body system, while the intuitive understanding based on the argument of ΔE is only true for two particles. The exact peak position of Γ also depends on the homonuclear spin-dependent interactions and possibly the number ratios.

4.2.6 Tuning spin dynamics with microwave

To demonstrate microwave control of the heteronuclear spin dynamics, we broadcast a microwave signal to the atoms after the B field is ramped

to the final value and the microwave frequency is fixed at 6836.18 MHz. Fig. 4.5(a) shows ΔE versus magnetic field calculated from equation 4.39 with the calibrated on resonant Rabi frequencies. There are three zero crossings within the B field range for observing the heteronuclear spin dynamics.

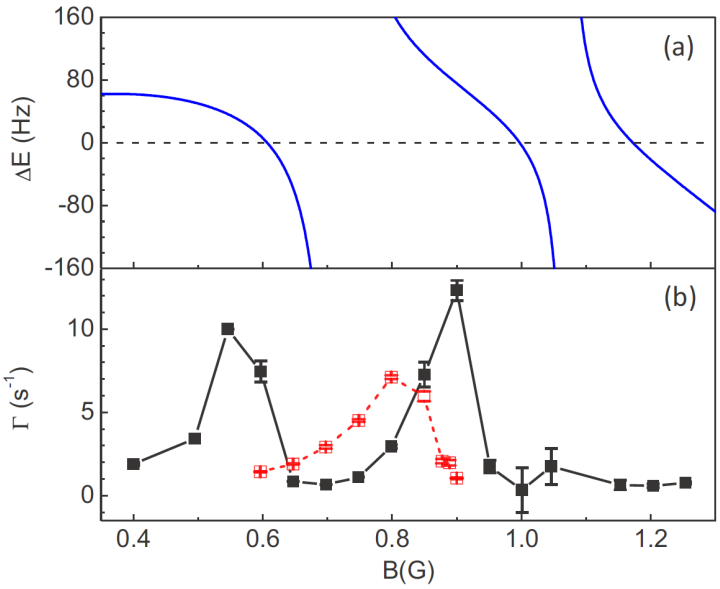

Fig. 4.5. Control of heteronuclear spin dynamics with microwave. (a) The blue curve shows $\Delta E(B, \Delta)$ with the microwave dressing field, which is calculated with equation 4.39 using experimentally measured parameters. (b) The black solid squares are the measured of the spin dynamics in the presence of the microwave; the red open squares are the case without the microwave. All measurements are performed at the same atomic conditions with peak densities of 2.2×10^{12} cm^{-3} for the ^{87}Rb thermal cloud and 5.0×10^{13} cm^{-3} for the ^{23}Na BEC. The curves are for eye guiding.

We map out the B field dependence of the spin dynamics in the presence of the microwave dressing by measuring the rate of the spin exchange Γ following the same procedure as in Sec. 4.2.5 We note that the peak position of Γ depends on the atomic conditions due to the resulting change of the spin-dependent interaction. To see a clear signature of the microwave dressing effect, it is thus important to perform all the measurements with the same atomic conditions. As shown in Fig. 4.5(b), without the microwave dressing, the peak of Γ appears at about 0.80 G. At the same atomic conditions but with the microwave dressing, two peaks of Γ can be observed at around 0.55 and 0.88 G, which are close to the two zero

crossings of ΔE at 0.6 and 1 G, respectively. The same as the case without the additional dressing fields, the maximums of also occur at B fields lower than the $\Delta E = 0$ points.

The apparent shifts of the peak positions of Γ and the appearance of the additional peak are both clear manifestations of the manipulations of the heteronuclear spin dynamics with microwave. However, no peak of Γ is observed for the zero crossing at around 1.2 G. The reason behind this is not fully understood.

4.2.7 Tuning spin dynamics with vector light shift

As discussed in sec. 4.2.1(c), using light field to tune spin dynamics is a unique capability in the heteronuclear spinor system. Since process 4.27 depends directly on the linear Zeeman shift, the effective magnetic field generated by the vector light shift can induce a large change to the spin oscillation resonance. Experimentally, we verify this with the help of a free running external cavity diode laser tuned to 789.817 nm. It is introduced to the atoms along the quantization axis defined by the magnetic field after passing through a $\lambda/4$ waveplate for obtaining σ^- polarization. The 1.15 mm beam diameter is much larger than the size of the atomic clouds to ensure a uniform illumination. From the measured laser power, the peak intensity is calculated to be 0.5 W/cm^2 which corresponds to a sizable differential vector light shift of 0.14 kHz between the $|0\rangle$ and $|1\rangle$ spin states of ^{87}Rb. At this intensity, no significant shortening of the trapping lifetime is observed. As depicted in Fig. 4.6(a), in this configuration the calculated zero crossing point of ΔE with equation 4.43 is shifted to 1.31 G.

Fig. 4.6(b) shows Γ extracted from measuring the spin dynamics at different B field with the light beam. The measurement was performed with essentially the same atomic condition as Fig. 4.5. Comparing withed to the case without the light field (red open squares), the measured shift of the resonance is 0.17 G. This is about 50% smaller than the shift of the zero-crossing points in ΔE. This disagreement could be due to imperfections in the laser beam polarization and/or alignment which result in a smaller shift than the calculation.

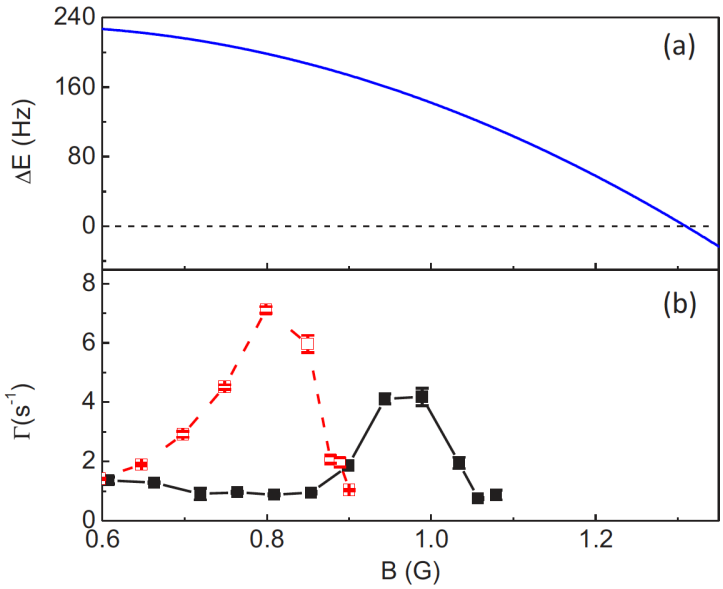

Fig. 4.6. Control of heteronuclear spin dynamics with vector light shift. (a) The blue curve shows the calculated $\Delta E(B, \Delta D1, \Delta D2)$ from equation 4.42 with the σ_- polarized 789.817 nm laser beam. The calculation is based on the peak intensity of the laser beam. (b) The black solid squares are the measured with the vector light shift. The atomic conditions are the same as those used in Fig. 4.5. For comparison, the red open squares show the case without the laser beam. The curves are for eye guiding.

It is also noticed that the peak of Γ is significantly smaller than the B field only case. One possible reason for this is the laser power fluctuation. Since ΔE depends on the laser power, such a fluctuation may diminish the spin population oscillation. In future experiments, the laser power should be carefully stabilized with a feedback control system.

4.3 Conclusion

In summary, we have observed and developed controlling methods for heteronuclear coherent spin dynamics. With the process $|0,0\rangle \leftrightarrow |1,-1\rangle$ in the spin-1 ^{87}Rb and ^{23}Na mixture, we showed that both the detuned microwave field and circularly polarized light field can tune spin dynamics to occur in regions not accessible with magnetic field only. Since both microwave and light fields can be controlled in a fast timescale, the methods studied here should be useful for tuning the spin dynamics time- dependently, such as

quenching. In addition, we find the versatile spatial control of light could be a valuable capability. For instance, by shrinking the laser beam size to smaller than that of the atomic sample, it is possible to introduce a local spin dynamics manipulation [154, 155]. It is also possible to form a standing wave to induce a periodical modulation to the spin dynamics.

4.4 Acknowledgement

The main part of the Sec. 4.2 appears in the published journal article:

Lintao Li, Bing Zhu, Bo Lu, Shizhong Zhang, and Dajun Wang. Manipulation of heteronuclear spin dynamics with microwave and vector light shift. Phys. Rev. A 101, 053611 (2020),

of which the author of this thesis is the first author.

5

Bose polarons in an ultracold mixture of ^{87}Rb and ^{23}Na atoms

An electron moving in solid state crystal will attract the nearby atoms, which form the lattice vibration modes and in turn dress the electron. This mechanism is an important paradigm in quantum many-body physics [66–68]. In 1950s, Herbert Fröhlich proposed the polaron theory that indicates an electrons in bath of the crystal lattice is dressed by a cloud of phonons [156, 157]. Through this theory is the simplest case, it is still too complicated for calculation. Ultracold atomic gases provides an unprecedented platform to analog system with perfect control and measurement. Theoretically, Bose polaron has been investigated more extensively [70–81, 85, 158–168], compared to the Fermi polaron, Bose polaron in BEC background allows the impurity to interact with more than one particles simultaneously, which includes the three-body and other few-body effect. However, it also increase the loss of the atom number, which limits the measurement in strong interacting regime. In this chapter will talk about the experiment study of the Bose polaron in Bose-Bose mixture of ultracold ^{87}Rb and ^{23}Na atoms. We use the rf spectroscopy to measure the energy spectrum and residue of the polaron state at different interaction strength.

In Sec. 5.1, I will give a brief introduction to the Bose polaron theory. I will talk about the Hamiltonian of the system and its solution. In Sec. 5.2, I will introduce the measurement related to the rf spectroscopy of the Bose polaron. In Sec. 5.4, I will describe the fitting method which help us to

find the energy and residue (firstly) of the Bose polaron, which is usually impossible to be measured by Rabi oscillation due to the fast damping.

5.1 Bose polaron theory descriptions

Bose polaron studies the impurity particles immersed in the background of Bose-Einstein condensate (BEC) with $n_0 a_{BB} \ll 1$, where n_0 is the density and a_{BB} is the background scattering length of the condensate. Additionally, the interaction between impurities and background can be tuned by Feshbach resonance, which is introduced in Sec. 2.1. Recently, there are intensive focus on different theoretical approaches to this problem, however, I will only discuss some of them. Typically, we will consider the behaviour of single impurity since the density of the impurity particles are much smaller than the condensate.

Similar to the discussion for Chapter 4, it is convenient to use field operator to describe the system since it is necessary to take into account the excitations in BEC background, which is an analogue to the lattice vibration modes in the Fröhlich Hamiltonian [157]. The full Hamiltonian of the system is

$$\begin{aligned} H = &\sum_k \epsilon_k^B b_k^\dagger b_k + \frac{1}{2\mathcal{V}} \sum_{k,k',q} V_{BB}(q) b_{k+q}^\dagger b_{k'-q}^\dagger b_{k'} b_k \\ &+ \sum_k \epsilon_k^I c_k^\dagger c_k + \frac{1}{\mathcal{V}} \sum_{k,k',q} V_{IB}(q) c_{k+q}^\dagger b_{k'-q}^\dagger b_{k'} c_k, \end{aligned} \tag{5.1}$$

where b_k ($b_k^\dagger$) and c_k ($c_k^\dagger$) are the annihilate (create) a boson and an impurity, respectively. $\epsilon_k^{B,I} = k^2/2m_{B,I}$ is the kinetic energy term of bosons and impurities with the momentum defined by k. Here, $m_{B,I}$ denotes for the atomic mass of a boson or a impurity, respectively. Thus the first term of two rows describe the kinetic energy of the system. The remaining terms indicate the interaction energy from condensate and the boson-impurity interaction. The two-body potential $V_{BB}(q)$ and $V_{BI}(q)$ are the Fourier transform of two-body contact interaction. As we have already discussed in Sec. 2.2, the interaction is assumed to be short-ranged thus $\sum_q V_{BB}(q) = g_{BB} = \frac{4\pi\hbar^2 a_{BB}}{m_B}$ and $\sum_q V_{IB}(q) = g_{IB} = \frac{2\pi\hbar^2 a_{IB}}{\mu_{IB}}$, where $\mu_{IB} =$

$m_B m_I/(m_B+m_I)$ is the reduced mass. However, the equation is limited to mean-field approximation, which is not always true for boson-impurity interaction. For zero-range model, the coupling constants has an ultra-violet divergence, which is regularized by

$$\frac{1}{g_{IB}} = \frac{\mu_{IB}}{2\pi a_{IB}\hbar^2} - \frac{1}{\mathcal{V}}\sum_k \frac{2\mu_{IB}}{k^2}, \tag{5.2}$$

where $\mathcal{V}$ is the volume of the system.

For a stable repulsive interacting BEC ($0 < n_0 a_{BB} \ll 1$), the ground state can be well described by the Bogoliubov theory, where we replace b_k with $\sqrt{N}+\delta b_k$ and use the small δb_k to describe the fluctuation. Since we can neglect the terms higher than quadratic term. Under the Bogoliubov transformation [94], the elementary excitations in the condensate are the collective Bogoliubov modes. And the Hamiltonian is transformed into [78]

$$\begin{aligned} H &= H_0 + H_I \\ &= E_g + \sum_k \gamma(k) a_k^\dagger a_k + \sum_k \epsilon_k^I c_k^\dagger c_k \\ &+ \frac{g_{IB}}{\mathcal{V}}\left(N\sum_k c_k^\dagger c_k + \sqrt{N}\sum_{k,q}\mathcal{R}(q)\left(c_{k+q}^\dagger c_k a_q + c_{k+q}^\dagger a_{-q}^\dagger c_k\right)\right. \\ &\left. + \sum_{k,k',q}\mathcal{D}(k,k') c_{q+k-k'}^\dagger a_{k'}^\dagger a_k c_q \right), \end{aligned} \tag{5.3}$$

where a_k ($a_k^\dagger$) is the annihilation (creation) operator of Bogoliubov phonon under the transformation:

$$\begin{aligned} \delta b_k &= u_k a_k^\dagger - v_k a_{-k}^\dagger, \\ \delta b_{-k} &= u_k a_{-k}^\dagger - v_k a_k^\dagger \end{aligned} \tag{5.4}$$

with the dispersion relation given by $\gamma(k) = \sqrt{(\epsilon_k^B)^2 + 2\epsilon_k^B g_{BB} n_0}$. The real and positive coherence factors are $u_k^2 = [1 + (\epsilon_k^B + g_{BB}n_0)/\gamma(k)]/2$ and $v_k^2 = [-1 + (\epsilon_k^B + g_{BB}n_0)/\gamma(k)]/2$. Here, we use the mean-field approximation which ignores the number fluctuation of BEC and $\sum_k a_k^\dagger a_k \approx \sum_k \left|a_k^\dagger a_k\right| = N$. $\mathcal{R}(q) = u_q - v_q$, $\mathcal{D}(k,k') = u_k u_{k'} + v_k v_{k'}$ and E_g is the ground state energy of the weak-interacting BEC.

The interacting Hamiltonian H_I is shown by the last two rows of equation 5.3 where the first term is the mean-field shift with the energy given by $g_{IB}\frac{N}{\mathcal{V}} = g_{IB}\bar{n}_{\text{BEC}}$. The second term describes photon exchange between the impurity and surrounding medium, which is same to the origin Fröhlich Hamiltonian. And the third term describes the photons being scattered by the impurities.

There are various method to solve the Hamiltonian 5.3 including the T-matrix [77, 158], renormalization group approach [81, 162], quantum Monte-Carlo [86, 159, 160] and the variational theory [85, 166, 168, 169]. I will give a brief introduction to two of them, which are used for our prediction.

5.1.1 Variational theory

Similar to the calculation for Fermi polaron [169], we can use the variational theory to determine the ground state of the system. The trial wave function for polaron with momentum q is given by [78]

$$|\Phi(q)\rangle = \left(\phi_0(q)c_q^\dagger + \sum_{k\neq 0}\phi_k(q)c_{q-k}^\dagger a_k\right)|\text{BEC}\rangle \tag{5.5}$$

where $\phi_0(q)$ and $\phi_k(q)$ are the variational parameters, $|\text{BEC}\rangle$ is the ground state Bose-Einstein condensate with weak interaction. The equation here only consider the first order which describes only one photon excitation or two-body correlations between the impurity and surrounding medium.

The theoretical procedure is to minimize the energy of the trial wave function by numerically varying the parameters. That gives the following differential equation:

$$\frac{\partial}{\partial\phi_i(q)}\langle\Phi(q)|\,H - E\,|\Phi(q)\rangle = 0, \tag{5.6}$$

which should be fulfilled for all the ϕ parameters. At each momentum q, we have the minimized energy E(q), which provides the dispersion relation of Bose polaron. And the effective mass is defined by

$$E(q) = E(0) + \frac{q^2}{2m_{eff}} + \mathcal{O}(q^4). \tag{5.7}$$

Here, $E(0)$ is ground state polaron energy or the polaronic binding energy and m_{eff} is the effective mass of single impurity dressed by BEC, which can be connected to the quasiparticle residue $Z \equiv |\phi_0|^2$.

5.1.2 T-matrix method

For the Hamiltonian given by equation 5.1, we use T-matrix to describe the interaction $V_{BB}(q)$ and $V_{IB}(q)$ [77]. For zero energy, the scattering matrix is given by

$$\mathcal{T}_{BB} = \frac{4\pi\hbar^2 a_{BB}}{m_B}, \mathcal{T}_{IB} = \frac{2\pi\hbar^2 a_{IB}}{\mu_{IB}}. \tag{5.8}$$

And the weakly interacting BEC is described by the imaginary time Bose Green's functions. The Fourier transforms are [158, 170]

$$\begin{aligned} G_{11}(k,z) &= \frac{u_k^2}{\hbar z - \gamma(k)} - \frac{v_k^2}{\hbar z + \gamma(k)}, \\ G_{12}(k,z) &= G_{21}(k,z) = \frac{u_k v_k}{\gamma^2(k) - (\hbar z)^2}. \end{aligned} \tag{5.9}$$

On the other hand, the main features of the quantum impurity are given in terms of its retarded Green's function. This function is given by

$$G(k,z) = \frac{1}{\hbar z - \frac{k^2}{2m_I} - \Sigma(k,z)}, \tag{5.10}$$

where k is the momentum and z is the energy of impurity and the key of this Green function is the self-energy $\Sigma(k,z)$. And the self-energy is given by

$$\Sigma(k,z) = n_0 \mathcal{T}_{IB}(k,z) + \sum_q v_q^2 \mathcal{T}_{IB}\left(q+k, z-\gamma\left(q\right)\right), \tag{5.11}$$

where $T_{IB}(k,z)$ is the impurity-boson $\mathcal{T}$ scattering matrix. The self energy is is taken using the ladder-approximation. As shown by the Fig. 5.1 (Top), the first term stands for the mean-field like interaction between the impurity and condensate. The second term represents the dressing of impurity with the depleted bosons, which come from the condensate due to the boson-boson interactions. Using the Bethe-Salpeter equation for the impurity-boson interaction, the $\mathcal{T}$ scattering matrix is given by

$$\begin{aligned}\mathcal{T}_{IB}(p,z) &= \frac{g_{IB}}{1-g_{IB}\Pi(p,z)} = \mathcal{T}_{IB} + \mathcal{T}_{IB}^2\Pi(p,z) + \cdots \\ \Pi(p,z) &= -\sum_{i\omega_\nu}\sum_{k} G_I(p-k, z-i\omega_\nu)G_{11}(k,i\omega_\nu),\end{aligned} \tag{5.12}$$

where $G_I(p,z)$ is the ideal Green's function of impurity. As shown by the Fig. 5.1 (Below), the $\mathcal{T}$ scattering matrix is given by the infinite sum over two-particle reducible ladder-type diagrams which is the combination of repeated impurity-boson scattering.

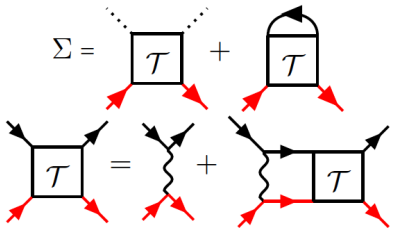

Fig. 5.1. Diagrams related to the non-selfconsistent $\mathcal{T}$ approximation. (Top) The self-energy of the impurity. (Below) In-medium $\mathcal{T}$ scattering equation. The red solid line stands for the impurity propagators. The solid black line stands for the BEC Green's function and the dashed line denotes the condensate bosons. The wavy line is $\mathcal{T}_{IB}$. Credit: A. Camacho-Guardian.

The energy of the impurity is given by the solution of self-consistent equation:

$$\omega_k = \frac{k^2}{2m_I} + \Sigma(k,\omega_k). \tag{5.13}$$

The spectral function is connected to retarded Green's function:

$$A(k,\omega) = -2Im\left(G(k,\omega)\right). \tag{5.14}$$

We focus on the ground state thus the spectral function can be simply denote by $A(\omega)$. The spectral weight or quasi-particle residue is given by

$$Z(k) = \frac{1}{1 - \partial_\omega Re\Sigma(k,\omega)} \mid_{\omega=\omega_k} \tag{5.15}$$

And the decay width of the spectrum is given by.

$$\Gamma(k) = -Z(k) Im\Sigma(k,\omega_k) \tag{5.16}$$

5.1.3 Polaron energy, residue and rf spectrum

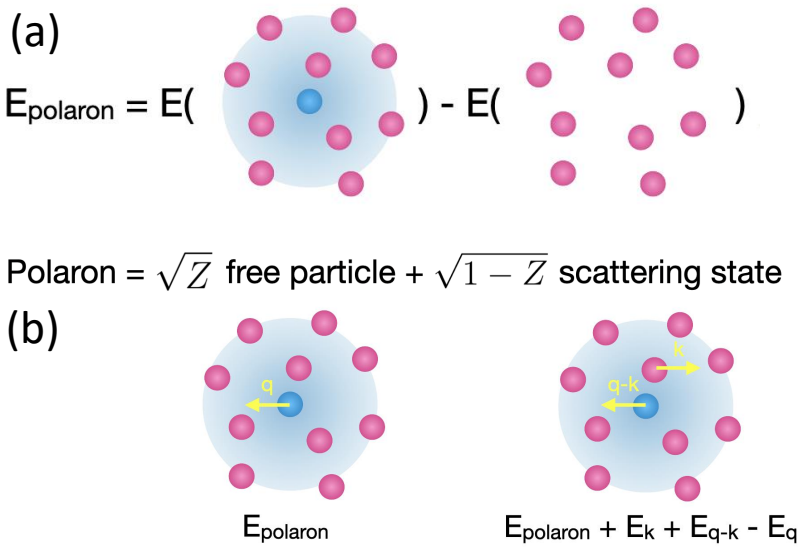

Fig. 5.2. The concept of the polaron energy and residue. (a) Polaron energy. (b) Polaron residue. The wave function of polaron can be divided into the free particle and scattered state. Polaron residue Z is defined as the weight of free particle state.

The polaron energy can be defined as the energy of the system that contains an impurity minus the energy of the system without the impurity (Fig. 5.2(a)). Thus the polaron energy is a generalized chemical potential. As shown by the Fig. 5.5(a), we can use rf transtion between two different Zeeman sublevels to probe the polaron energy of the dressing state. For the $|\uparrow\rangle$ state, the interaction between $|\uparrow\rangle$ state impurity atoms and BEC is weak. However, for the $|\downarrow\rangle$ state, we can tune the interaction between the

impurity and BEC via Feshbach resonance. The dressing energy of the $|\uparrow\rangle$ state is exactly the polaron energy which can be probed by the detuning $\Delta = \nu_{rf} - \nu_0$ that described the frequency shift of the rf transition. ν_0 is the bare atom transition frequency which is given by the Zeeman splitting between the two sublevels.

Under the two-body theory, the polaron wave function $|\Phi(q)\rangle$ is descrived by Equation. 5.5, q is the momentum of the polaron state. As shown by the Fig. 5.2(b), this wave function can devided into two parts, the first part with amplitude $\phi_0(q) \equiv \sqrt{Z}$ describes the free particle state that do not have momentum exchange with the surrounding Bogoliubov phonons. The second part with amplitude $\phi_k(q)$ $(k \neq 0)$ is the scattering state that comes from impurity scattered by the Bogliubov phonons. And the energy of the scattering state is not only decieded by the polaron energy $E_{polaron}$ but also the kinetic energy introduced in the scattering process, which is always larger than zero.

With the given wave function in Equation. 5.5. The rf spectrum of a single polaron is derived from Fermi's Golden rule:

$$\begin{aligned} A(\Delta) &= 2\pi Z\delta(\Delta - E_{polaron}) + 2\pi \sum_k \phi_k(q)\delta(\Delta - E_{polaron} - E_k + E_q - E_{q-k}) \\ &= 2\pi Z\delta(\Delta - E_{polaron}) + 2\pi(1-Z)A_{incoh}(\Delta - E_{polaron}). \end{aligned} \tag{5.17}$$

where the first term describes the coherent rf transition of free particle state with amplitude Z and the second term is the incoherent many-body continuum with amplitude $(1 - Z)$ that gives the summation of all the possible two-body scattering states. The polaron residue Z is defined as the weight of free paricle states in the rf spectrum. Since the incoherent part shows a very different unsymmetrical lineshape, we may use Z as the fitting parameter to seperate the coherent part from incoherent part in the experimental spectrum. We will talk more about this fit in Sec. 5.4.

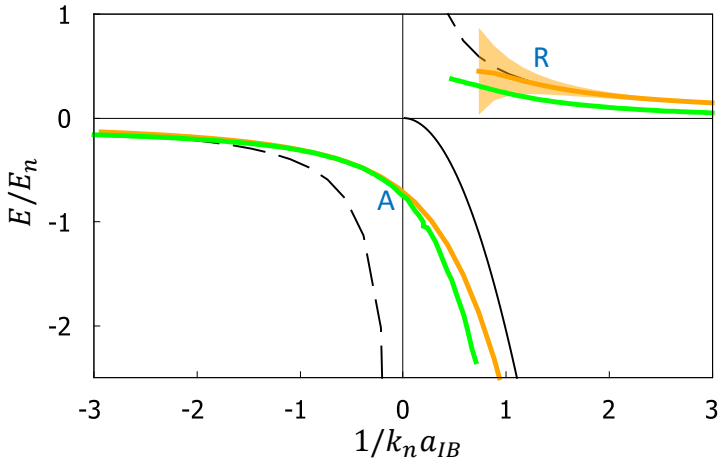

Fig. 5.3. The calculation results of energy spectrum of an impurity immersed in homogeneous Bose-Einstein condensate. The energies of attractive and repulsive branch are shown by the curves labelled with A and R, respectively. We show the results from two-body variational calculation (orange curve) and $\mathcal{T}$ approximation (green curve). The orange shading area denotes the broadening from limited lifetime of repulsive polaron, which is from the decay into lower energy state, and is calculated by the imaginary part of the polaron energy. For comparison, the black solid line shows the two-body molecular state energy and the dashed line shows the energy shift given by mean-field theory.

5.1.4 Two-body theory prediciton of Bose polaron's energy and residue

In our experiment we use ^{87}Rb as impurities and ^{23}Na BEC as the background media. The the boson-boson and impurity-impurity scattering lengths $a_{\mathrm{BB}} = 54.5a0$ [90] and $a_{\mathrm{II}} = 100.4a0$ [91] are both constant. We introduce the parameter $1/k_n a_{\mathrm{IB}}$ with $k_n = (6^2 n_{\mathrm{BEC}})^{1/3}$. The energy scale of the system is then $E_n = \hbar k_n^2/2m_{\mathrm{Na}}$ with m_{Na} the mass of sodium.

The theoretical prediction of Bose polaron's zero momentum energy spectrum for our ^{87}Rb-^{23}Na system is shown in FIg. 5.3, where the result of variational theory [78] and $\mathcal{T}$ approximation [77] are show by the orange and green curves, respectively. The spectrums can be divided into attractive (noted with A) and repulsive branch (noted with R). For weak interactions, both repulsive and attractive branch approaches the mean-field shift (dashed black curve), which is the impurity's mean-field energy with attractive or repulsive interaction from surrounding BEC.

However, when the interaction is getting stronger, the behaviours of two branches are very different from the mean-field shift. For the attractive branch, as stronger interaction approaches, the polaron state is well defined even when the mean-field shift diverges. Finally, the calculated energy of attractive polaron approaches the two-body molecular state (solid black curve), which results from the two-body correlations. Between the mean-field shift and dimmer energy, we can see a smooth crossover which defines the quasiparicle. Since the attractive branch is a ground state, the attractive polaron has long lifetime and narrow line shape.

For the repulsive branch, when we approach strong interactions, the lifetime becomes short and the energy spectrum is broadened, which is indicated by the orange shading area. This effect comes from the decay of impurity from repulsive branch to lower-lying states. And it will flatten the spectrum if the lifetime is comparable with our detection time.

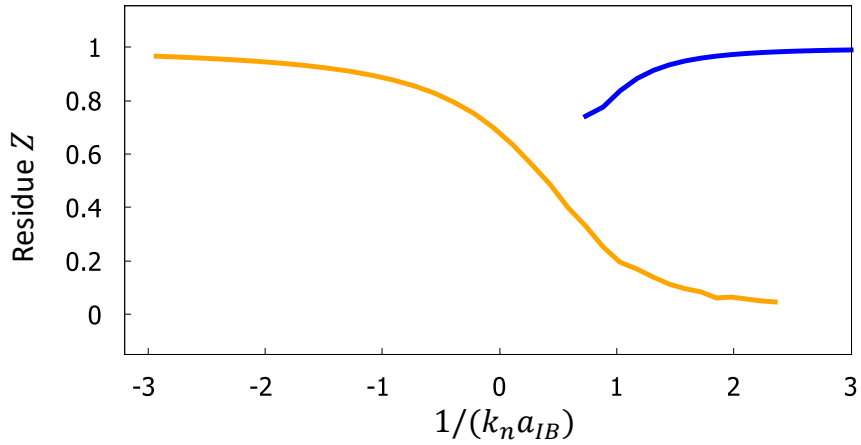

Fig. 5.4. Residue Z at different interaction strength. The orange line shows the attractive branch and the blue line shows the repulsive branch. The curves are calculated from two-body variational theory.

Fig. 5.4 shows the corresponding polaron residue Z at different interaction strength. When the interaction between the impurity and BEC is weak, the residue $Z \equiv |\phi_0|^2$ approaches 1 which describes the bare impurity part in the wave function. As the interaction strength $1/k_n a_{IB}$ approaches 0, the phonon exitations can no longer be neglected and Z is decreased. For the attractive polaron, as $1/k_n a_{IB}$ across the unitary regime to the positive value, $Z \to 0$ as the polaron approaches the two-body bound state.

5.1.5 Three-body correlations

In the previous section, we introduced the variational theory and $\mathcal{T}$-matrix method, which beyond the mean-field theory and Fröhlich model. However, the methods only include up to two-body correlations, which may not be enough for the Bose polaron.

Since the three-body Efimov correlation may play an important role in the Bose polaron theory, especially for the attractive branch, we can include the three-body terms in the trail function of variational theory. To be brief, we consider the zero momentum case and the trial wave function is [85]

$$
\begin{aligned}
|\Phi\rangle = \Bigg(& \phi_0 c_0^\dagger + \sum_k \phi_k c_{-k}^\dagger a_k \\
& + \frac{1}{2} \sum_{k_1,k_2} \phi_{k_1 k_2} c_{-k_1-k_2}^\dagger a_{k_1} a_{k_2} + \gamma_0 d_0^\dagger + \sum_k \gamma_k d_{-k}^\dagger a_k \Bigg) |BEC\rangle \, .
\end{aligned}
\tag{5.18}
$$

The first line is same as equation 5.5, which describes the bare impurity dressed by one Bogoliubov mode. And the first term of the second line describes the impurity dressed by two Bogoliubov mode. The remaining terms indicate the bound state formed by an impurity and a boson, which can be dressed by a Bogoliubov mode.

The calculation results of this trial wave function shows that three-body correlations become important for strong interacting regime, which leads to the avoid crossing of an Efimov trimer state. Compare with the results of two-body correlations, the energy and quasiparticle residue are lowered significantly at an intermediate interaction strength, even there is no Efimov trimmer state in a vacuum [85].

5.1.6 About the comparison between theory and experiment

The theoretical approach mentioned above mainly focuses on the energy and residue of the quasiparticle, which comes from the free particle state

of polaron's wave function. However, for the experiment, there are some aspects that are not included by the above theories.

For the both the variational approach and the $\mathcal{T}$-matrix method, the theories do not include the three-body recombinations (see Sec. 2.3.2), which should introduce the loss of impurities. To eliminate this problem, we introduce the fast detection method. However, this atom loss should still affect the polaron signal amplitude at strong interaction regime. For the comparison at this regime, we need to confirm that the signal strength is not being severely affected by the loss of impurities. This can be done by comparing the total area of the experimental spectrum with the bare atom transition spectrum.

Another concern relative to the above mentioned theory is that both the variational approach and the $\mathcal{T}$-matrix method include only a few excitations in their wavefunction, which may not be enough for the Bose polaron at strong interaction regime. The renormalization group theory [162] suggests that the polaron spectrum will change qualitatively at strong coupling, which can no longer be described by single coherent peak with residue Z and all the remaining incoherent spectrum located at $E > E_p$. This theory also predicts an infinite number of phonons in the polaron cloud near the unitary regime which gives a broad and featureless polaron spectrum. However, the behavior of attractive Bose polaron at strong interaction regime is still an open question and the bad signal to noise ratio at strong interaction regime also limits the comparison between the theory and the experiment.

5.2 The Bose polaron experiment

A cold atom system for the polaron experiment includes impurity particles and surrounding media. Depending on the quantum statistics of the bath's constituent particles, polaron can be divided into the Fermi polarons with a degenerate Fermi gas and Bose polarons within a Bose-Einstein condensate.

The ideal polaron experiment requires a system of one of few impurities immersed in a homogeneous background media, which is usually difficult since the harmonic trap potential cause the inhomogeneous density distribution. For the Fermi polaron, it is actually not a big problem, due to the existence of Fermi pressure, the size of Fermi gas is usually much larger than the size of impurity component and the impurity particles will only see the density near the central region.

However, as we have discussed in Sec. 2.2 and 3.4.1, the Tomas-Fermi radius of the BEC is much smaller than the usual size of Fermi sea and even the small gravitational sag will significantly affect the mixture of two different species. For heteronuclear Bose-Bose mixture, another difficulty is that the number of impurities should be kept below the critical number to prevent double BEC mixture. Since ^{87}Rb and ^{23}Na are immersible under background scattering length, the double BEC mixture will not only change the roles of impurities but also affect the overlap. To solve this problem, we have developed a better control system for ^{87}Rb atom number, which is discussed in Sec. 3.3.3. And we also evaluate the noise of the absorption image with low atom number, which is discussed in Sec. 3.7.3.

5.2.1 A review of previous Bose polaron experiments

Before talking about our experiments, it is quite helpful to look at several previous work and see how they deal with these problems.

In JILA's experiment [22], the Bose-Fermi mixture of ^{87}Rb and ^{40}K is used. Because they are using the Fermi sea of ^{40}K as the impurities, the impurity gas is actually much larger than the BEC of ^{87}Rb. And the polaron signal is totally submerged by the bare atom transition from non-overlapped part. To solve this problem, they have introduced the inverse Abel transformation to get the signal exactly coming from the impurities near the center of the BEC. This method requires a good image resolution and an excellent signal to noise ratio of the absorption image, which is doable for their experiment since they don't need to worry about the critical number problem for Fermi impurities. In their experiment, the ^{40}K and ^{87}Rb atoms also show

different gravitational sag in the trap. However, their interspecies interaction is attractive which cancels the overlap problem in vertical direction.

Instead of using heteronuclear mixture, Denmark's experiment [69] uses single species ^{39}K BEC in different spin states. In their experiment, the impurities are created by the spin flip of some of the atoms in BEC, which avoids the non-overlapped impurities problem. However, the density inhomogeneous is still there for the impurities in different position. And they introduced the theoretical prediction that includes broadenings from inhomogeneous density distribution. Instead of directly detecting the number of impurities, they observe the three-body loss of the BEC due to the existence of impurities, which made their measurement be sensitive to the atom number stability of the system.

In MIT's experiment [23], they use the Bose-Fermi mixture of ^{23}Na and ^{40}K. A dual wavelength optical dipole trap is introduced to selectively confine the ^{40}K impurities and also decrease the gravitational sag differences on vertical direction. The attractive interspecies interaction also increases the density overlap between two species. More interestingly, they take the advantages of the density inhomogeneous in an elongated optical dipole trap. By separating the polaron signal at different positions, they can study the polaron spectrum at various reduced temperatures in a single measurement.

5.2.2 The rf spectrocopy measurement

As shown in the Fig. 5.5(a), the starting point of our experiment is an weak interacting imbalanced mixture of a thermal sample of ^{87}Rb atoms in $|\uparrow\rangle \equiv |F = 1, m_F = 0\rangle$ hyperfine Zeeman state (yellow ball) and a pure BEC of ^{23}Na atoms in $|F = 1, m_F = 1\rangle$ state (red ball) co-trapped in a pancake-shaped optical trap formed by two crossed 947 nm laser beams. The special wavelength is designed to increase the density overlap between ^{87}Rb and ^{23}Na atoms since the centres of mass of the two species will overlap with each other as they feel the same trap frequencies or gravitational sags [128]. To further increase the density overlap in horizontal direction, we apply a low power 805 nm trap light which compress

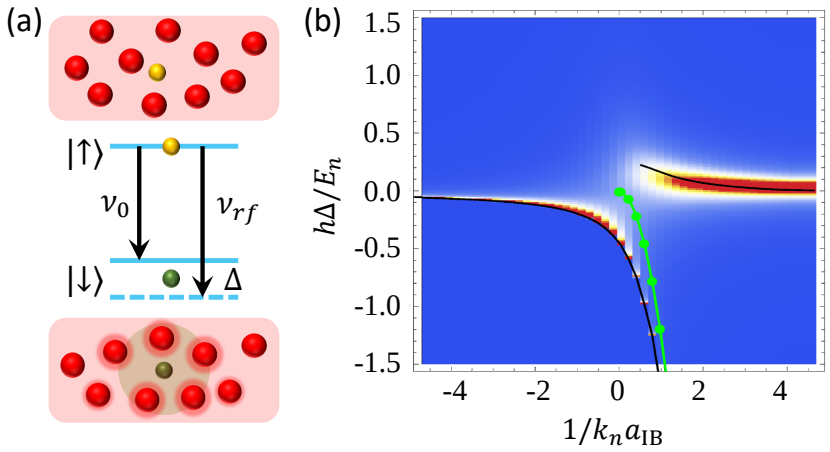

Fig. 5.5. Probing the Bose polaron with rf injection spectroscopy. (a) An $|\uparrow\rangle$ impurity atom (yellow sphere) immersed in the BEC bath (red sphere) experiences only the mean field interaction. A rf pulse drives the impurity to the strongly interacting $|\downarrow\rangle$ state (green sphere) where a polaron can be formed. ν_0 is from the Zeeman splitting between the $|\uparrow\rangle$ and $|\downarrow\rangle$ states. (b) Calculated Bose polaron spectra function for a homogeneous BEC. The solid black curves are the zero-momentum polaron energy, while the false colour graph includes contribution from the many-body continuum. The green curve shows the binding energy of the heteronuclear Feshbach molecules. (see text for details)

the radial size of the ^{87}Rb thermal sample. The wavelength is close to the ^{87}Rb's D1, D2 lines and has no significant effect to the Na atoms. With the combined potential, the measured radial and z-direction (vertical) trap frequencies for Na (Rb) are $f_{\mathrm{Na},\rho}(f_{\mathrm{Rb},\rho}) = 2\pi \times 52$ $(2\pi \times 83)$ Hz and $f_{\mathrm{Na},z}(f_{\mathrm{Rb},z}) = 2\pi \times 183$ $(2\pi \times 183)$ Hz, respectively. And the typical number of atoms is $2.3(2) \times 10^5$ $(3.5(9) \times 10^3)$ for ^{23}Na (^{87}Rb). The temperature measured by thermal Rb sample is 120 nK which indicates the peak density of ^{87}Rb is $n_{\mathrm{Rb}} = 1.1 \times 10^{12}$ cm^{-3} under the mean-field interaction with ^{23}Na BEC. This density is around 60 times smaller than the peak density of ^{23}Na, which is $n_{\mathrm{BEC}} = 7.1 \times 10^{13}$ cm^{-3}. Thus ^{87}Rb can be treated as impurities.

In the $|\uparrow\rangle$ state, the ^{87}Rb impurity interacts with the Na BEC weakly as characterized by a constant background interspecies scattering length $a_{bg} = 66.77a_0$ [92]. Thus the $|\uparrow\rangle$ state impurity energy which can be well described by the mean-field shift, which is indicated by the solid lines in Fig. 5.5(a). The rf pulse then drive the impurity to the $|\downarrow\rangle \equiv |F = 1, m_F = 1\rangle$ state (green ball), where the impurity-bath interaction can be tuned from weak to strong with a magnetic Feshbach resonance. The impurity-boson

interaction is tuned with the Feshbach resonance at $B_0 = 347.64$ G following $a_{\mathrm{IB}} = a_{bg}(1 - \Delta_0/(B - B_0) - \Delta_1/(B - B_1))$. Here $\Delta_0 = 5.2$ G are the center and width of the Feshbach resonance, while $B_1 = 478.83$ G and $\Delta_1 = 4.8$ G are from another resonance. Near B_0, the boson-boson and impurity-impurity scattering lengths $a_{BB} = 54a_0$ and $a_{II} = 100.4a0$ are both constant. The magnetic field is tuned from 346.7 to 348.4 G where the interaction is mainly decided by first resonance, both the repulsive and attractive branches can be reached (Fig. 5.5(b)).

We use the inverse rf spectroscopy to measure the polaron spectrum of $|\downarrow\rangle$ state versis $1/k_n a_{\mathrm{IB}}$ by applying a rf pulse to probe the $|\uparrow\rangle \rightarrow |\downarrow\rangle$ transition for a range of magnetic fields. And the pulse frequency ν_{rf} minus the bare atom transition frequency ν_0 is the detuning Δ, which describe the energy dressing of surrounding BEC. In the experiment, we use a Gaussian rf pulse with a 57 μs 1/e^2 full width and a Rabi frequency Ω_0 that can drive a $\pi/2$ pulse on the bare ^{87}Rb transition. From Fourier transformation, the rf line shape can be expressed as $R(\nu) = \exp(-2\nu^2/\delta\nu^2)$ with $\delta\nu = 5.6$ kHz the pulse duration limited linewidth. The bare atom transition gives $\delta\nu = 6.4$ kHz, which also includes the broadening from magnetic field noise. The characteristic energy scale E_n is $h \times 57$ kHz for the given condition. The linewidth of the rf spectroscopy corresponds to around $0.1E_n/h$ and is thus enough to resolve details of the spectrum.

After the rf pulse, the number of $|\uparrow\rangle$ state ^{87}Rb atoms being transferred to the $|\downarrow\rangle$ state ($N_\downarrow$) are detected immediately with a high field $in\ situ$ absorption imaging setup. The magnetic field is then ramped down and the remaining number of atoms in $|\uparrow\rangle$ ($N_\uparrow$) is detected at low field. Both imaging systems are calibrated carefully following standard procedures. From these numbers, the fractional population transferred to $|\downarrow\rangle$, $f_\downarrow = N_\downarrow/(N_\downarrow + N_\uparrow) \equiv N_\downarrow/N$, is then obtained for each ν_{rf}. We normalize $f_\downarrow$ with the pulse area of the bare Rb atom spectrum, thus we can remove the gain error of antenna and the on resonance rf signal is exactly the definition of quasiparticle residue for a homogeneous system.

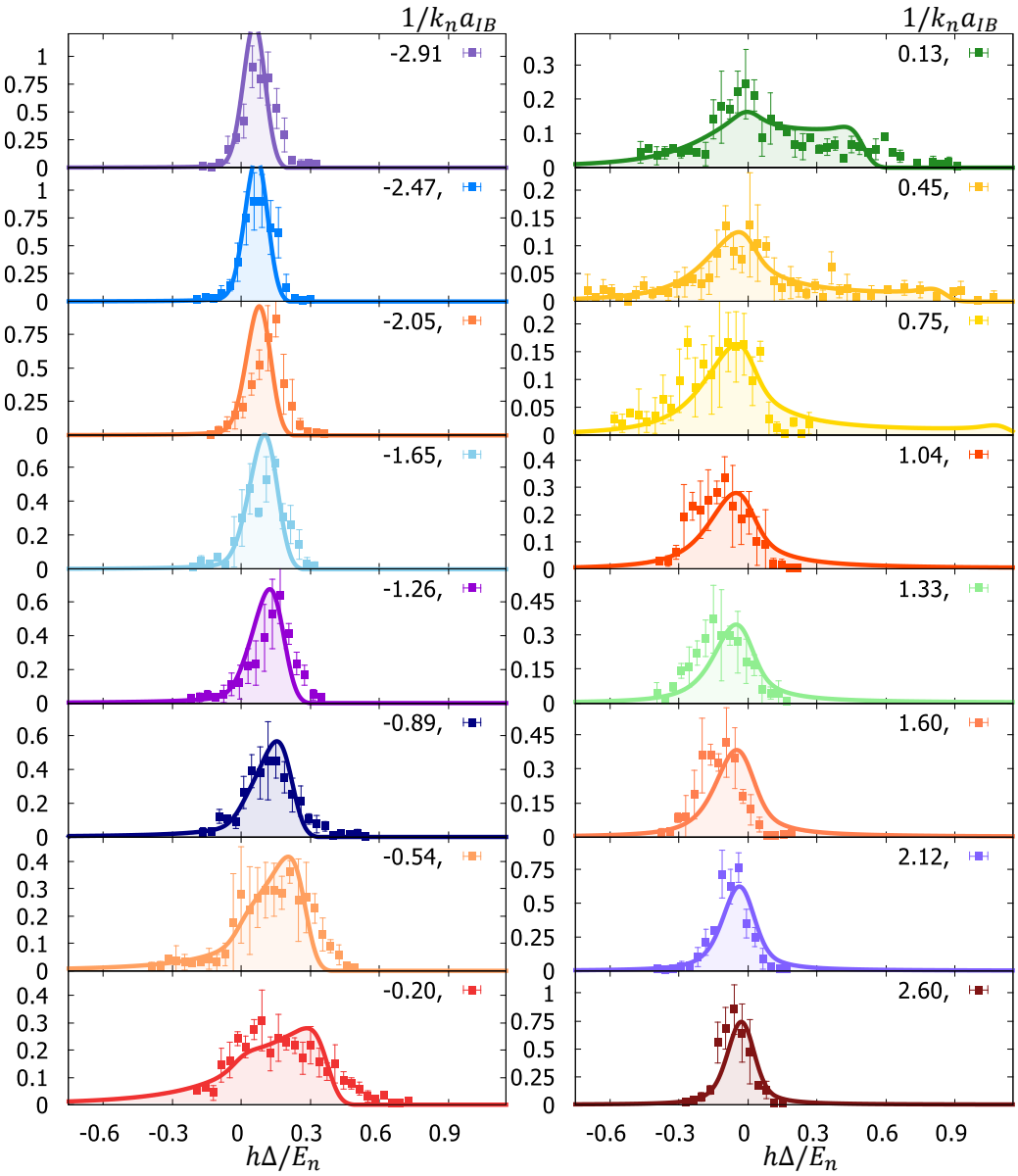

Fig. 5.6. The rf spectrum of ^{87}Rb in ^{23}Na BEC. The rf signal $f_\downarrow$ as a function of detuning Δ for different values of interaction parameter $1/k_n a_{\mathrm{IB}}$. The solid curves shows the theoretical spectrum normalized by the frequency integrated area same as experimental spectra. There are usually 3 repetitions for each data point and the error bar shows the statistic error.

5.3 Spectroscopy of the Bose polaron

Figure 5.6 shows the obtained spectral response versus $h\Delta/E_n$, with $\Delta = \nu_{\mathrm{rf}} - \nu_0$, for different $1/k_n a_{\mathrm{B}}$. Compared with the calculation for the ho-

mogeneous polaron in Fig. 5.5(b), the line shape is much more complex and several main features can be identified. For the attractive branch, the weight of the signal shifts to larger Δ when $1/k_n a_{\mathrm{IB}}$ is tuned toward unitarity and eventually crosses smoothly to the $a_{\mathrm{IB}} > 0$ side. Double peaks can be seen for $1/k_n a_{\mathrm{IB}} = -0.20$ and 0.13 which signals the competition from and the eventual transition to the repulsive branch. For $1/k_n a_{\mathrm{IB}}$ from 1 to 2.6, a well defined repulsive branch is also observed. The spectra are increasingly broadened as the interaction strength is ramped up from both the attractive and and the repulsive sides. As a result, for $1/k_n a_{\mathrm{IB}}$ from -0.54 to 0.74, the amplitude of the signal is significantly reduced.

In the strongly interaction region, as shown by the Fig. 5.5(b), the broadening can be partially attributed to the many-body continuum which is a unique feature of the Bose polaron due to the boson nature of the bath [79]. The origin of this continuum is incoherent excitations of the BEC which lies above the quasiparticle pole of the polaron. The onset of this continuum is determined by the Landau superfluid criterion. However, for weak and intermediate interactions, where contributions from the many-body continuum is small, significant broadening is still observed. This is due to the inhomogeneity of the BEC density introduced by the harmonic trap and the finite rf linewidth $\delta\nu$. In addition, due to the imperfect impurity-BEC overlap in the vertical direction, some Rb atoms are never part of the polaron. Overall, these lead to an averaging effect in the experimental spectral function over the quasiparticle poles for different segments of the trap which persists for all interaction strengths.

To model the experimental spectral function, we employ a field-theory (non) self-consistent $\mathcal{T}$ approximation (NSCT/SCT) approach that includes the Feshbach resonances and many-body physics. In Fig. 5.6, the solid curves indicate the polaron spectral functions calculated with the real experimental parameters reproduce the observed signals successfully without introducing any fitting parameters. This approach is based on the $\mathcal{T}$ which is the Bethe-Salpeter equation within the ladder approximation for the impurity-boson scattering. The trap averaging is included by employing the local-density approximation (LDA) by introducing a local spectra

function $A(\Delta, \mathbf{n}_{\mathrm{LDA}}(\mathbf{r}))$ which depends on the local density $\mathbf{n}_{\mathrm{LDA}}(\mathbf{r})$. The rf pulse induced broadening is incorporated by a convolution

$$S_{\mathrm{LDA}}(\Delta, \mathbf{n}_{\mathrm{LDA}}) = \frac{1}{2\pi\sqrt{2\pi\delta\nu^2}} \int \mathrm{d}\Delta A(\Delta, \mathbf{n}_{\mathrm{LDA}}(\mathbf{r})) e^{-\Delta^2/2\delta\nu^2}. \tag{5.19}$$

Finally, we obtain a spectral function directly corresponding to the experimental observable

$$f_{\downarrow}(\Delta) = \frac{1}{N} \int \mathrm{d}^3\mathbf{r} \mathbf{n}_{\mathrm{LDA}}(\mathbf{r}) S_{\mathrm{LDA}}(\Delta, \mathbf{n}_{\mathrm{LDA}}(\mathbf{r})). \tag{5.20}$$

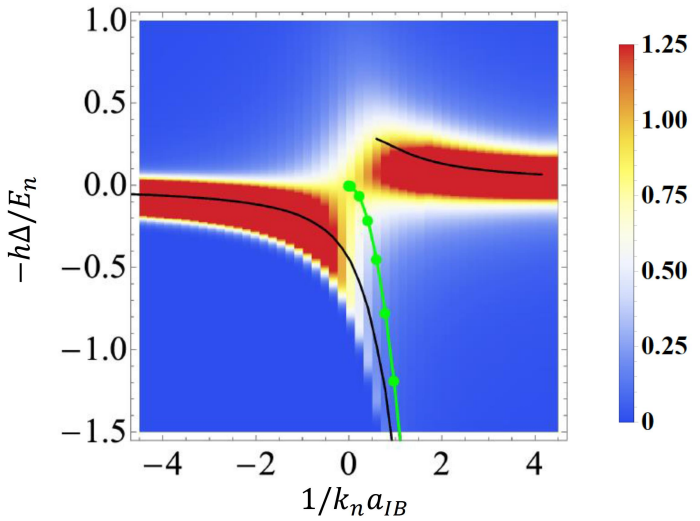

Fig. 5.7. The false colour plot of theoretical spectrum for different Δ and $1/k_n a_{\mathrm{IB}}$. The solid black line denote the position of the quasiparticle pole taking the average BEC density over the trap, while the green dotted line correspond to the dimer energy.

Figure 5.7 summarizes the theoretical spectral function versus $1/k_n a_{\mathrm{IB}}$ calculated with real experimental parameters. In stark contrast with the homogeneous density case in Fig. 5.5(b), the trap averaging and the rf pulse cause visible broadening for all $1/k_n a_{\mathrm{IB}}$. The calculation also reproduces all the main features of the experimental observation, including the increasingly larger broadening from weak to strong interactions, the extension of the attractive branch from to the a_{IB} side and the double peak in the crossover region. A detailed comparison is also presented in Fig. 5.6 by superimposing the theoretical curves to the corresponding data points for the same $1/k_n a_{\mathrm{IB}}$. Without any fitting parameters, near quantitative agreements can already be observed. However, the broadening of the spectrum

also decrease the signal amplitude, which significantly limit the signal to noise ratio of the spectrum at strong interacting regime. As we will be discussed later, the broadening line shape includes rich information about the density overlap and many-body excitations, which is coupled to the local spectra function of Bose polaron.

5.4 The energy and residue of the Bose polaron

With all the broadening mechanics, extracting the ground-state polaron energy becomes challenging. In previous works [21, 22, 69], this was done by fitting the observed spectrum with a Gaussian function. Here, however, this is seemed more complicated as the rf spectrum always contains contributions from the bare Rb transition due to the imperfect overlap between the impurity and the bath. This problem does not exist in the two-component ^{39}K experiment [69]. For the ^{40}K-^{87}Rb experiment, in which the size of the fermion impurity is much large than the BEC size, an inverse Abel transform was applied to extract signals from the overlapping part [22]. However, due to the small impurity number, the signal to noise ratio is not enough for a reliable inverse Abel transform for the current experiment.

To obtain the polaron energy, we developed an empirical spectra function

$$A(\Delta) = 2\pi Z\delta(\Delta) + 2\pi(1-Z)\Theta(\Delta)\frac{\sqrt{\Delta}}{\Delta^3+\alpha^2}\frac{3\alpha}{\pi}, \tag{5.21}$$

which includes contributions from both the polaron pole at Z in the first term and the many-body continuum in the second term. This spectral function is inspired by the spectral function at zero temperature obtained within the $\mathcal{T}$ matrix framework [171]. Here Z is the polaron residue with the local BEC density $\mathbf{n}_{\mathrm{LDA}}$, $\Theta(\Delta)$ is the Heaviside function, and α is a fitting parameter. With this spectral function, the tail of the spectrum and the density of state close to the onset of the many-body continuum are all taken into account.

Taking into account the rf pulse and trap averaging effects, we reach a line shape function

$$A(\Delta) = R(\Delta) * \int \mathrm{d}\mathbf{n}_{\mathrm{LDA}} f_{\mathrm{I}}(\mathbf{n}_{\mathrm{LDA}}) \Big\{ Z(\mathbf{n}_{\mathrm{LDA}}, Z_p)\delta(-\mathcal{E}) + (1 - Z(\mathbf{n}_{\mathrm{LDA}}, Z_p))\, 2\pi\Theta(\mathcal{E}) \frac{\sqrt{\mathcal{E}}}{\mathcal{E}^3 + \alpha^2} \frac{3\alpha}{\pi} \Big\} \tag{5.22}$$

for fitting the experimental data. Here $R(\Delta)*$ denotes the convolution with the rf envelope. $Z(\mathbf{n}_{\mathrm{LDA}}, Z_p) = 1 \Big/ \left(1 + (1/Z_p - 1)\sqrt{\mathbf{n}_{\mathrm{LDA}}/n_{\mathrm{BEC}}}\right)$ and $E(\mathbf{n}_{\mathrm{LDA}}, E_p) = E_p \mathbf{n}_{\mathrm{LDA}}/n_{\mathrm{BEC}}$ are the local polaron residue and energy, respectively [171], with E_p the peak polaron energy. $\mathcal{E} = E_{bg} - E(\mathbf{n}_{\mathrm{LDA}}, E_p) - \Delta$ is energy of the incoherent power law tail relative to the coherent part of the ground state impurity spectrum. E_{bg} is the mean-field shift of $|\uparrow\rangle$ state ^{87}Rb atoms before the rf pulse. f_{I} represents number density of ^{87}Rb as the function of surrounding BEC density n and is normalized by $\int_0^{n_{\mathrm{BEC}}} f_I(n)\mathrm{d}n/n_{\mathrm{BEC}} = 1$. It is not a continuous function since around 20% of ^{87}Rb atoms are outside of BEC.

We fit the experimental rf spectrum for both polaron branches using Eq. 5.22 with E_p, Z_p and α as the only free parameters. The fitting result the spectrum is shown in the Fig. 5.8. We can find our fit captures the experimentally observed line shape for both attractive and repulsive branch. Thus the polaron energy E_p and residue Z_p at the center of the BEC is thereby successfully obtained.

Fig. 5.9(a) shows E_p/E_n obtained from the fitting together with the theoretical results calculated with the $\mathcal{T}$ matrix framework and the variational theory [78]. For the attractive branch, good agreement between the fitting results and the theory predictions is observed from the weak interaction region up to $1/k_n a_{\mathrm{IB}} = -0.89$. Beyond this point, the deviation becomes large which should be an indication of additional physic not included in the theoretical models. A very possible source of contribution, which is neglected in both theory curves, is three-body correlations. The heteronuclear three-body parameter a_- are $\sim -11850a_0$ and $\sim -4.05 \times 10^6 a_0$ for the NaRbRb and NaNaRb systems, respectively [20]. Influences of these Efimov trimers have been addressed with variation theory including the three-body terms [85]. Another concern is the NaRb Feshbach molecule,

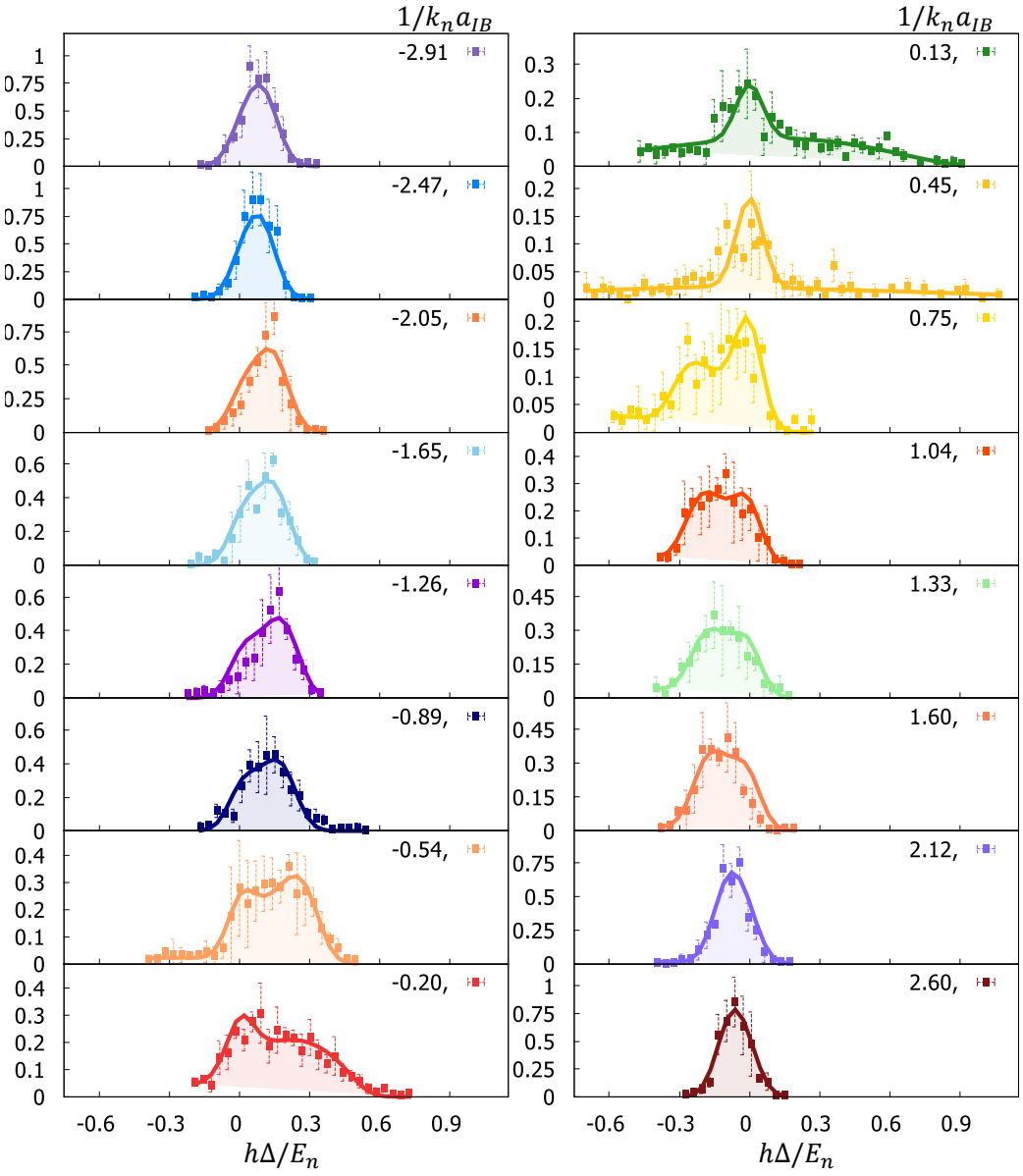

Fig. 5.8. The fit applied to polaron's rf spectrum to obtain the polaron energy and residue under different interaction strength. The solid curve shows the fitting function given by Equation. 5.22 that contains the fitting parameters E_p, Z_p and α.

which is close channel dominated at large detuning [34]. Its binding energy varies rapidly with magnetic field [34] and cannot be fully captured with the simple universal relation as used in our theories.

The repulsive branch is typically considered more complicated as it is susceptible to decay to the lower energy attractive branch. In addition, Bose

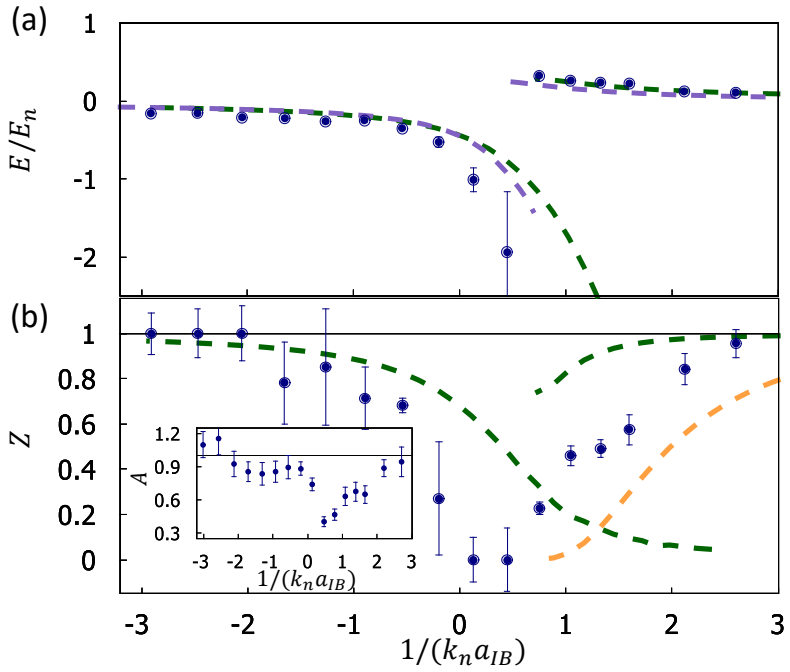

Fig. 5.9. The energy E (a) and residue Z (b) of $|\downarrow\rangle$ state impurity extracted by fitting method, which correspond to the peak BEC density n_{BEC}. The blue data points shows the fitting result versus the inverse interaction strength $1/k_n a_{\mathrm{IB}}$ and the error bar indicates the fitting error of the each lineshape. The purple dashed curve shows the prediction of $\mathcal{T}$ approximation, which is calculated with n_{BEC} and includes both the attractive and repulsive branch. The green dashed curve shows the prediction of two-body variational theory and the orange dashed curve shows the prediction of residue fitting for repulsive polaron with limited lifetime. Inset: the normalized area of the polaron spectra with respect to the bare atom transition.

gases are subject to enhanced three-body losses in the strongly interaction region. Nevertheless, as seen in Fig. 5.9(a), the fitted E_p points show excellent agreements with the two theoretical calculations. We note that the our data points for the repulsive branch cover the range of interaction strength $1/k_n a_{\mathrm{IB}} \geqslant 0.75$, i.e., no significant deviation is observed even for relatively strong interaction. We attribute this to our capability of detecting the $|\downarrow\rangle$ impurity $in\ situ$ with a fast time scale of only 30 μs after the rf pulse. The detailed time scale relevant to the polaron detection is listed in Table. 5.1, we can find that the lifetime of repulsive polaron is usually comparable to the time of our detection. Our results demonstrate that the lifetime of the repulsive polaron is long enough for the detection duration. And the fit-

ting of polaron energy center is irrelevant to the broadening from limited lifetime. However, the loss can not be neglected for the fitting of residue, which would be discussed later.

Parameters	Time scale
Thermal equilibration time ($\hbar/E_n$)	3 μs
Caculated lifetime of repulsive polaron ($1/k_n a_{IB} = 0.75$)	11 μs
Caculated lifetime of repulsive polaron ($1/k_n a_{IB} = 1.02$)	26 μs
Caculated lifetime of repulsive polaron ($1/k_n a_{IB} = 1.98$)	143 μs
Gaussian rf pulse duration	200 μs
Optical pumping pulse duration	30 μs
Absorption image pulse duration	50 μs

Tab. 5.1. Time scales relative to the rf spectrocopy of the polaron experiment.

Since our signal is the number fraction of $|\downarrow\rangle$ state atom, it is easy for us to normalize the polaron spectra with the bare atom transition. Fig. 5.9(b) shows Z_p extracted by fitting of the normalized curve together with the theoretical prediction of Z_p given by the $\mathcal{T}$ approximation and the variational theory. For the attractive branch, we can find the theoretical results consistent with the polaron residue from weak interaction region up to $1/k_n a_{\mathrm{IB}} = -1.26$. For stronger interaction, we can find that the deviation becomes large. A possible reason is the three-body recombination loss, which decrease the $|\downarrow\rangle$ state atom number in our detection. However, as shown in the inset of Fig. 5.9(b), the area of observed spectra with respect to the bare atom transition doesn't see a significant drop up to $1/k_n a_{\mathrm{IB}} = 0.13$. Thus the measurement should be correct and the spectrum is broaden by the fast decreasing of quasiparticle residue. Compared with the theoretical prediction, the lower quasiparticle residue can be addressed with the three-body terms since the residue decreases as the wave function resembles the Efimov state. Under this assumption, at around the unitary point, the residue decreases to almost zero at $1/k_n a_{\mathrm{IB}} = 0.13$.

Due to the inhomogeneous density and repulsive interaction, the impurity is possible to escape from the condensate which affects the measurements of previous experiments [22, 69]. We avoid this problem by counting all the impurities in trap with fast time scale. However, as shown in the inset of Fig. 5.9(b), starting from the weak interaction region with $1/k_n a_{\mathrm{IB}} = 2.6$, the area of the observed repulsive branch spectra still drops rapidly as the

interaction strength increases. Since the three-body loss is not significant here, the loss should be from the impurities that decay to the lower-lying states and finally leave the trap. For the two-body picture, the decay rate Γ of repulsive polaron is given by the imaginary part of the polaron energy and we can include the this rate into Rabi oscillation and calculate the corresponding polaron signal, which is proportional to the number of $|\downarrow\rangle$ state atoms. The details about the calculation is discussed in Sec. 5.5.2 and the orange dashed curve shows the prediction of the lower limit for the residue fitting of repulsive polaron with considering the limited lifetime. Finally, we can find a relatively good agreement between the theoretical prediction and fitting value.

5.5 Details about data analysis

5.5.1 The evaluation of density overlap

As shown in the insets of Fig. 5.10, in a harmonic trap, the density of ^{87}Rb and ^{23}Na clouds follow the Gaussian and parabolic distribution, respectively. The 947 nm trap gives the same gravitational sag for ^{87}Rb and ^{23}Na and the 805 nm trap decrease the size of ^{87}Rb thermal cloud in horizontal direction.

To calculate the density distribution given by Fig. 5.10, we need to consider the mean-field interaction between ^{87}Rb and ^{23}Na. The density distributions of ^{87}Rb and ^{23}Na are written as

$$\begin{aligned} n_{\mathrm{BEC}}(\rho,z) &= n_{\mathrm{BEC}}\left(1-\frac{\rho^2}{R_\rho^2}-\frac{(z-sag)^2}{R_z^2}\right), \\ n_{\mathrm{I}}(\rho,z) &= n_{\mathrm{Rb}} exp\left(-\frac{\rho^2}{2\sigma_x^2}-\frac{(z-sag)^2}{2\sigma_z^2}-\frac{E_{bg}(\rho,z)}{k_BT}\right), \end{aligned} \tag{5.23}$$

where R_z are the Tomas-Fermi radius of of BEC and σ_ρ, σ_z are the RMS width of thermal cloud. $E_{bg}(\rho,z) = 2\pi\hbar^2 a_{bg}\mathbf{n}_{\mathrm{LDA}}(\rho,z)/\mu$ is mean-field shift, which is decided by the local BEC density $\mathbf{n}_{\mathrm{LDA}}$. Here, due to the repulsive background interaction, some of the ^{87}Rb atoms are pushed away from the BEC.

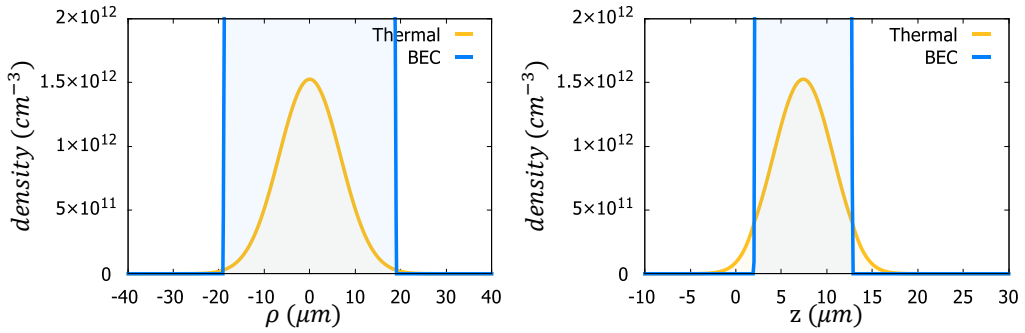

Fig. 5.10. The density distribution of ^{87}Rb thermal and ^{23}Na BEC in trap under background scattering length. (a) The density distributions in horizontal direction with $z = sag = 7.4$ μm. The peak density of BEC is $n_{\text{BEC}} = 7.1 \times 10^{13}$ cm^{-3} with $R_\rho = 19$ μm. The ^{87}Rb atoms are well trapped within the ^{23}Na BEC. (b) The density distributions in vertical direction with $\rho = 0$. The size of BEC is $R_z = 5.4$ μm, which is still not big enough for ^{87}Rb impurities.

We apply the rf pulse and intergral the spin-flipped atoms over whole trap, the fraction of spin-flipped atoms in the $|\downarrow\rangle$ state is given by

$$f_\downarrow(\Delta) = R(\nu) * \int \mathrm{d}\rho \int \mathrm{d}z \frac{n_{\mathrm{I}}(\rho, z)}{N_{Rb}} \Big\{ Z(n_{\text{LDA}}, Z_p)\delta\left(\Delta + E(n_{\text{LDA}}, E_p)\right) + (1 - Z(n_{\text{LDA}}, Z_p))2\pi\Theta(-\Delta - E(n_{\text{LDA}}, E_p)) \frac{\sqrt{-\Delta - E(n_{\text{LDA}}, E_p)}}{\left(-\Delta - E(n_{\text{LDA}}, E_p)\right)^3 + \alpha^2} \frac{3\alpha}{\pi} \Big\}. \tag{5.24}$$

where $R(\nu) = \exp(-2\nu^2/\delta\nu^2)$ is the normalized line shape of the bare atom transition, N_{Rb} is the number of ^{87}Rb. The first line shows the coherent signal from polaron pole and the second line shows the empirical spectra function that describes the incoherent many-body excitations. For simplification, here we neglect E_{bg}. By replacing the integral parameters with $\mathbf{n}_{\text{LDA}}$, we have

$$f_\downarrow(\Delta) = R(\nu) * \int \mathrm{d}\mathbf{n}_{\text{LDA}} f_I(\mathrm{n}_{\text{LDA}}) \Big\{ Z(\mathbf{n}_{\text{LDA}}, Z_p)\delta\left(-\mathcal{E}\right) + (1 - Z(\mathbf{n}_{\text{LDA}}, Z_p))2\pi\Theta(\mathcal{E}) \frac{\sqrt{\mathcal{E}}}{\mathcal{E}^3 + \alpha^2} \frac{3\alpha}{\pi} \Big\}. \tag{5.25}$$

where $\mathcal{E} = E_{bg}(\mathbf{n}_{\text{LDA}}) - E(\mathbf{n}_{\text{LDA}}, E_p) - \Delta = E(\mathbf{n}_{\text{LDA}}, E_{bg} - E_p) - \Delta$. Here, E_{bg} is the mean-field shift corresponds to the peak density n_{BEC}. This is exactly the equation 5.22.

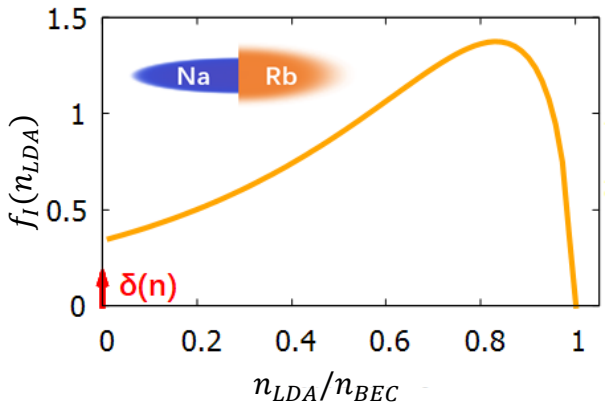

Fig. 5.11. The number density $f_I(n_{\text{LDA}})$ of $|\uparrow\rangle$ state impurities as a function of surrounding BEC density n_{LDA}. The red arrow indicates the impurities which are outside of ^{23}Na BEC. The insets shows the side view of the density distribution for ^{23}Na and ^{87}Rb atoms.

Fig. 5.11 shows the number density function $f_I(n_{\text{LDA}})$. Since some of the ^{87}Rb is outside of the ^{23}Na BEC, $f_I(n_{\text{LDA}})$ is a discontinuous piecewise function:

$$f_I(\mathbf{n}_{\text{LDA}}) = \begin{cases} \frac{N_0}{N_{Rb}}\delta(\mathbf{n}_{\text{LDA}}), & \mathbf{n}_{\text{LDA}} = 0 \\ -\frac{\mathrm{d}}{\mathrm{d}\mathbf{n}_{\text{LDA}}} \int \mathrm{d}\rho \int \mathrm{d}z \frac{n_1(\rho,z)}{N_{Rb}} \Theta(n_{\text{BEC}}(\rho,z) - \mathbf{n}_{\text{LDA}}), & \mathbf{n}_{\text{LDA}} > 0 \end{cases} \tag{5.26}$$

where N_0 is the number of ^{87}Rb atoms that are outside of BEC. Since the attractive polaron with higher BEC density tends to have lower energy, the number density distribution $f_I(\mathbf{n}_{\text{LDA}})$ is mapped to the energy density distribution $f_I(\frac{E}{E_p}\mathbf{n}_{\text{BEC}})$ for the spectrum. An intuitive understanding of the overall spectrum is that the spectrum is the convolution of $f_I(\mathbf{n}_{\text{LDA}})$ and the polaron spectra function for local density $\mathbf{n}_{\text{LDA}}$.

5.5.2 The decay of repulsive polaron

In Sec. 5.4, we found the area of repulsive polaron's spectra drops rapidly as the interaction strength increases, which is very different from the attractive brach. And our detection is fast enough to avoid the three-body

losses and the escape of impurities. According to the two-body picture, the repulsive polarons are possible to decay to lower-lying states and escape from the trap. This process can be much faster than our detection. The decreased $f_\downarrow$ do not affect the fitting of polaron energy but introduce significant error to the fitting of polaron residue.

To evaluate the influence from the loss of the $f_\downarrow = |c_\downarrow|^2$, we let $\delta = 0$ and add the loss rate Γ into the time dependent Schrödinger equation A.4:

$$i\hbar\frac{\mathrm{d}}{\mathrm{d}t}\begin{pmatrix}\widetilde{c}_\downarrow\\ \widetilde{c}_\uparrow\end{pmatrix} = \begin{pmatrix}-\frac{\Gamma}{2}i & \frac{\hbar\Omega(t)}{2}\\ \frac{\hbar\Omega(t)}{2} & 0\end{pmatrix}\begin{pmatrix}\widetilde{c}_\downarrow\\ \widetilde{c}_\uparrow\end{pmatrix}, \tag{5.27}$$

where Γ is given by the imaginary part of the polaron energy calculation. $\Omega(t)$ is the Rabi frequency of the Gaussian pulse which is given by $\Omega(t) = \Omega_0 Z e^{\frac{(t-1.75\Delta t)^2}{\Delta t^2}}$. And $\Omega_0 e^{\frac{(t-1.75\Delta t)^2}{\Delta t^2}}$ is the Rabi frequency of the bare atom transition.

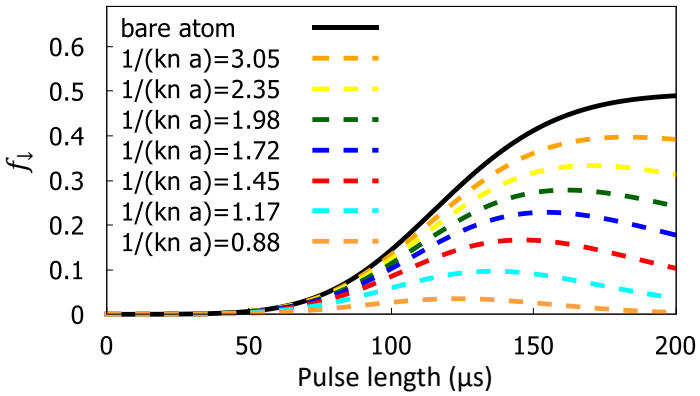

Fig. 5.12. The numerical calculation of the Rabi oscillation for the repulsive polaron under the different interaction strengths. The Rabi frequency and polaron's lifetime is given by the two-body variational theroy. $f_\downarrow$ is not normalized in this figure.

Fig. 5.12 shows the numerical simulation of the coherent Rabi oscillation for the repulsive polaron with limited lifetime. We can find the polaron signal $f_\downarrow$ is significantly decreased by the short lifetime when the interaction is strong. Since we use the bare atom transition to normalize the $f_\downarrow$ in our fitting. We normalize the $f_\downarrow$ given by Fig. 5.12 and this fraction gives the prediction of Z_p in the fitting function. The prediction is shown by the orange dashed curve in Fig. 5.9(b). However we can find that the fitting

value of Z_p is significantly larger than this prediction. That is because we assume that all the impurities will not be observed after decay, which is not true since our detection is relatively fast. Thus this prediction gives a lower limit for the fitting of residue.

5.6 Conclusion

In summary, we have observed the Bose polaron in the mixture of ^{87}Rb impurities in ^{23}Na BEC. Starting from the weak interacting state, we use injection rf spectroscopy to oberve the spectrum of the ^{87}Rb impurities. The observed spectrum shows excellent aggrement to the T-matrix calculation that includes the trap averaging effect without introducing any fitting parameters. We also use the fitting method to get rid of the trap averaging and extract the poaron energy and residue under the peak BEC density. We find that for the attractive polaron, both the energy and residue shows significant deviation for strong interaction region, which is hidden by the trap averaging spectra.

6

Thesis conclusions

In this thesis I present two studies based on the interactions offered by quantum gases. One is the spinor physics at weak interaction regime. Another is the impurity physics based on tunable interactions. Both of them are very interesting topics in many-body physics and some behavior of the Bose polaron can even be connected to the studies of few-body physics.

In Chapter 4, the manipulations of heteronuclear spinor dynamics with microwave and vector light shift were studied. We started with observation of the spin mixing dynamics within the double BEC spinor mixture of $^{87}\mathrm{Rb}|0\rangle$ and $^{23}\mathrm{Na}|0\rangle$. Due to the metastable dynamics and bad overlap between two species, we switched to thermal-BEC mixture and studied the magnetic field dependence of this heteronuclear spin mixing dynamics. In particular, we introduced microwave and vector light shifts and we have observed some difference in spin-exchange rate. Furthermore, we calculated the effective Zeeman energy introduced by the dressing fields and the spin-exchange rate at different magnetic fields matched well to the Zeeman energy calculation. This is the first quantitative study of the spinor dynamics manipulation by vector light shift, which can give much larger shift than the microwave method and also provide the local control of the spinor dynamcis.

In Chapter 5, we explored the properties of the polaron quasiparticle in a heteronuclear mixture of ^{87}Rb impurities and ^{23}Na BEC. The polaron spectrums were observed by radio frequency spectroscopy and we found near quantitative agreement between theory and experimental data without introducing any fitting parameters. To get rid of the trap averaging effect, we introduced a fitting function which includes the density information. Finally, we extracted the energy and residue of polaron near the center of BEC. Our fitting of polaron residue is the first comprehensive measurement of Bose polaron's residue. In addition, we found significant deviation of

attractive polaron's energy and residue from two-body theory's prediction at strong interaction regime. And this deviation is predicted by theory that includes the Efimov physics.

6.1 Outlook

The Bose polaron problem can be directly connected to the Fröhlich polaron which is the original polaron problem in solid state crystal. The study of Bose polaron opens up a new approach for the quantum simulation of the Fröhlich Hamitonian, which is nearly impossible to be studied by numerical calculation.

One interesting topic is to study the polaron-polaron interaction for Bose polaron problem, which may help us to understand the pairing of electrons in high temperature superconductors. Instead of the injection of spectroscopy we used in the previous experiment, we need to use the ejection spectroscopy, which can be studied with different impurity densities. First, we can apply a very fast rf pulse (several μs) to prepare the desired number of impurity atoms in BEC background. The pulse is so short and wideband that the density inhomogeneous of the surrounding BEC background will not affect the spin flip of the impurity preparation. Then we use the second pulse to do the ejection of spectroscopy. By tuning the pulse area of the first pulse, we may see the lineshape difference in the rf spectrum. This will give us a better understanding of the effective interaction between quasiparticles [163].

Based on the study of polaron-polaron interaction, another interesting topic is the bipolarons in BEC. The induced interaction mediated by BEC can form the bound state of two quasiparticles which is the origin of Cooper pairing in conventional superconductors [164]. However, this signal might be too small to be observed since the number of paired quasiparticles is very small. Some new detection methods such as fluorescent imageing should be introduced.

The coherence of spin-exchange dynamics needs low temperature and this is especially important for the metastable processes such as spin mixing

dynamics. However the two condensates are immiscible in our experiment, which gives a very bad density overlap and slow dynamics. Thus it is nearly impossible to observe repeatable coherent spin-exchange dynamics in our system.

For the better understanding of the heteronuclear spin mixing process, we may use partial-transfer absorption imaging [172] to observe each spin-exchange dynamics. Instead of averaging each set of data in time domain, we can extract the information of each set of data in frequency domain which should help us get rid of the repeatability problem. And using the vector light shift method we introduced, we may directly study the singlet-pairing process [173] in future.

Bibliography

[1] Niels Bohr. “On the Constitution of Atoms and Molecules, Part I”. In: *Philosophical Magazine* 26 (1913), pp. 1–25 (cit. on p. 1).

[2] M. Planck and M. Masius. *The Theory of Heat Radiation*. Blakiston, 1914 (cit. on p. 1).

[3] Albert Einstein. “Quantum theory of the monatomic ideal gas”. In: *Sitzungsberichte der Preussischen Akademie der Wissenschaften, Physikalisch-mathematische Klasse* (1924), pp. 261–267 (cit. on p. 1).

[4] M. H. Anderson, J. R. Ensher, M. R. Matthews, C. E. Wieman, and E. A. Cornell. “Observation of Bose-Einstein Condensation in a Dilute Atomic Vapor”. In: *Science* 269.5221 (1995), pp. 198–201. eprint: `https://science.sciencemag.org/content/269/5221/198.full.pdf` (cit. on p. 1).

[5] K. B. Davis, M. O. Mewes, M. R. Andrews, et al. “Bose-Einstein Condensation in a Gas of Sodium Atoms”. In: *Phys. Rev. Lett.* 75 (22 1995), pp. 3969–3973 (cit. on p. 1).

[6] C. C. Bradley, C. A. Sackett, J. J. Tollett, and R. G. Hulet. “Evidence of Bose-Einstein Condensation in an Atomic Gas with Attractive Interactions”. In: *Phys. Rev. Lett.* 75 (9 1995), pp. 1687–1690 (cit. on p. 1).

[7] Immanuel Bloch, Jean Dalibard, and Sylvain Nascimbène. “Quantum simulations with ultracold quantum gases”. In: *Nature Physics* 8.4 (2012), pp. 267–276 (cit. on p. 2).

[8] Manuel Endres, Hannes Bernien, Alexander Keesling, et al. “Atom-by-atom assembly of defect-free one-dimensional cold atom arrays”. In: *Science* (2016). eprint: `https://science.sciencemag.org/content/early/2016/11/02/science.aah3752.full.pdf` (cit. on p. 2).

[9] Matthew A. Norcia, Aaron W. Young, William J. Eckner, et al. “Seconds-scale coherence on an optical clock transition in a tweezer array”. In: *Science* 366.6461 (2019), pp. 93–97. eprint: `https://science.sciencemag.org/content/366/6461/93.full.pdf` (cit. on p. 2).

[10] Herman Feshbach. “Unified theory of nuclear reactions”. In: *Annals of Physics* 5.4 (1958), pp. 357 –390 (cit. on p. 2).

[11] S. Inouye, M. R. Andrews, J. Stenger, et al. “Observation of Feshbach resonances in a Bose–Einstein condensate”. In: *Nature* 392.6672 (1998), pp. 151–154 (cit. on p. 2).

[12] J. Stenger, S. Inouye, M. R. Andrews, et al. “Strongly Enhanced Inelastic Collisions in a Bose-Einstein Condensate near Feshbach Resonances”. In: *Phys. Rev. Lett.* 82 (12 1999), pp. 2422–2425 (cit. on pp. 2, 13).

[13] Cheng Chin, Rudolf Grimm, Paul Julienne, and Eite Tiesinga. “Feshbach resonances in ultracold gases”. In: *Rev. Mod. Phys.* 82 (2 2010), pp. 1225–1286 (cit. on pp. 2, 10).

[14] G. Barontini, C. Weber, F. Rabatti, et al. “Observation of Heteronuclear Atomic Efimov Resonances”. In: *Phys. Rev. Lett.* 103 (4 2009), p. 043201 (cit. on p. 2).

[15] Ruth S. Bloom, Ming-Guang Hu, Tyler D. Cumby, and Deborah S. Jin. “Tests of Universal Three-Body Physics in an Ultracold Bose-Fermi Mixture”. In: *Phys. Rev. Lett.* 111 (10 2013), p. 105301 (cit. on p. 2).

[16] Shih-Kuang Tung, Karina Jiménez-García, Jacob Johansen, Colin V. Parker, and Cheng Chin. “Geometric Scaling of Efimov States in a $^{6}\mathrm{Li}-^{133}\mathrm{Cs}$ Mixture”. In: *Phys. Rev. Lett.* 113 (24 2014), p. 240402 (cit. on p. 2).

[17] R. Pires, J. Ulmanis, S. Häfner, et al. “Observation of Efimov Resonances in a Mixture with Extreme Mass Imbalance”. In: *Phys. Rev. Lett.* 112 (25 2014), p. 250404 (cit. on p. 2).

[18] R. A. W. Maier, M. Eisele, E. Tiemann, and C. Zimmermann. “Efimov Resonance and Three-Body Parameter in a Lithium-Rubidium Mixture”. In: *Phys. Rev. Lett.* 115 (4 2015), p. 043201 (cit. on p. 2).

[19] Sébastien Laurent, Matthieu Pierce, Marion Delehaye, et al. “Connecting Few-Body Inelastic Decay to Quantum Correlations in a Many-Body System: A Weakly Coupled Impurity in a Resonant Fermi Gas”. In: *Phys. Rev. Lett.* 118 (10 2017), p. 103403 (cit. on p. 2).

[20] Fudong Wang, Xin Ye, Mingyang Guo, D. Blume, and Dajun Wang. “Observation of resonant scattering between ultracold heteronuclear Feshbach molecules”. In: *Phys. Rev. A* 100 (4 2019), p. 042706 (cit. on pp. 2, 14, 121).

[21] C. Kohstall, M. Zaccanti, M. Jag, et al. “Metastability and coherence of repulsive polarons in a strongly interacting Fermi mixture”. In: *Nature* 485.7400 (2012), pp. 615–618 (cit. on pp. 2, 3, 120).

[22] Ming-Guang Hu, Michael J. Van de Graaff, Dhruv Kedar, et al. “Bose Polarons in the Strongly Interacting Regime”. In: *Phys. Rev. Lett.* 117 (5 2016), p. 055301 (cit. on pp. 2, 3, 113, 120, 124).

[23] Zoe Z. Yan, Yiqi Ni, Carsten Robens, and Martin W. Zwierlein. “Bose polarons near quantum criticality”. In: *Science* 368.6487 (2020), pp. 190–194. eprint: `https://science.sciencemag.org/content/368/6487/190.full.pdf` (cit. on pp. 2, 3, 114).

[24] Xiaoke Li, Bing Zhu, Xiaodong He, et al. “Coherent Heteronuclear Spin Dynamics in an Ultracold Spinor Mixture”. In: *Phys. Rev. Lett.* 114 (25 2015), p. 255301 (cit. on pp. 2, 15, 82, 90, 92, 93, 95).

[25] Alexander Mil, Torsten V. Zache, Apoorva Hegde, et al. “A scalable realization of local U(1) gauge invariance in cold atomic mixtures”. In: *Science* 367.6482 (2020), pp. 1128–1130 (cit. on p. 2).

[26] C. D’Errico, A. Burchianti, M. Prevedelli, et al. “Observation of quantum droplets in a heteronuclear bosonic mixture”. In: *Phys. Rev. Research* 1 (3 2019), p. 033155 (cit. on p. 2).

[27] S. B. Papp and C. E. Wieman. “Observation of Heteronuclear Feshbach Molecules from a $^{85}\mathrm{Rb} - {}^{87}\mathrm{Rb}$ Gas”. In: *Phys. Rev. Lett.* 97 (18 2006), p. 180404 (cit. on p. 2).

[28] C. Klempt, T. Henninger, O. Topic, et al. “Radio-frequency association of heteronuclear Feshbach molecules”. In: *Phys. Rev. A* 78 (6 2008), p. 061602 (cit. on p. 2).

[29] K.-K. Ni, S. Ospelkaus, M. H. G. de Miranda, et al. “A High Phase-Space-Density Gas of Polar Molecules”. In: *Science* 322.5899 (2008), pp. 231–235 (cit. on p. 2).

[30] S. Ospelkaus, A. Pe’er, K. K. Ni, et al. “Efficient state transfer in an ultracold dense gas of heteronuclear molecules”. In: *Nature Physics* 4.8 (2008), pp. 622–626 (cit. on p. 2).

[31] Myoung-Sun Heo, Tout T. Wang, Caleb A. Christensen, et al. “Formation of ultracold fermionic NaLi Feshbach molecules”. In: *Phys. Rev. A* 86 (2 2012), p. 021602 (cit. on p. 2).

[32] Tetsu Takekoshi, Markus Debatin, Raffael Rameshan, et al. “Towards the production of ultracold ground-state RbCs molecules: Feshbach resonances, weakly bound states, and the coupled-channel model”. In: *Phys. Rev. A* 85 (3 2012), p. 032506 (cit. on p. 2).

[33] Cheng-Hsun Wu, Jee Woo Park, Peyman Ahmadi, Sebastian Will, and Martin W. Zwierlein. “Ultracold Fermionic Feshbach Molecules of $^{23}\mathrm{Na}^{40}\mathbf{K}$”. In: *Phys. Rev. Lett.* 109 (8 2012), p. 085301 (cit. on p. 2).

[34] Fudong Wang, Xiaodong He, Xiaoke Li, et al. “Formation of ultracold NaRb Feshbach molecules”. In: *New Journal of Physics* 17.3 (2015), p. 035003 (cit. on pp. 2, 9, 122).

[35] Jee Woo Park, Sebastian A. Will, and Martin W. Zwierlein. “Ultracold Dipolar Gas of Fermionic $^{23}\mathrm{Na}^{40}\mathrm{K}$ Molecules in Their Absolute Ground State”. In: *Phys. Rev. Lett.* 114 (20 2015), p. 205302 (cit. on p. 2).

[36] Mingyang Guo, Bing Zhu, Bo Lu, et al. “Creation of an Ultracold Gas of Ground-State Dipolar $^{23}\mathrm{Na}^{87}\mathrm{Rb}$ Molecules”. In: *Phys. Rev. Lett.* 116 (20 2016), p. 205303 (cit. on pp. 2, 15).

[37] Timur M. Rvachov, Hyungmok Son, Ariel T. Sommer, et al. “Long-Lived Ultracold Molecules with Electric and Magnetic Dipole Moments”. In: *Phys. Rev. Lett.* 119 (14 2017), p. 143001 (cit. on p. 2).

[38] Kai K. Voges, Philipp Gersema, Torsten Hartmann, et al. “Formation of ultracold weakly bound dimers of bosonic $^{23}\mathrm{Na}^{39}\mathrm{K}$”. In: *Phys. Rev. A* 101 (4 2020), p. 042704 (cit. on p. 2).

[39] Xing-Can Yao, Hao-Ze Chen, Yu-Ping Wu, et al. “Observation of Coupled Vortex Lattices in a Mass-Imbalance Bose and Fermi Superfluid Mixture”. In: *Phys. Rev. Lett.* 117 (14 2016), p. 145301 (cit. on p. 2).

[40] S. B. Papp, J. M. Pino, and C. E. Wieman. “Tunable Miscibility in a Dual-Species Bose-Einstein Condensate”. In: *Phys. Rev. Lett.* 101 (4 2008), p. 040402 (cit. on p. 2).

[41] D. J. McCarron, H. W. Cho, D. L. Jenkin, M. P. Köppinger, and S. L. Cornish. “Dual-species Bose-Einstein condensate of $^{87}\mathrm{Rb}$ and $^{133}\mathrm{Cs}$”. In: *Phys. Rev. A* 84 (1 2011), p. 011603 (cit. on p. 2).

[42] Fudong Wang, Xiaoke Li, Dezhi Xiong, and Dajun Wang. “A double species ^{23}Na and ^{87}Rb Bose–Einstein condensate with tunable miscibility via an interspecies Feshbach resonance”. In: *Journal of Physics B: Atomic, Molecular and Optical Physics* 49.1 (2015), p. 015302 (cit. on pp. 2, 26, 32, 94).

[43] K L Lee, N B Jørgensen, L J Wacker, et al. “Time-of-flight expansion of binary Bose–Einstein condensates at finite temperature”. In: *New Journal of Physics* 20.5 (2018), p. 053004 (cit. on p. 2).

[44] Tin-Lun Ho. “Spinor Bose Condensates in Optical Traps”. In: *Phys. Rev. Lett.* 81 (4 1998), pp. 742–745 (cit. on pp. 2, 73).

[45] J. Stenger, S. Inouye, D. M. Stamper-Kurn, et al. “Spin domains in ground-state Bose–Einstein condensates”. In: *Nature* 396 (Nov. 1998), p. 345 (cit. on pp. 2, 73).

[46] Yuki Kawaguchi and Masahito Ueda. “Spinor Bose–Einstein condensates”. In: *Physics Reports* 520.5 (2012). Spinor Bose–Einstein condensates, pp. 253 –381 (cit. on pp. 2, 73).

[47] T. Kuwamoto, K. Araki, T. Eno, and T. Hirano. “Magnetic field dependence of the dynamics of $^{87}\mathrm{Rb}$ spin-2 Bose-Einstein condensates”. In: *Phys. Rev. A* 69 (6 2004), p. 063604 (cit. on p. 2).

[48] H. Schmaljohann, M. Erhard, J. Kronjäger, et al. “Dynamics of $F = 2$ Spinor Bose-Einstein Condensates”. In: *Phys. Rev. Lett.* 92 (4 2004), p. 040402 (cit. on p. 2).

[49] M.-S. Chang, C. D. Hamley, M. D. Barrett, et al. “Observation of Spinor Dynamics in Optically Trapped $^{87}\mathrm{Rb}$ Bose-Einstein Condensates”. In: *Phys. Rev. Lett.* 92 (14 2004), p. 140403 (cit. on pp. 2, 73, 93).

[50] Ming-Shien Chang, Qishu Qin, Wenxian Zhang, Li You, and Michael S. Chapman. “Coherent spinor dynamics in a spin-1 Bose condensate”. In: *Nat. Phys.* 1.2 (Nov. 2005), pp. 111–116 (cit. on pp. 2, 73).

[51] Artur Widera, Fabrice Gerbier, Simon Fölling, et al. “Coherent Collisional Spin Dynamics in Optical Lattices”. In: *Phys. Rev. Lett.* 95 (19 2005), p. 190405 (cit. on pp. 2, 73).

[52] J. Kronjäger, C. Becker, P. Navez, K. Bongs, and K. Sengstock. “Magnetically Tuned Spin Dynamics Resonance”. In: *Phys. Rev. Lett.* 97 (11 2006), p. 110404 (cit. on pp. 2, 73).

[53] Fabrice Gerbier, Artur Widera, Simon Fölling, Olaf Mandel, and Immanuel Bloch. “Resonant control of spin dynamics in ultracold quantum gases by microwave dressing”. In: *Phys. Rev. A* 73 (4 2006), p. 041602 (cit. on pp. 2, 73, 87).

[54] A. T. Black, E. Gomez, L. D. Turner, S. Jung, and P. D. Lett. “Spinor Dynamics in an Antiferromagnetic Spin-1 Condensate”. In: *Phys. Rev. Lett.* 99 (7 2007), p. 070403 (cit. on pp. 2, 73).

[55] C. Klempt, O. Topic, G. Gebreyesus, et al. “Multiresonant Spinor Dynamics in a Bose-Einstein Condensate”. In: *Phys. Rev. Lett.* 103 (19 2009), p. 195302 (cit. on p. 2).

[56] E. M. Bookjans, A. Vinit, and C. Raman. “Quantum Phase Transition in an Antiferromagnetic Spinor Bose-Einstein Condensate”. In: *Phys. Rev. Lett.* 107 (19 2011), p. 195306 (cit. on pp. 2, 73, 93).

[57] H. K. Pechkis, J. P. Wrubel, A. Schwettmann, et al. “Spinor Dynamics in an Antiferromagnetic Spin-1 Thermal Bose Gas”. In: *Phys. Rev. Lett.* 111 (2 2013), p. 025301 (cit. on pp. 2, 73).

[58] Xiaodong He, Bing Zhu, Xiaoke Li, et al. “Coherent spin-mixing dynamics in thermal $^{87}\mathrm{Rb}$ spin-1 and spin-2 gases”. In: *Phys. Rev. A* 91 (3 2015), p. 033635 (cit. on pp. 2, 73).

[59] Eva M. Bookjans, Christopher D. Hamley, and Michael S. Chapman. “Strong Quantum Spin Correlations Observed in Atomic Spin Mixing”. In: *Phys. Rev. Lett.* 107 (21 2011), p. 210406 (cit. on p. 3).

[60] C. D. Hamley, C. S. Gerving, T. M. Hoang, E. M. Bookjans, and M. S. Chapman. “Spin-nematic squeezed vacuum in a quantum gas”. In: *Nat. Phys.* 8 (Feb. 2012), p. 305 (cit. on p. 3).

[61] T. M. Hoang, C. S. Gerving, B. J. Land, et al. “Dynamic Stabilization of a Quantum Many-Body Spin System”. In: *Phys. Rev. Lett.* 111 (9 2013), p. 090403 (cit. on p. 3).

[62] T. M. Hoang, M. Anquez, B. A. Robbins, et al. “Parametric excitation and squeezing in a many-body spinor condensate”. In: *Nat. Commun.* 7 (Apr. 2016), p. 11233 (cit. on p. 3).

[63] Xin-Yu Luo, Yi-Quan Zou, Ling-Na Wu, et al. “Deterministic entanglement generation from driving through quantum phase transitions”. In: *Science* 355.6325 (2017), pp. 620–623 (cit. on p. 3).

[64] M. Anquez, B. A. Robbins, H. M Bharath, et al. “Quantum Kibble-Zurek Mechanism in a Spin-1 Bose-Einstein Condensate”. In: *Phys. Rev. Lett.* 116 (15 2016), p. 155301 (cit. on p. 3).

[65] L.-Y. Qiu, H.-Y. Liang, Y.-B. Yang, et al. “Observation of generalized Kibble-Zurek mechanism across a first-order quantum phase transition in a spinor condensate”. In: *Science Advances* 6.21 (2020). eprint: `https://advances.sciencemag.org/content/6/21/eaba7292.full.pdf` (cit. on pp. 3, 73).

[66] LD Landau. “On the motion of electrons in a crystal lattice”. In: *Phys. Z. Sowjetunion* 3 (1933), p. 664 (cit. on pp. 3, 101).

[67] SI Pekar. “Autolocalization of the electron in an inertially polarizable dielectric medium”. In: *Zh. Eksp. Teor. Fiz* 16 (1946), p. 335 (cit. on pp. 3, 101).

[68] LD Landau and SI Pekar. “Effective mass of a polaron”. In: *Zh. Eksp. Teor. Fiz* 18.5 (1948), pp. 419–423 (cit. on pp. 3, 101).

[69] Nils B. Jørgensen, Lars Wacker, Kristoffer T. Skalmstang, et al. “Observation of Attractive and Repulsive Polarons in a Bose-Einstein Condensate”. In: *Phys. Rev. Lett.* 117 (5 2016), p. 055302 (cit. on pp. 3, 114, 120, 124).

[70] G. E. Astrakharchik and L. P. Pitaevskii. “Motion of a heavy impurity through a Bose-Einstein condensate”. In: *Phys. Rev. A* 70 (1 2004), p. 013608 (cit. on pp. 3, 101).

[71] F. M. Cucchietti and E. Timmermans. “Strong-Coupling Polarons in Dilute Gas Bose-Einstein Condensates”. In: *Phys. Rev. Lett.* 96 (21 2006), p. 210401 (cit. on pp. 3, 101).

[72] Ryan M. Kalas and D. Blume. “Interaction-induced localization of an impurity in a trapped Bose-Einstein condensate”. In: *Phys. Rev. A* 73 (4 2006), p. 043608 (cit. on pp. 3, 101).

[73] Krzysztof Sacha and Eddy Timmermans. “Self-localized impurities embedded in a one-dimensional Bose-Einstein condensate and their quantum fluctuations”. In: *Phys. Rev. A* 73 (6 2006), p. 063604 (cit. on pp. 3, 101).

[74] M. Bruderer, W. Bao, and D. Jaksch. “Self-trapping of impurities in Bose-Einstein condensates: Strong attractive and repulsive coupling”. In: *EPL (Europhysics Letters)* 82.3 (2008), p. 30004 (cit. on pp. 3, 101).

[75] Huang Bei-Bing and Wan Shao-Long. “Polaron in Bose–Einstein–Condensation System”. In: *Chinese Physics Letters* 26.8 (2009), p. 080302 (cit. on pp. 3, 101).

[76] J. Tempere, W. Casteels, M. K. Oberthaler, et al. “Feynman path-integral treatment of the BEC-impurity polaron”. In: *Phys. Rev. B* 80 (18 2009), p. 184504 (cit. on pp. 3, 101).

[77] Steffen Patrick Rath and Richard Schmidt. “Field-theoretical study of the Bose polaron”. In: *Phys. Rev. A* 88 (5 2013), p. 053632 (cit. on pp. 3, 101, 104, 105, 109).

[78] Weiran Li and S. Das Sarma. "Variational study of polarons in Bose-Einstein condensates". In: *Phys. Rev. A* 90 (1 2014), p. 013618 (cit. on pp. 3, 101, 103, 104, 109, 121).

[79] Aditya Shashi, Fabian Grusdt, Dmitry A. Abanin, and Eugene Demler. "Radio-frequency spectroscopy of polarons in ultracold Bose gases". In: *Phys. Rev. A* 89 (5 2014), p. 053617 (cit. on pp. 3, 101, 118).

[80] A. G. Volosniev, H.-W. Hammer, and N. T. Zinner. "Real-time dynamics of an impurity in an ideal Bose gas in a trap". In: *Phys. Rev. A* 92 (2 2015), p. 023623 (cit. on pp. 3, 101).

[81] F. Grusdt, Y. E. Shchadilova, A. N. Rubtsov, and E. Demler. "Renormalization group approach to the Fröhlich polaron model: application to impurity-BEC problem". In: *Scientific Reports* 5 (July 2015), 12124 EP – (cit. on pp. 3, 101, 104).

[82] André Schirotzek, Cheng-Hsun Wu, Ariel Sommer, and Martin W. Zwierlein. "Observation of Fermi Polarons in a Tunable Fermi Liquid of Ultracold Atoms". In: *Phys. Rev. Lett.* 102 (23 2009), p. 230402 (cit. on p. 3).

[83] Marco Koschorreck, Daniel Pertot, Enrico Vogt, et al. "Attractive and repulsive Fermi polarons in two dimensions". In: *Nature* 485.7400 (2012), pp. 619–622 (cit. on p. 3).

[84] F. Scazza, G. Valtolina, P. Massignan, et al. "Repulsive Fermi Polarons in a Resonant Mixture of Ultracold ^{6}Li Atoms". In: *Phys. Rev. Lett.* 118 (8 2017), p. 083602 (cit. on p. 3).

[85] Jesper Levinsen, Meera M. Parish, and Georg M. Bruun. "Impurity in a Bose-Einstein Condensate and the Efimov Effect". In: *Phys. Rev. Lett.* 115 (12 2015), p. 125302 (cit. on pp. 3, 14, 101, 104, 111, 121).

[86] L. A. Peña Ardila and S. Giorgini. "Bose polaron problem: Effect of mass imbalance on binding energy". In: *Phys. Rev. A* 94 (6 2016), p. 063640 (cit. on pp. 3, 104).

[87] Mingyuan Sun, Hui Zhai, and Xiaoling Cui. "Visualizing the Efimov Correlation in Bose Polarons". In: *Phys. Rev. Lett.* 119 (1 2017), p. 013401 (cit. on pp. 3, 14).

[88] Franco Dalfovo, Stefano Giorgini, Lev P. Pitaevskii, and Sandro Stringari. "Theory of Bose-Einstein condensation in trapped gases". In: *Rev. Mod. Phys.* 71 (3 1999), pp. 463–512 (cit. on p. 7).

[89] Lev Davidovich Landau and Evgenii Mikhailovich Lifshitz. *Quantum mechanics: non-relativistic theory*. Vol. 3. Elsevier, 2013 (cit. on p. 8).

[90] S. Knoop, T. Schuster, R. Scelle, et al. “Feshbach spectroscopy and analysis of the interaction potentials of ultracold sodium”. In: *Phys. Rev. A* 83 (4 2011), p. 042704 (cit. on pp. 9, 109).

[91] E. G. M. van Kempen, S. J. J. M. F. Kokkelmans, D. J. Heinzen, and B. J. Verhaar. “Interisotope Determination of Ultracold Rubidium Interactions from Three High-Precision Experiments”. In: *Phys. Rev. Lett.* 88 (9 2002), p. 093201 (cit. on pp. 9, 109).

[92] Fudong Wang, Dezhi Xiong, Xiaoke Li, Dajun Wang, and Eberhard Tiemann. “Observation of Feshbach resonances between ultracold Na and Rb atoms”. In: *Phys. Rev. A* 87 (5 2013), p. 050702 (cit. on pp. 9, 115).

[93] C. A. Regal, M. Greiner, and D. S. Jin. “Observation of Resonance Condensation of Fermionic Atom Pairs”. In: *Phys. Rev. Lett.* 92 (4 2004), p. 040403 (cit. on p. 10).

[94] Christopher J Pethick and Henrik Smith. *Bose–Einstein condensation in dilute gases*. Cambridge university press, 2008 (cit. on pp. 10, 103).

[95] Christopher J Foot et al. *Atomic physics*. Vol. 7. Oxford University Press, 2005 (cit. on pp. 10, 18).

[96] Wolfgang Ketterle, Dallin S Durfee, and DM Stamper-Kurn. “Making, probing and understanding Bose-Einstein condensates”. In: *arXiv preprint cond-mat/9904034* (1999) (cit. on p. 10).

[97] Wolfgang Ketterle. “Experimental studies of Bose-Einstein condensation”. In: *Phys. Today* 52.12 (1999), pp. 30–35 (cit. on p. 10).

[98] Ph W Courteille, Vanderlei Salvador Bagnato, and VI Yukalov. “Bose-Einstein condensation of trapped atomic gases”. In: *arXiv preprint cond-mat/0109421* (2001) (cit. on p. 10).

[99] Vanderlei Salvador Bagnato, Dimitri J Frantzeskakis, Panagiotis G Kevrekidis, Boris A Malomed, and D Mihalache. “Bose-Einstein condensation: Twenty years after”. In: *arXiv preprint arXiv:1502.06328* (2015) (cit. on p. 10).

[100] E. P. Gross. “Structure of a quantized vortex in boson systems”. In: *Il Nuovo Cimento (1955-1965)* 20.3 (1961), pp. 454–477 (cit. on p. 10).

[101] Tsin D Lee, Kerson Huang, and Chen N Yang. “Eigenvalues and eigenfunctions of a Bose system of hard spheres and its low-temperature properties”. In: *Physical Review* 106.6 (1957), p. 1135 (cit. on p. 12).

[102] Nir Navon, Swann Piatecki, Kenneth Günter, et al. “Dynamics and Thermodynamics of the Low-Temperature Strongly Interacting Bose Gas”. In: *Phys. Rev. Lett.* 107 (13 2011), p. 135301 (cit. on p. 12).

[103] D. S. Petrov. “Quantum Mechanical Stabilization of a Collapsing Bose-Bose Mixture”. In: *Phys. Rev. Lett.* 115 (15 2015), p. 155302 (cit. on p. 12).

[104] Igor Ferrier-Barbut, Holger Kadau, Matthias Schmitt, Matthias Wenzel, and Tilman Pfau. “Observation of Quantum Droplets in a Strongly Dipolar Bose Gas”. In: *Phys. Rev. Lett.* 116 (21 2016), p. 215301 (cit. on p. 12).

[105] CR Cabrera, L Tanzi, J Sanz, et al. “Quantum liquid droplets in a mixture of Bose-Einstein condensates”. In: *Science* 359.6373 (2018), pp. 301–304 (cit. on p. 12).

[106] P. Cheiney, C. R. Cabrera, J. Sanz, et al. “Bright Soliton to Quantum Droplet Transition in a Mixture of Bose-Einstein Condensates”. In: *Phys. Rev. Lett.* 120 (13 2018), p. 135301 (cit. on p. 12).

[107] G. Semeghini, G. Ferioli, L. Masi, et al. “Self-Bound Quantum Droplets of Atomic Mixtures in Free Space”. In: *Phys. Rev. Lett.* 120 (23 2018), p. 235301 (cit. on p. 12).

[108] P. O. Fedichev, M. W. Reynolds, and G. V. Shlyapnikov. “Three-Body Recombination of Ultracold Atoms to a Weakly Bound s Level”. In: *Phys. Rev. Lett.* 77 (14 1996), pp. 2921–2924 (cit. on p. 13).

[109] B. D. Esry, Chris H. Greene, and James P. Burke. “Recombination of Three Atoms in the Ultracold Limit”. In: *Phys. Rev. Lett.* 83 (9 1999), pp. 1751–1754 (cit. on p. 13).

[110] S. L. Cornish, N. R. Claussen, J. L. Roberts, E. A. Cornell, and C. E. Wieman. “Stable $^{85}\mathrm{Rb}$ Bose-Einstein Condensates with Widely Tunable Interactions”. In: *Phys. Rev. Lett.* 85 (9 2000), pp. 1795–1798 (cit. on p. 13).

[111] Tino Weber, Jens Herbig, Michael Mark, Hanns-Christoph Nägerl, and Rudolf Grimm. “Three-Body Recombination at Large Scattering Lengths in an Ultracold Atomic Gas”. In: *Phys. Rev. Lett.* 91 (12 2003), p. 123201 (cit. on p. 13).

[112] V Efimov. “Weakly-bound states of three resonantly-interacting particles”. In: *Sov. J. Nucl. Phys* 12.589 (1971), p. 101 (cit. on p. 14).

[113] Pascal Naidon and Shimpei Endo. “Efimov physics: a review”. In: *Reports on Progress in Physics* 80.5 (2017), p. 056001 (cit. on p. 14).

[114] Eric Braaten and H.-W. Hammer. “Efimov physics in cold atoms”. In: *Annals of Physics* 322.1 (2007). January Special Issue 2007, pp. 120 –163 (cit. on p. 14).

[115] T. Kraemer, M. Mark, P. Waldburger, et al. “Evidence for Efimov quantum states in an ultracold gas of caesium atoms”. In: *Nature* 440.7082 (2006), pp. 315–318 (cit. on p. 14).

[116] Ruth S. Bloom, Ming-Guang Hu, Tyler D. Cumby, and Deborah S. Jin. “Tests of Universal Three-Body Physics in an Ultracold Bose-Fermi Mixture”. In: *Phys. Rev. Lett.* 111 (10 2013), p. 105301 (cit. on p. 14).

[117] Dezhi Xiong, Fudong Wang, Xiaoke Li, Ting-Fai Lam, and Dajun Wang. “Production of a rubidium Bose-Einstein condensate in a hybrid trap with light induced atom desorption”. In: 2013 (cit. on p. 15).

[118] Xiaoke Li. “Coherent Heteronuclear Spin Dynamics in an Ultracold Spinor Mixture”. PhD thesis. The Chinese University of Hong Kong, 2015 (cit. on p. 15).

[119] Bing Zhu. “Studies of Polar Molecules and Spinor Gases with an Ultracold Mixture of Na and Rb Atoms”. PhD thesis. The Chinese University of Hong Kong, 2016 (cit. on pp. 15, 21).

[120] Fudong Wang. “Studies of an Ultracold Bose-Bose Mixture with Tunable Interspecies Interactions”. PhD thesis. The Chinese University of Hong Kong, 2016 (cit. on p. 15).

[121] Ettore Majorana. “Atomi orientati in campo magnetico variabile”. In: *Il Nuovo Cimento (1924-1942)* 9.2 (1932), pp. 43–50 (cit. on p. 16).

[122] Michael A Joffe, Wolfgang Ketterle, Alex Martin, and David E Pritchard. “Transverse cooling and deflection of an atomic beam inside a Zeeman slower”. In: *JOSA B* 10.12 (1993), pp. 2257–2262 (cit. on p. 19).

[123] K. Dieckmann, R. J. C. Spreeuw, M. Weidemüller, and J. T. M. Walraven. “Two-dimensional magneto-optical trap as a source of slow atoms”. In: *Phys. Rev. A* 58 (5 1998), pp. 3891–3895 (cit. on p. 19).

[124] C. Klempt, T. van Zoest, T. Henninger, et al. “Ultraviolet light-induced atom desorption for large rubidium and potassium magneto-optical traps”. In: *Phys. Rev. A* 73 (1 2006), p. 013410 (cit. on p. 19).

[125] D. S. Barker, E. B. Norrgard, J. Scherschligt, J. A. Fedchak, and S. Eckel. “Light-induced atomic desorption of lithium”. In: *Phys. Rev. A* 98 (4 2018), p. 043412 (cit. on p. 19).

[126] M. A. Kristensen, M. B. Christensen, M. Gajdacz, et al. “Observation of Atom Number Fluctuations in a Bose-Einstein Condensate”. In: *Phys. Rev. Lett.* 122 (16 2019), p. 163601 (cit. on p. 22).

[127] Rudolf Grimm, Matthias Weidemüller, and Yuri Ovchinnikov. “Optical Dipole Traps for Neutral Atoms”. In: *Adv. At. Mol. Opt. Phys.* 42 (Dec. 2000), p. 95 (cit. on pp. 25, 32).

[128] M. S. Safronova, Bindiya Arora, and Charles W. Clark. “Frequency-dependent polarizabilities of alkali-metal atoms from ultraviolet through infrared spectral regions”. In: *Phys. Rev. A* 73 (2 2006), p. 022505 (cit. on pp. 28, 32, 114).

[129] Mancini Ron. *Op Amps For Everyone*. Design Reference. Texas Instruments, 2002 (cit. on p. 38).

[130] John Wright. *Don’t Be Fooled by Voltage Reference Long-Term Drift and Hysteresis*. Design Note 229. Linear Technology, 2000 (cit. on p. 38).

[131] Jim Williams, J. Brubaker, P. Copley, J. Guerrero, and F. Oprescu. *A Standards Lab Grade 20-Bit DAC with 0.1ppm/°C Drift*. Application Note 86. Linear Technology, 2001 (cit. on p. 39).

[132] Vishay. *Audio Noise Reduction Through the Use of Bulk Metal® Foil Resistors-“Hear the Difference”*. Application Notes 49414. Vishay, 2005 (cit. on p. 39).

[133] Frank Seifert. *Resistor Current Noise Measurements*. Technical report. LIGO, 2009 (cit. on p. 39).

[134] Philip Makotyn. “Experimental studies of a degenerate unitary Bose gas”. PhD thesis. University of Colorado, 2014 (cit. on p. 46).

[135] Allan Cabiluna, YaFei Lv, ZhiPing Hu, and Wonsuk Choi. *Practical Considerations of Trench MOSFET Stability when Operating in Linear Mode*. Application Note 4161. Fairchild Semiconductor, 2013 (cit. on p. 48).

[136] J. Schoiswohl. *Linear Mode Operation and Safe Operating Diagram of PowerMOSFETs*. Application Note AP99007. Infineon Technologies, 2017 (cit. on p. 48).

[137] Daniel A Steck. *Rubidium 87 D line data*. 2001 (cit. on p. 49).

[138] W Alan Davis and Krishna Kumar Agarwal. *Radio frequency circuit design*. Wiley Online Library, 2001 (cit. on p. 51).

[139] Gerald L Hall, G Woodward, CL Hutchinson, et al. “The ARRL Antenna Book, The American Radio Relay League”. In: *Inc. Newington CT* (1984), pp. 2–20 (cit. on p. 51).

[140] Ming-Guang Hu. “Bose polarons and rotating gases in an ultracold Bose-Fermi gas mixture of ^{40}K and ^{87}Rb atoms”. PhD thesis. University of Colorado, 2015 (cit. on p. 61).

[141] Eva M. Bookjans. “RELATIVE NUMBER SQUEEZING IN A SPIN-1 BOSE-EINSTEIN CONDENSATE”. PhD thesis. Georgia Institute of Technology, 2010 (cit. on p. 61).

[142] Pieter-Tjerk de Boer. *Digital noise reduction*. Tech. rep. University of Twente, 2017 (cit. on p. 66).

[143] G. Reinaudi, T. Lahaye, Z. Wang, and D. Guéry-Odelin. “Strong saturation absorption imaging of dense clouds of ultracold atoms”. In: *Opt. Lett.* 32.21 (2007), pp. 3143–3145 (cit. on p. 69).

[144] Tetsuo Ohmi and Kazushige Machida. “Bose-Einstein Condensation with Internal Degrees of Freedom in Alkali Atom Gases”. In: *J. Phys. Soc. Jpn.* 67.6 (1998), pp. 1822–1825 (cit. on p. 73).

[145] C. K. Law, H. Pu, and N. P. Bigelow. “Quantum Spins Mixing in Spinor Bose-Einstein Condensates”. In: *Phys. Rev. Lett.* 81 (24 1998), pp. 5257–5261 (cit. on p. 73).

[146] Wenxian Zhang, D. L. Zhou, M.-S. Chang, M. S. Chapman, and L. You. “Coherent spin mixing dynamics in a spin-1 atomic condensate”. In: *Phys. Rev. A* 72 (1 2005), p. 013602 (cit. on p. 73).

[147] Dan M. Stamper-Kurn and Masahito Ueda. “Spinor Bose gases: Symmetries, magnetism, and quantum dynamics”. In: *Rev. Mod. Phys.* 85 (3 2013), pp. 1191–1244 (cit. on p. 73).

[148] L. Zhao, J. Jiang, T. Tang, M. Webb, and Y. Liu. “Dynamics in spinor condensates tuned by a microwave dressing field”. In: *Phys. Rev. A* 89 (2 2014), p. 023608 (cit. on pp. 73, 87).

[149] S. R. Leslie, J. Guzman, M. Vengalattore, et al. “Amplification of fluctuations in a spinor Bose-Einstein condensate”. In: *Phys. Rev. A* 79 (4 2009), p. 043631 (cit. on p. 73).

[150] Yixiao Huang, Wei Zhong, Zhe Sun, and Zheng-Da Hu. “Phase diagram and spin mixing dynamics in spinor condensates with a microwave dressing field”. In: *Scientific Reports* 5 (Sept. 2015), 14464 EP – (cit. on p. 73).

[151] Z. F. Xu, Yunbo Zhang, and L. You. “Binary mixture of spinor atomic Bose-Einstein condensates”. In: *Phys. Rev. A* 79 (2 2009), p. 023613 (cit. on pp. 82, 85).

[152] Z. F. Xu, D. J. Wang, and L. You. “Quantum spin mixing in a binary mixture of spin-1 atomic condensates”. In: *Phys. Rev. A* 86 (1 2012), p. 013632 (cit. on pp. 82, 85).

[153] Daniel A. Steck. *Quantum and Atom Optics*. 2007 (cit. on p. 88).

[154] L. S. Leslie, A. Hansen, K. C. Wright, B. M. Deutsch, and N. P. Bigelow. "Creation and Detection of Skyrmions in a Bose-Einstein Condensate". In: *Phys. Rev. Lett.* 103 (25 2009), p. 250401 (cit. on p. 99).

[155] Jae-yoon Choi, Woo Jin Kwon, and Yong-il Shin. "Observation of Topologically Stable 2D Skyrmions in an Antiferromagnetic Spinor Bose-Einstein Condensate". In: *Phys. Rev. Lett.* 108 (3 2012), p. 035301 (cit. on p. 99).

[156] H. Fröhlich, H. Pelzer, and S. Zienau. "Properties of slow electrons in polar materials". In: *The London, Edinburgh, and Dublin Philosophical Magazine and Journal of Science* 41.314 (1950), pp. 221–242. eprint: https://doi.org/10.1080/14786445008521794 (cit. on p. 101).

[157] H. Fröhlich. "Electrons in lattice fields". In: *Advances in Physics* 3.11 (1954), pp. 325–361. eprint: https://doi.org/10.1080/00018735400101213 (cit. on pp. 101, 102).

[158] Rasmus Søgaard Christensen, Jesper Levinsen, and Georg M. Bruun. "Quasiparticle Properties of a Mobile Impurity in a Bose-Einstein Condensate". In: *Phys. Rev. Lett.* 115 (16 2015), p. 160401 (cit. on pp. 101, 104, 105).

[159] L. A. Peña Ardila and S. Giorgini. "Impurity in a Bose-Einstein condensate: Study of the attractive and repulsive branch using quantum Monte Carlo methods". In: *Phys. Rev. A* 92 (3 2015), p. 033612 (cit. on pp. 101, 104).

[160] L. Parisi and S. Giorgini. "Quantum Monte Carlo study of the Bose-polaron problem in a one-dimensional gas with contact interactions". In: *Phys. Rev. A* 95 (2 2017), p. 023619 (cit. on pp. 101, 104).

[161] Jesper Levinsen, Meera M. Parish, Rasmus S. Christensen, Jan J. Arlt, and Georg M. Bruun. "Finite-temperature behavior of the Bose polaron". In: *Phys. Rev. A* 96 (6 2017), p. 063622 (cit. on p. 101).

[162] F. Grusdt, R. Schmidt, Y. E. Shchadilova, and E. Demler. "Strong-coupling Bose polarons in a Bose-Einstein condensate". In: *Phys. Rev. A* 96 (1 2017), p. 013607 (cit. on pp. 101, 104, 112).

[163] A. Camacho-Guardian and Georg M. Bruun. "Landau Effective Interaction between Quasiparticles in a Bose-Einstein Condensate". In: *Phys. Rev. X* 8 (3 2018), p. 031042 (cit. on pp. 101, 132).

[164] A. Camacho-Guardian, L. A. Peña Ardila, T. Pohl, and G. M. Bruun. "Bipolarons in a Bose-Einstein Condensate". In: *Phys. Rev. Lett.* 121 (1 2018), p. 013401 (cit. on pp. 101, 132).

[165] Nils-Eric Guenther, Pietro Massignan, Maciej Lewenstein, and Georg M. Bruun. “Bose Polarons at Finite Temperature and Strong Coupling”. In: *Phys. Rev. Lett.* 120 (5 2018), p. 050405 (cit. on p. 101).

[166] Shuhei M. Yoshida, Shimpei Endo, Jesper Levinsen, and Meera M. Parish. “Universality of an Impurity in a Bose-Einstein Condensate”. In: *Phys. Rev. X* 8 (1 2018), p. 011024 (cit. on pp. 101, 104).

[167] Bernard Field, Jesper Levinsen, and Meera M. Parish. “Fate of the Bose polaron at finite temperature”. In: *Phys. Rev. A* 101 (1 2020), p. 013623 (cit. on p. 101).

[168] David Dzsotjan, Richard Schmidt, and Michael Fleischhauer. “Dynamical Variational Approach to Bose Polarons at Finite Temperatures”. In: *Phys. Rev. Lett.* 124 (22 2020), p. 223401 (cit. on pp. 101, 104).

[169] F. Chevy. “Universal phase diagram of a strongly interacting Fermi gas with unbalanced spin populations”. In: *Phys. Rev. A* 74 (6 2006), p. 063628 (cit. on p. 104).

[170] Alexander L Fetter and John Dirk Walecka. *Quantum theory of many-particle systems*. Courier Corporation, 2012 (cit. on p. 105).

[171] L. A. Peña Ardila, N. B. Jørgensen, T. Pohl, et al. “Analyzing a Bose polaron across resonant interactions”. In: *Phys. Rev. A* 99 (6 2019), p. 063607 (cit. on pp. 120, 121).

[172] Anand Ramanathan, Sérgio R. Muniz, Kevin C. Wright, et al. “Partial-transfer absorption imaging: A versatile technique for optimal imaging of ultracold gases”. In: *Review of Scientific Instruments* 83.8 (2012), p. 083119. eprint: https://doi.org/10.1063/1.4747163 (cit. on p. 133).

[173] Jianwen Jie, Yonghong Yu, Dajun Wang, and Peng Zhang. *Laser Control of Singlet-Pairing Process in an Ultracold Spinor Mixture*. 2020. arXiv: 2008.10071 [cond-mat.quant-gas] (cit. on p. 133).

A

Appendix

A.1 The spin rotations and rf spectroscopy of non-interacting atoms

For the magnetic field around 347 G, the transition frequencies between different sublevels are well separated by the quadratic Zeeman energy. Thus can use the two-level Hamiltonian to describe the system. For ^{87}Rb impurities, the rf photon's frequency is typically around $2\pi\times230$ MHz, which shows negligible momentum. For the momentum-conserving transitions, we let H_0 be the noninteracting Hamiltonian and H_{rf} be the interaction between atom and AC magnetic field in horizontal direction. For simplification, we define the AC magnetic field in x axis. Thus we have

$$\begin{aligned} H &= H_0 + H_{rf} \\ &= H_0 + 2\hbar\Omega(t)F_x \\ &= \begin{pmatrix} E+\hbar\omega_0 & 0 \\ 0 & E \end{pmatrix} + \begin{pmatrix} 0 & \hbar\Omega(t)cos(\omega t) \\ \hbar\Omega(t)cos(\omega t) & 0 \end{pmatrix}, \end{aligned} \tag{A.1}$$

where we define the initial state $|I\rangle = (0,1)^T$ with energy E, final state $|F\rangle = (1,0)^T$ with energy $E+\hbar\omega_0$, $\hbar\omega_0$ is the Zeeman splitting between two sublevels under B_0 and $\Omega(t)$ is the Rabi frequency. The time-dependent Schrödinger equation is

$$i\hbar\frac{\mathrm{d}}{\mathrm{d}t}\begin{pmatrix} c_F \\ c_I \end{pmatrix} = \begin{pmatrix} E+\hbar\omega_0 & \hbar\Omega(t)cos(\omega t) \\ \hbar\Omega(t)cos(\omega t) & E \end{pmatrix}\begin{pmatrix} c_F \\ c_I \end{pmatrix}. \tag{A.2}$$

Under the unitary transformation

$$\begin{pmatrix} \widetilde{c_F} \\ \widetilde{c_I} \end{pmatrix} = \hat{U}\begin{pmatrix} c_F \\ c_I \end{pmatrix} = \begin{pmatrix} e^{-i(E+\hbar\omega_0)t} & 0 \\ 0 & e^{-iEt} \end{pmatrix}\begin{pmatrix} c_F \\ c_I \end{pmatrix}, \tag{A.3}$$

which gives $\widetilde{H} = U^{\dagger}(H - i\hbar\frac{\partial}{\partial t})U$. After the rotating-wave approximation, the system becomes

$$i\hbar\frac{\mathrm{d}}{\mathrm{d}t}\begin{pmatrix}\widetilde{c_F}\\ \widetilde{c_I}\end{pmatrix} = \frac{\hbar\Omega(t)}{2}\begin{pmatrix}0 & e^{-i\delta t}\\ e^{i\delta t} & 0\end{pmatrix}\begin{pmatrix}\widetilde{c_F}\\ \widetilde{c_I}\end{pmatrix}, \tag{A.4}$$

where $\delta = \omega - \omega_0$ is the detuning from resonance frequency.

We first talk about the case for $\delta = 0$, which means the rf frequency is in resonance with the Zeeman energy splitting of two energy levels.

For the square pulse $\Omega(t) = \Omega_0(\Theta(0) - \Theta(t))$ the fractional population of spin-flipped atoms in the final state $|F\rangle$ is

$$P_F = |\widetilde{c_F}|^2 = sin^2\left(\frac{\Omega_0 t}{2}\right). \tag{A.5}$$

For the gaussian pulse we define $\Omega(t) = \Omega_0 e^{\frac{(t-1.75\Delta t)^2}{\Delta t^2}}$ and the pulse is applied during $t = 0$ and $3.5\Delta t$. At $t = 3.5\Delta t$, the fractional population of spin-flipped atoms in the final state $|F\rangle$ is

$$\begin{aligned} P_F &= |\widetilde{c_F}|^2 \\ &= sin^2\left(\frac{\Omega_0\sqrt{\pi}Erf(1.75)t/3.5}{2}\right) \\ &\approx sin^2(0.2498\Omega_0 t) \end{aligned} \tag{A.6}$$

For our setting with applying the rf from 0 to $3.5\Delta t$, the effective Rabi frequency for the gaussian pulse is around one half of Ω_0, which corresponds to the peak power of rf. To get the line shape of the gaussian pulse we used in polaron experiment, we do the Fourier transformation of $\Omega(t)$, which has

$$\begin{aligned} \Omega(2\pi\nu) &= \int_{-\infty}^{\infty}\Omega_0 e^{\frac{(t-1.75\Delta t)^2}{\Delta t^2}}e^{i2\pi\nu t}\mathrm{d}t \\ &= \sqrt{\pi}\Omega_0\Delta t e^{i1.75\Delta t(2\pi\nu)}e^{\frac{(\Delta t(2\pi\nu))^2}{4}} \\ &\propto e^{\frac{\nu^2}{\Delta\nu^2}}, \end{aligned} \tag{A.7}$$

where $\Delta\nu \equiv 1/(\pi\Delta t)$ is the $1/e$ width. For small pulse area, the lineshape is $R(\nu) \propto \Omega(2\pi\nu)^2 \propto e^{\frac{2\nu^2}{\Delta\nu^2}}$. If we go back to the original Hamitonian, the lineshape should be

$$R(\nu - \nu_0) \propto e^{\frac{2(\nu-\nu_0)^2}{\Delta\nu^2}}, \tag{A.8}$$

where $\nu_0 = \omega_0/2\pi$ is the resonance frequency under magnetic field B_0.

The square pulse is already discussed in secion 3.5.1, and the lineshape should be

$$R(\nu - \nu_0) \propto sinc^2\left[\pi T(\nu - \nu_0)\right], \tag{A.9}$$

where T is defined as the pulse duration.

A.2 The rapid adiabatic passage

We can also flip the spin by sweeping the detuning δ across the resonance. We solve the equation A.4 for $\widetilde{c_F}$ leads

$$\frac{\mathrm{d}^2}{\mathrm{d}t^2}\widetilde{c_F} + i\left(\delta(t) + t\frac{\mathrm{d}}{\mathrm{d}t}\delta(t)\right)\frac{\mathrm{d}}{\mathrm{d}t}\widetilde{c_F} + \left(\frac{\Omega}{2}\right)^2\widetilde{c_F} = 0 \tag{A.10}$$

with initial conditions $\widetilde{c_F} = 0$ and $\mathrm{d}\widetilde{c_F}/\mathrm{d}t = \Omega/2$. If we linearly sweep the detuning with considering $\delta(t) = \alpha t$ and change the variable by the transform $\widetilde{c_F} = e^{-i\alpha t^2}y$. The equation becomes

$$\frac{\mathrm{d}^2}{\mathrm{d}t^2}y + \left[\left(\frac{\Omega}{2}\right)^2 + \alpha^2 t^2\right]y = 0, \tag{A.11}$$

which is known as the Weber differential equations. At $t \to \infty$, the explicit solution that called Landau-Zener formula is

$$P_F = |\widetilde{c_F}|^2 = 1 - e^{-\frac{\pi\Omega^2}{2\alpha}}, \tag{A.12}$$

which means during the frequency sweep we should keep $\dot{\omega} \ll \Omega^2$. Otherwise the efficiency of the spin flip will be affected.

We can also understand this result by the classical model. With introducing the oscillating magnetic field, the energy of eigenlevels of the Hamiltonian of equation A.1 changes from $(\hbar\delta, 0)^T$ to $\left(\hbar\frac{\delta+\sqrt{\delta^2+2\Omega^2}}{2}, \hbar\frac{\delta-\sqrt{\delta^2+2\Omega^2}}{2}\right)^T$, which means the degeneracy of two levels is split by Rabi frequency at $\delta = 0$ point. And if we tune the detuning across the resonance, there will be an avoid crossing and the spin state is fliped from one to another. However the speed of spin flipping should be controlled well below the Rabi frequency. Otherwise the spin of the atom can not follow the sweep of the detuning. This limitation is most critical for the frequency close to resonance, which gives

$$\frac{\mathrm{d}\omega}{\mathrm{d}t}/\Omega \ll \Omega, \tag{A.13}$$

which is same as the requirement given by the Landau-Zener formula. For the rapid adiabatic passage in our experiment, we use 10 ms to linearly sweep the rf frequency across the resonance with a speed around $2\pi \times 40$ MHz/s, which is much smaller than $\Omega^2 = (2\pi \times 20\ \mathrm{kHz})^2$.

A.3 Circuit diagrams

In this section, I include the new designs for the electrical components of our machine. Most of them are relevant to the experiment in my thesis. All the designs and drawings are created by myself.

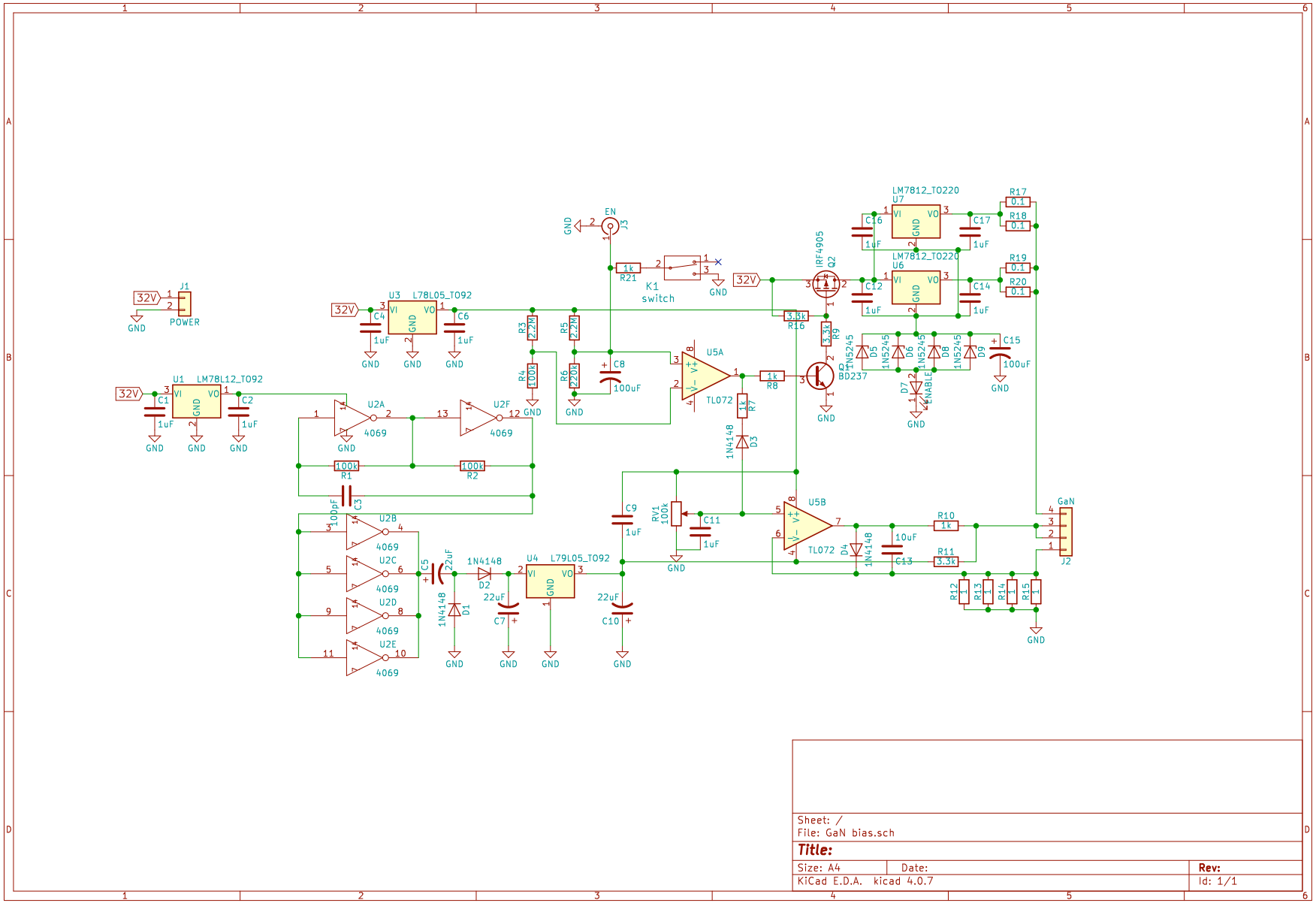

Fig. A.1. GaN bias controller.

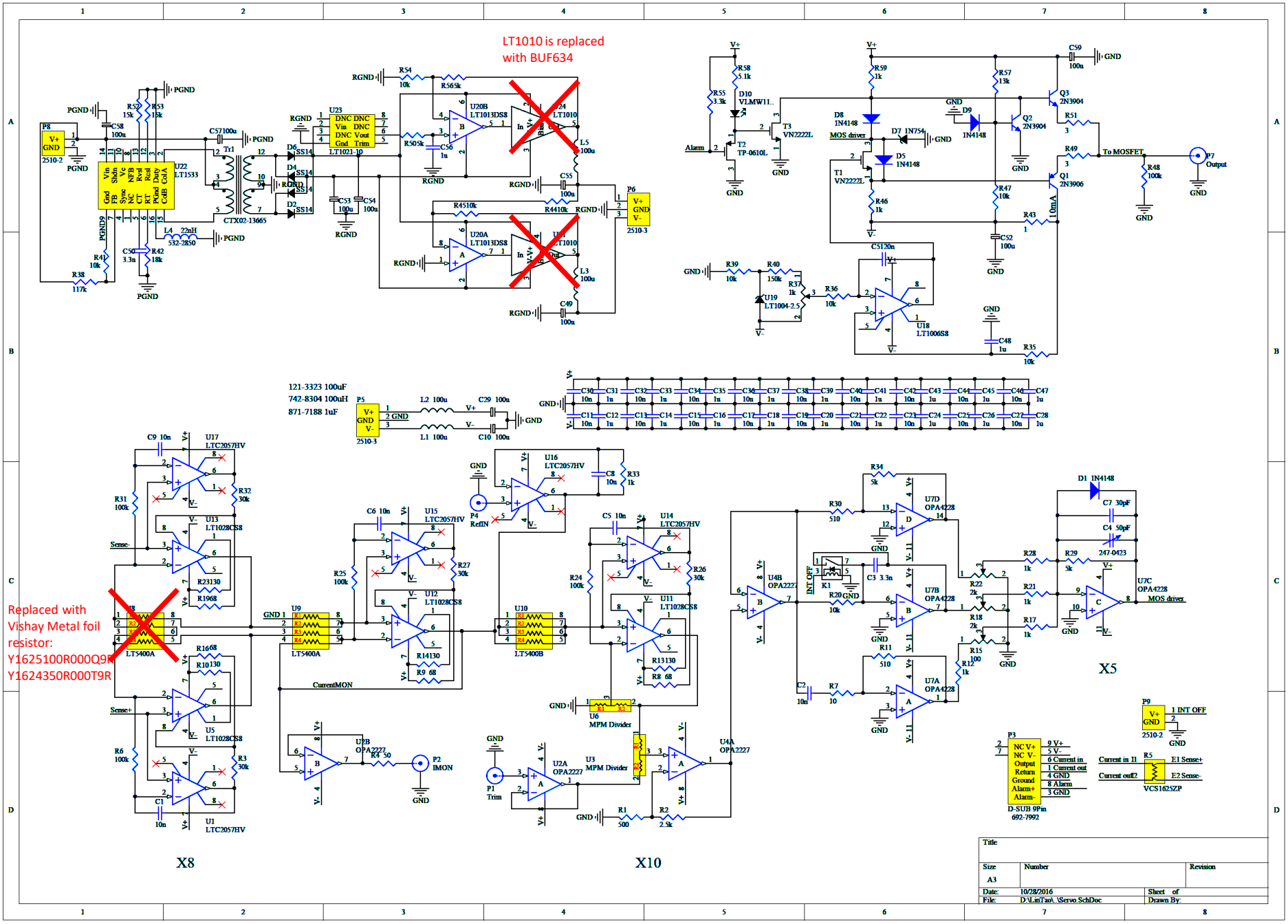

Fig. A.2. Magnetic field servo (for MOSFET) and isolated low noise switched-mode power supply.

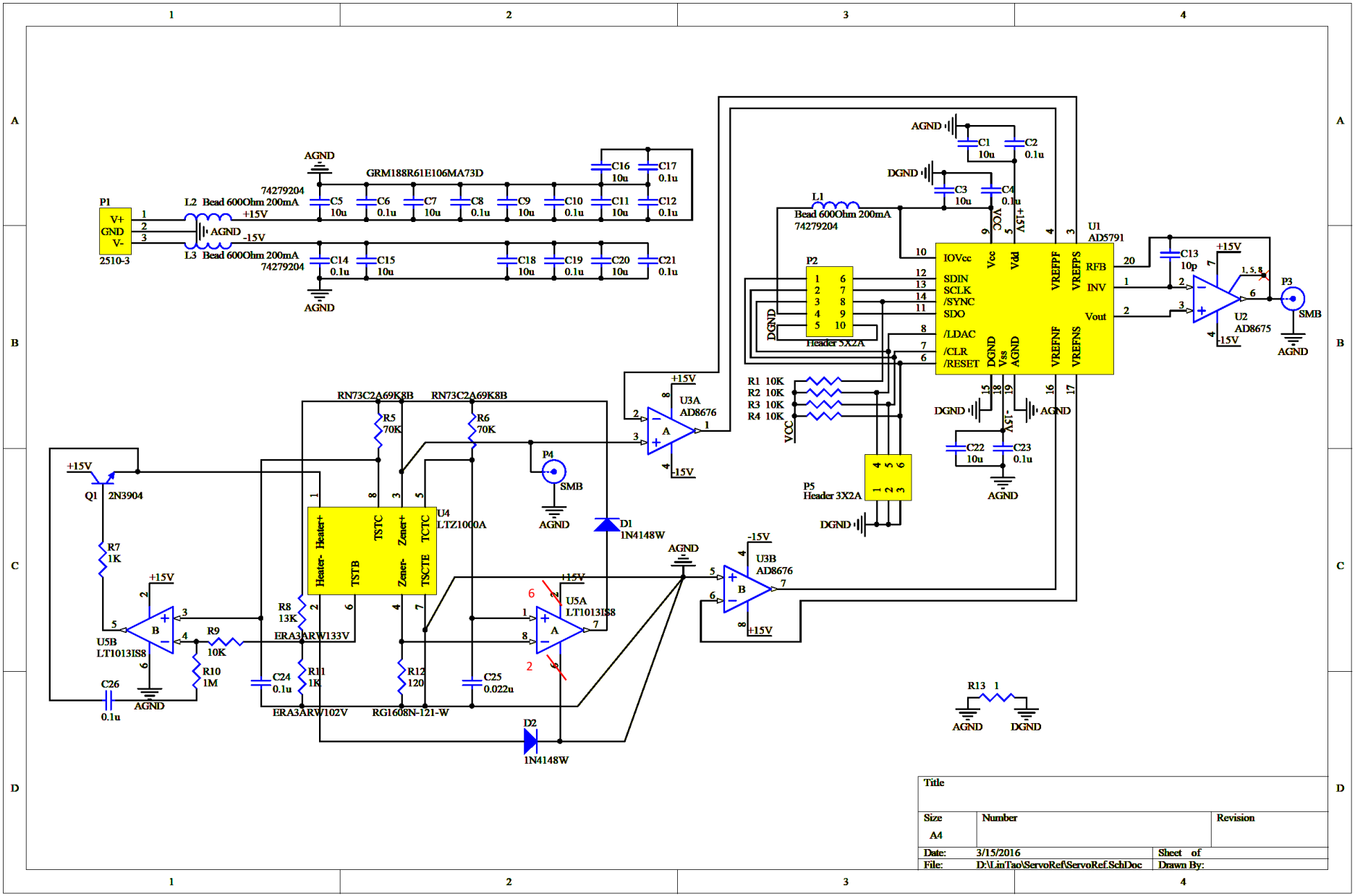

Fig. A.3. Voltage reference and DAC with 1 ppm stability and resolution.

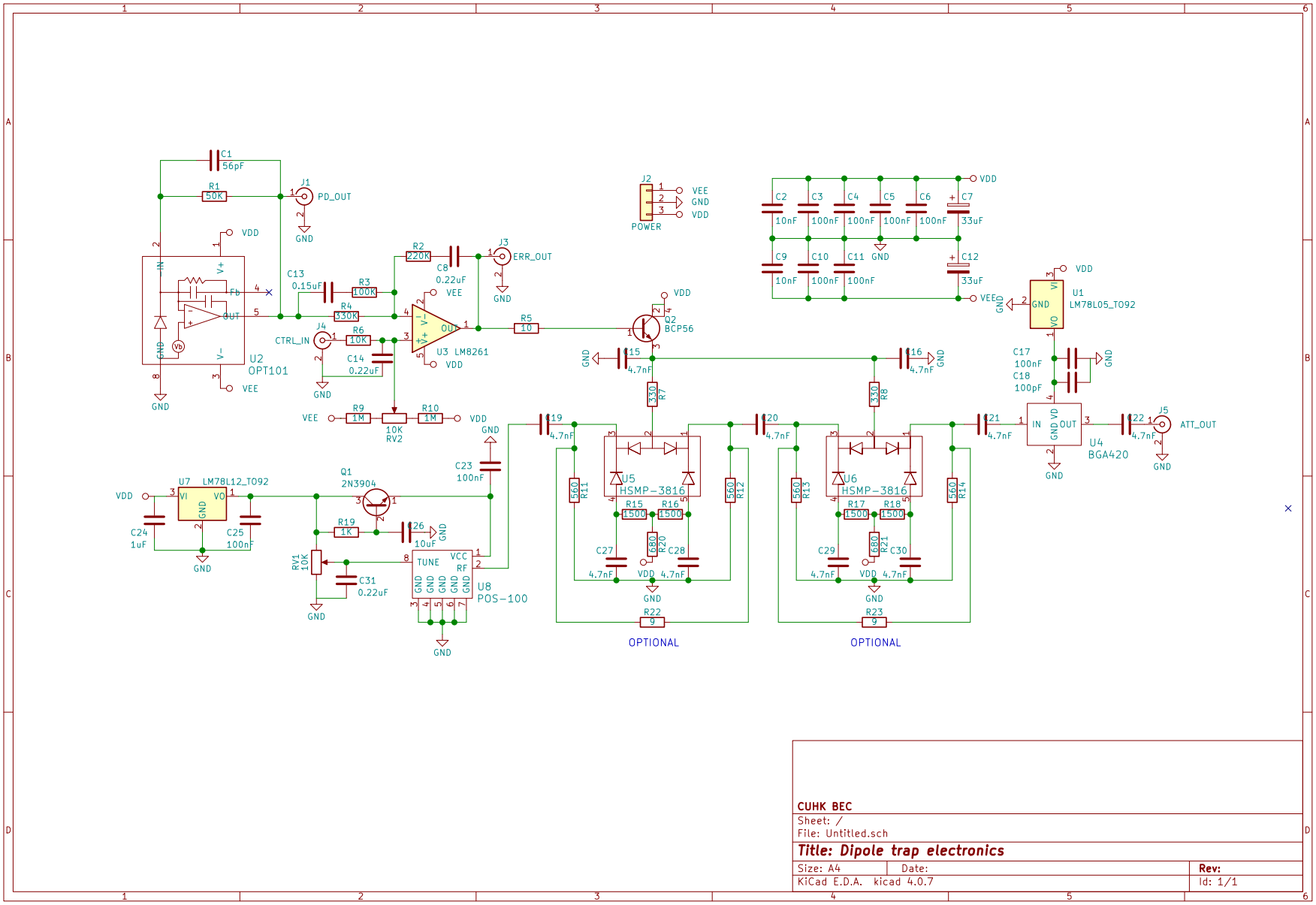

Fig. A.4. Dipole trap power controller with intergrated PD, VCO and variable attenuator.

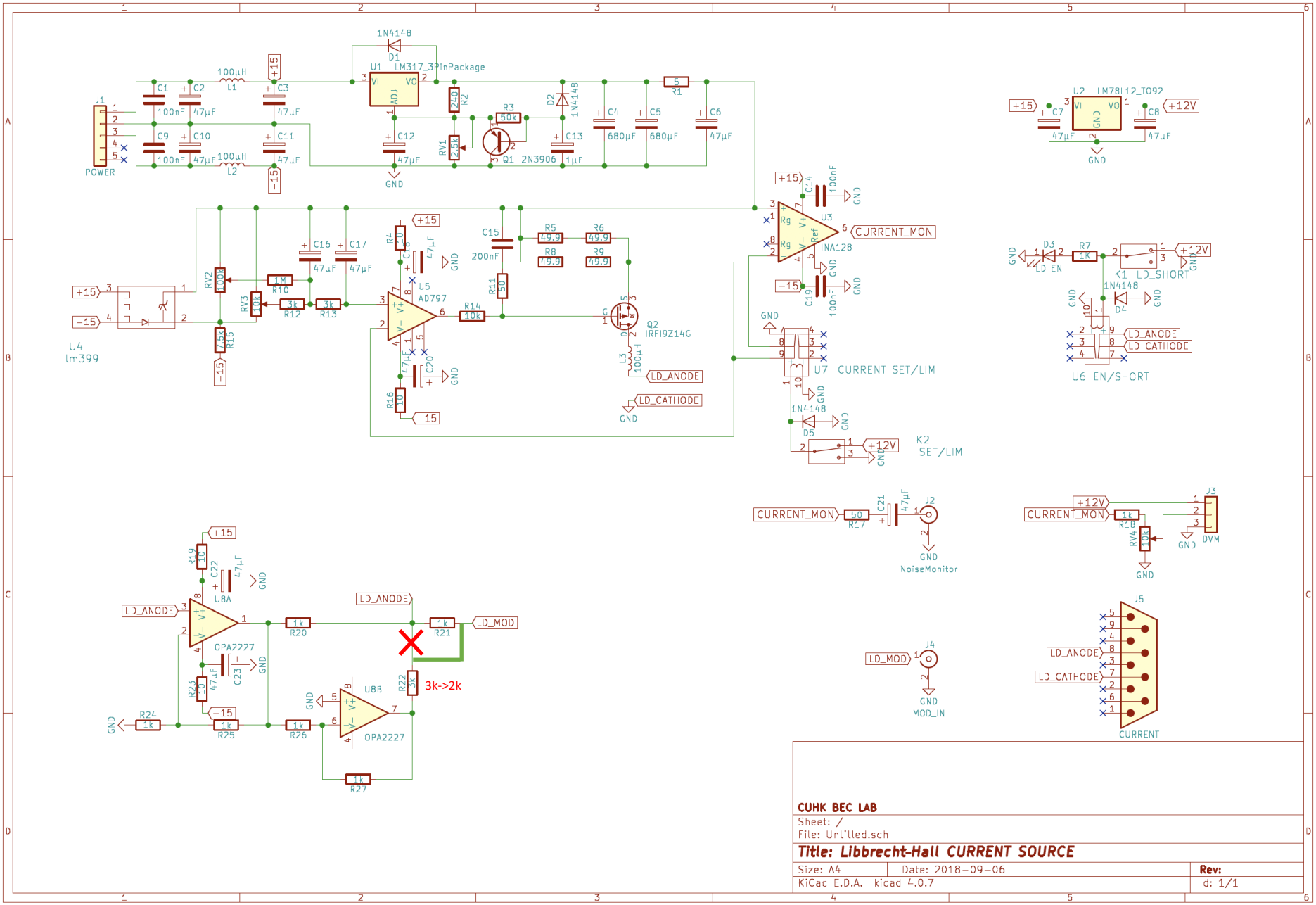

Fig. A.5. Libbrecht-Hall current source for DFB/DBR laser diode.

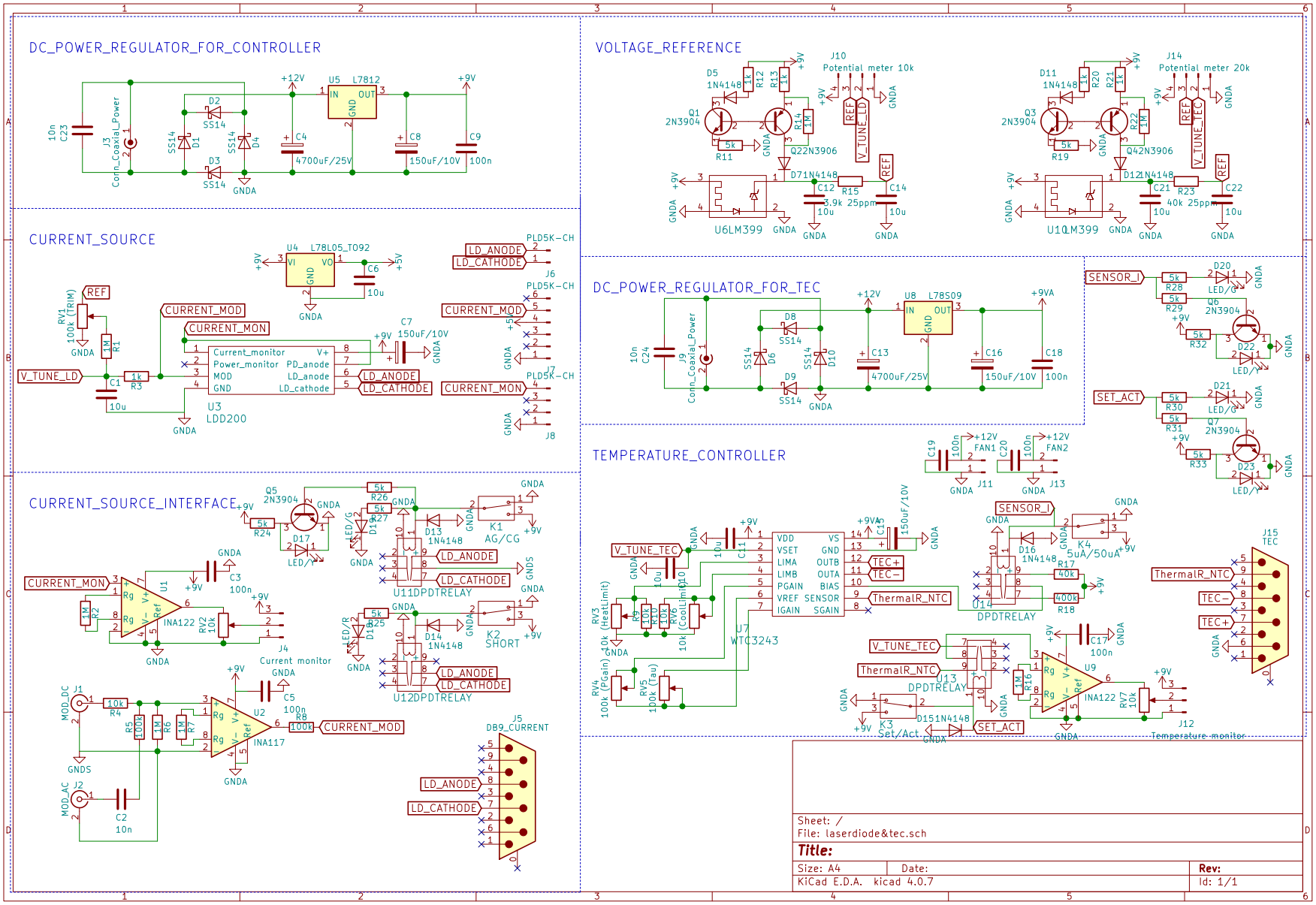

Fig. A.6. Current source and TEC controller for general ECDL.

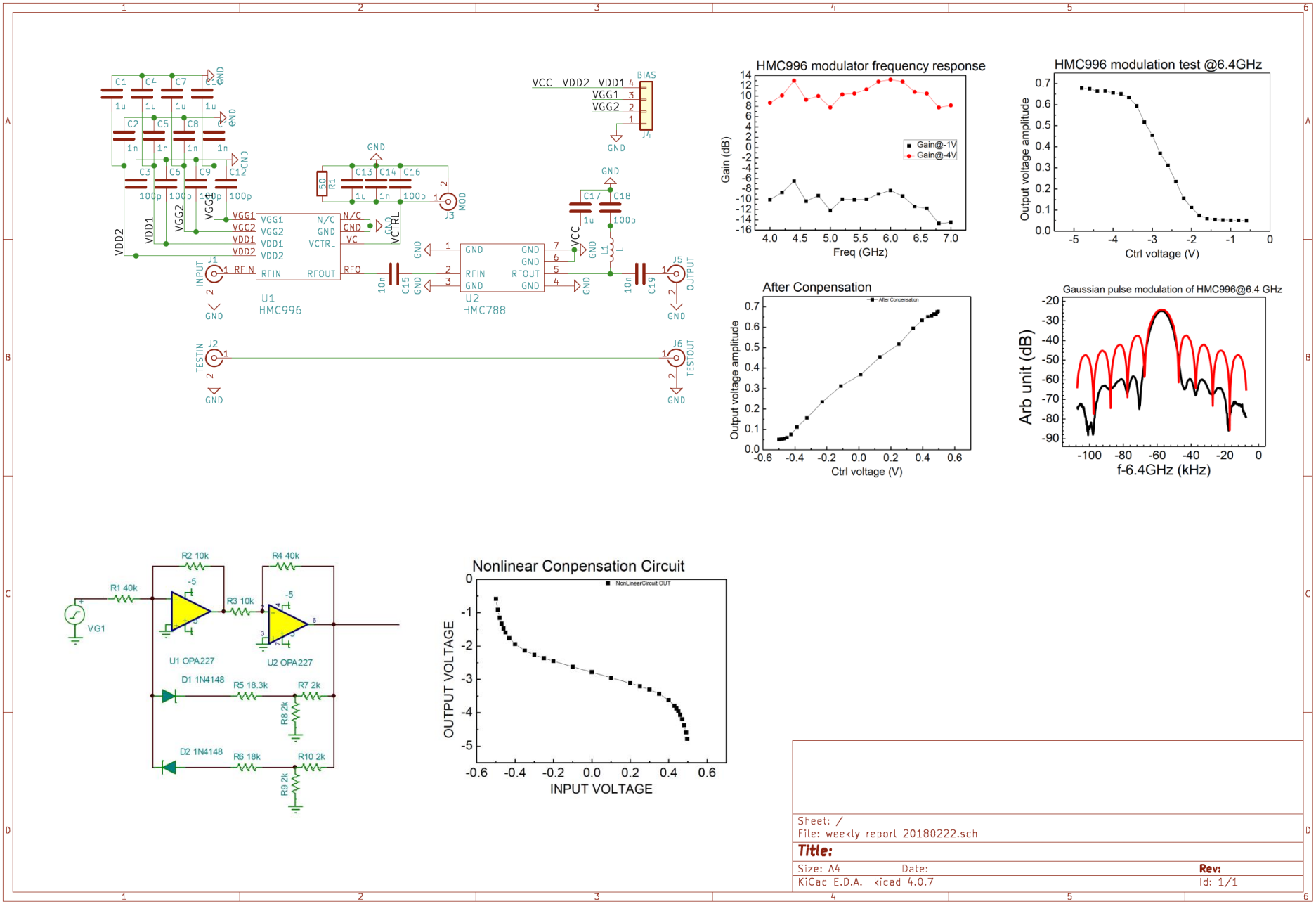

Fig. A.7. Microwave pulse amplitude modulator with nonlinear compensation for gain control. The insets show the testing result.

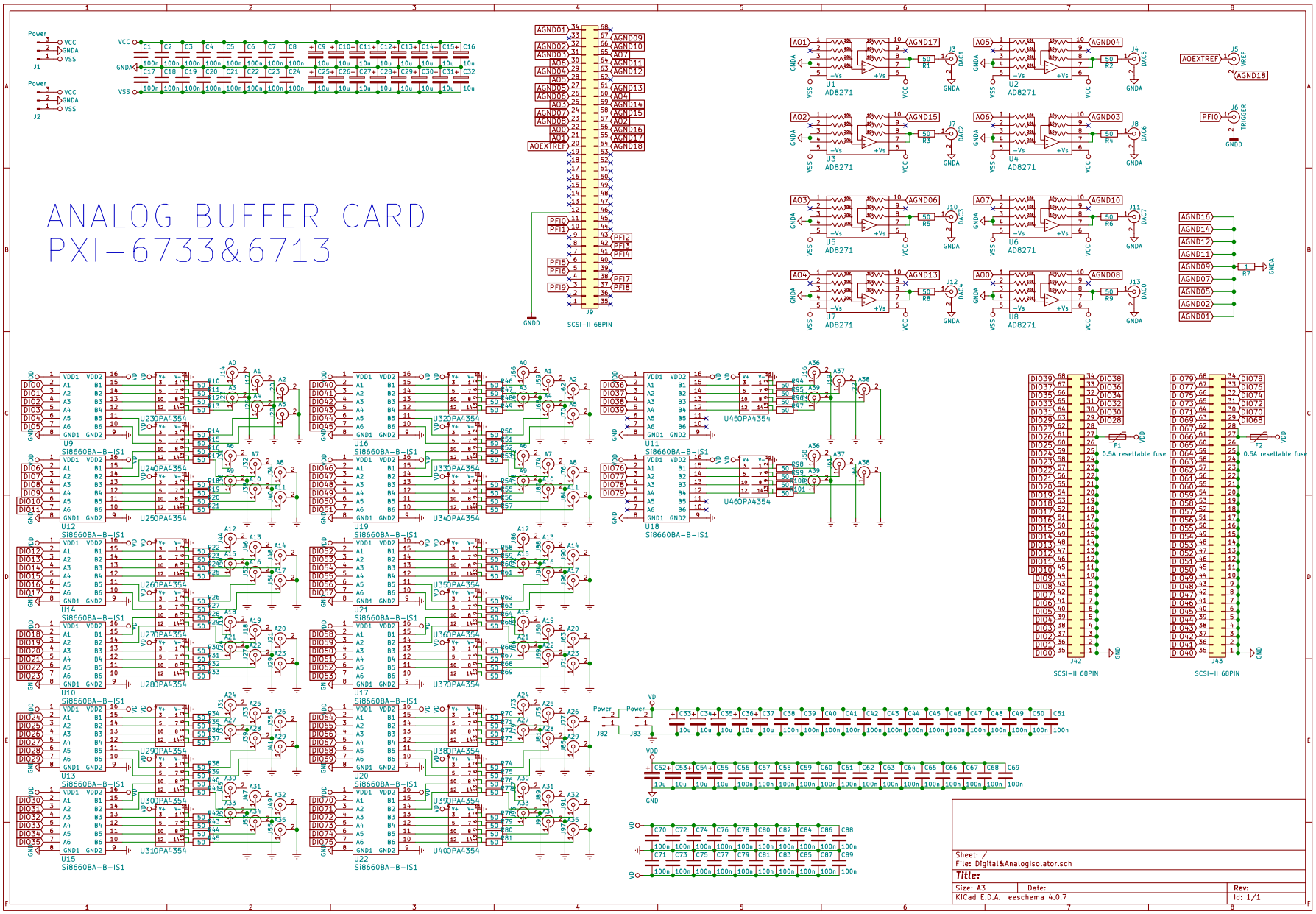

Fig. A.8. The analog and digital interface and isolation board for NI 6733/6713 and NI 7811R cards.

A.4 Programs

A.4.1 Voltage reference driver for Arduino

This code converts the I^2C bus commands (voltage and ramping time) into the voltage output control signal (SPI bus) for the AD5791 DAC voltage reference board. The ramping voltage is immediately generated after each command. The ramping time can be set between 0 to 255 ms and the voltage codes ranges from 0 to 1048575 ($2^{20} - 1$).

The code also provides the connection to LCD1602, which will show the receiving command after each output event. This will help you to find out whether the communication is correct.

```
#include <SPI.h>
#include <Wire.h>
#include <LiquidCrystal.h>

LiquidCrystal lcd(6, 7, 5, 4, 3, 2);
const int SyncPin = 10;
const int IntPin = 8;
const int DAC     = 0x10;
const int CTRL    = 0x20;
const int DACSET  = 0x0012;
const uint32_t fullDigit = 1048575;
uint32_t lastDACvalue;
uint8_t rampTime = 5;
uint16_t i = 0;
boolean Rcv = 0;

union myUnion{
  uint32_t DACvoltage;
  uint8_t DACvalue[4];
};

void setup() {
```

```
  Wire.begin(8);                 // join i2c bus with
      address #8
  Wire.setClock(10000L);        // IIC CLK
  Wire.onReceive(receiveEvent); // register event
  Serial.begin(9600);
  pinMode(SyncPin, OUTPUT);
  SPI.begin();
  SPI.beginTransaction(SPISettings(30000000,
     MSBFIRST, SPI_MODE1));
  lcd.begin(16, 2);
  digitalPotWrite(CTRL, DACSET);
  delay(100);
  uint8_t ii;
  for(ii=1; ii<40; ii++) {
    lcd.setCursor(15, 0);
    lcd.print("Magnetic Field Controller");
    lcd.setCursor(15, 1);
    lcd.print("      CUHK BEC LAB");
    lcd.scrollDisplayLeft();
    delay(200);
  }
  lcd.clear();
}

void loop() {
//  digitalPotWrite(CTRL, DACSET);
//  delay(100);
//  digitalPotWrite(DAC, fullDigit/2);
//  delay(100);
  if(Rcv == 1){
    if(i<2){
      lcd.setCursor(13, 0);
      lcd.print("Rcv");
      lcdPrint();
      i++;
    }
```

```
57      else if(i>=100){
58        lcd.setCursor(13, 0);
59        lcd.print("   ");
60        lcdPrint();
61        i = 0;
62        Rcv = 0;
63      }
64      else{
65        i++;
66      }
67     }
68     delay(1);
69 }
70
71 void receiveEvent(int howMany) {
72   Rcv = 1;
73   while (4 < Wire.available()) { // loop through all
         but the last
74     char c = Wire.read();         // receive byte as
          a character
75     //Serial.print(c);            // print the
          character
76   }
77   myUnion val;
78   val.DACvalue[2] = Wire.read(); // receive byte as
       an integer
79   val.DACvalue[1] = Wire.read();
80   val.DACvalue[0] = Wire.read();
81   rampTime = Wire.read();
82   rampWrite(rampTime, lastDACvalue, val.DACvoltage);
83   lastDACvalue = val.DACvoltage&0xFFFFFF;
84
85   //float voltage = (float) 7.1345* val.DACvoltage
       /1048575;
86   //Serial.println(voltage, 6);
87   Serial.println(lastDACvalue);// print the integer
```

```
}

void digitalPotWrite(uint8_t reg, uint32_t value) {
  myUnion val;
  val.DACvoltage = value;
  val.DACvalue[2]&= 0x0F;
  val.DACvalue[2]|= reg;
  digitalWrite(SyncPin, LOW);
  SPI.transfer(val.DACvalue[2]);
  SPI.transfer(val.DACvalue[1]);
  SPI.transfer(val.DACvalue[0]);
  digitalWrite(SyncPin, HIGH);
}

void rampWrite(uint8_t risingTime, uint32_t iValue,
   uint32_t fValue){
  digitalWrite(IntPin, LOW);
  uint16_t datapoints = risingTime*48;
  uint32_t Value = iValue;
  digitalPotWrite(CTRL, DACSET);
  if(iValue>fValue){
    int stepValue = (iValue-fValue)/datapoints;
    for(int i=0; i<=datapoints; i++){
      digitalPotWrite(DAC, Value);
      Value = Value - stepValue;
    }
    digitalPotWrite(DAC, fValue);
  }
  else{
    int stepValue = (fValue-iValue)/datapoints;
    for(int i=0; i<=datapoints; i++){
      digitalPotWrite(DAC, Value);
      Value = Value + stepValue;
    }
    digitalPotWrite(DAC, fValue);
  }
```

```
123   digitalWrite(IntPin, LOW);
124 }
125
126 void lcdPrint(void){
127   lcd.setCursor(0, 0);
128   lcd.print("Ramp:   ms");
129   lcd.setCursor(5, 0);
130   lcd.print(rampTime);
131   lcd.setCursor(0, 1);
132   lcd.print("RefOut:        V");
133   float voltage = (float) 7.1346* lastDACvalue
        /1048575;
134   lcd.setCursor(7, 1);
135   lcd.print(voltage, 6);
136   //Serial.println(lastDACvalue);
137 }
138
139 uint32_t serialDataRcv(void){
140   if (Serial.available() >0) {
141     uint32_t value = 0;
142     byte inByte;
143     char buffer[7];
144     int pointer;
145     inByte = Serial.read();
146     if (inByte == '#') {
147       while (pointer < 7) {
148         buffer[pointer] = Serial.read();
149         pointer++;
150         }
151         pointer = 0;
152         for(int i=0; i<=6; i++){
153         value = hex2dec(buffer[i]) + value*10;
154         }
155         return value;
156     }
157     }
```

```
158 }
159
160 int hex2dec(byte c) { // converts one HEX character
      into a number
161   if (c >= '0' && c <= '9') {
162   return c - '0';
163   }
164   else if (c >= 'A' && c <= 'F') {
165   return c - 'A' + 10;
166   }
167 }
```

A.4.2 I²C bus master for TTL control signal

The above DAC reference driver needs the I²C interface to control the output signal. This codes can be used to replace the I²C interface if there is only TTL control signal.

The 8 byte register "outputValue" stores a maximum eight DAC values that we need to use in the experiment. And the "rampTime" stores the eight ramping time for reaching each value. $Ch2:Ch1:Ch0$ sets the value we need. For example, if we want to output the 4th value in "outputValue", we set $Ch2:Ch1:Ch0=011$ and use the rising edge of the TTL connected to the "intteruptPin" to trigger the output.

The value in the register can be modified by reprogramming the Arduino or the serial port. For the serial port modifications, the microcontroller will lose all the modifications after reset. For example, if you want to change the 5th value in "outputValue", you need to input "Exxxxxxx", where "E" stands for 5th DAC value and "xxxxxxx" is the value we need. And if you want to change the ramp time for 2nd value, you need to imput "bxxx", where "b" stands for the ramping time for 2nd DAC value and "xxx" is the time we need. You also need to add additional zeros in front of the value if the value is not in 7 or 3 digits.

```
1 #include <Wire.h>
```

```
2
3 uint32_t outputValue[8] = {0, 151914, 873418,
    915208, 880090, 678802, 841712, 63062};//0, 60,
    347.64, 364.3, 350.3, 270.2, 335, (477322,190)
    (699057,276.1)(24.6,63062)(668250,266) (974880
    ,388)
4 uint8_t rampTime[8] =  {0, 0, 1, 0, 1, 1, 1, 1};
5 const byte interruptPin = 7;
6 const byte Ch2 = 4;
7 const byte Ch1 = 5;
8 const byte Ch0 = 6;
9
10 union myUnion{
11   uint32_t DACvoltage;
12   uint8_t DACvalue[4];
13 };
14
15 void setup() {
16   Serial.begin(9600);
17   Wire.begin(); // join i2c bus (address optional
       for master)
18   Wire.setClock(100000L);       // 400kHz IIC CLK
19   pinMode(Ch0, INPUT);
20   pinMode(Ch1, INPUT);
21   pinMode(Ch2, INPUT);
22   pinMode(interruptPin, INPUT);
23   attachInterrupt(digitalPinToInterrupt(interruptPin
       ), sendcomm, RISING);
24 }
25
26 void loop() {
27   serialDataUpload();
28   delay(1);
29 }
30
31 void sendcomm(void){
```

```
32    uint8_t a =  digitalRead(Ch0);
33    uint8_t b =  digitalRead(Ch1);
34    uint8_t c =  digitalRead(Ch2);
35    b = b << 1;
36    c = c << 2;
37    int number = a + b + c;
38    noInterrupts();
39    interrupts();
40    I2CdataSend(outputValue[number], rampTime[number])
        ;
41    Serial.println(number);
42 }
43
44 void I2CdataSend(uint32_t voltage, uint8_t rampTime)
     {
45    myUnion val;
46    val.DACvoltage = voltage;
47    Wire.beginTransmission(8); // transmit to device
        #8
48    Wire.write(val.DACvalue[2]);
49    Wire.write(val.DACvalue[1]);
50    Wire.write(val.DACvalue[0]);
51    Wire.write(rampTime);
52    Wire.endTransmission();    // stop transmitting
53 }
54
55 void serialDataUpload(void){
56     uint32_t valueRcv;
57     if (Serial.available() >0) {
58       byte inByte;
59       byte number;
60       int pointer = 0;
61       char buffer[7];
62       inByte = Serial.read();
63       if(inByte <= 'H' && inByte >= 'A'){
64          number = (hex2dec(inByte)-10);
```

```
65          valueRcv = 0;
66          while (pointer < 7) {
67           buffer[pointer] = Serial.read();
68           pointer++;
69           }
70           pointer = 0;
71           for(int i=0; i<=6; i++){
72           valueRcv = hex2dec(buffer[i]) + valueRcv
                *10;
73           }
74          outputValue[number] = 1048575.0* (float)
               valueRcv / 7134600.0 ;
75          Serial.println(outputValue[number]);
76        }
77        else if(inByte <= 'h' && inByte >= 'a'){
78          number = (hex2dec(inByte)-10);
79          valueRcv = 0;
80          while (pointer < 3) {
81           buffer[pointer] = Serial.read();
82           pointer++;
83           }
84           pointer = 0;
85           for(int i=0; i<=2; i++){
86           valueRcv = hex2dec(buffer[i]) + valueRcv
                *10;
87           }
88          rampTime[number] = valueRcv;
89          Serial.println(rampTime[number]);
90        }
91     }
92 }
93
94 int hex2dec(byte c) { // converts one HEX character
      into a number
95   if (c >= '0' && c <= '9') {
96   return c - '0';
```

```
97    }
98    else if (c >= 'A' && c <= 'Z') {
99    return c - 'A' + 10;
100   }
101   else if (c >= 'a' && c <= 'z') {
102   return c - 'a' + 10;
103   }
104 }
```